Mathematical Modeling of Proton Exchange Membrane Fuel Cells

by

Andrew Michael Rowe
B. Eng., Royal Military College of Canada, 1992

A Thesis Submitted in Partial Fulfillment of the
Requirements for the Degree of
MASTER OF APPLIED SCIENCE
in the
Department of Mechanical Engineering.

We accept this thesis as conforming
to the required standard

Dr. X. Li, Supervisor (Dept. of Mechanical Engineering)

Dr. Z. Dong, Departmental Member (Dept. of Mechanical Engineering)

Dr. J. Haddow, Departmental Member (Dept. of Mechanical Engineering)

Dr. D. Harrington, External Examiner (Dept. of Chemistry)

University of Victoria

Supervisor: Dr. Xianguo Li

Abstract

A good understanding of the various mass and heat transport, and electrochemical reaction processes is required for design strategies that lead to increased performance of proton exchange membrane (PEM) fuel cells. Traditionally, attempts at understanding how these processes interact has been through mathematical modeling where efforts have focussed on understanding the cathode. The interaction between mass transport, membrane hydration and the effects of heat generation and transfer complicates our understanding of relevant processes, hampering the effort to improve fuel cell performance.

To further our basic understanding of how the power density of a PEM fuel cell can be increased, and, thereby, decrease the cost of a complete fuel cell system, a comprehensive performance model of a PEM fuel cell has been formulated and investigated. This model explicitly examines the anode as well as the cathode, and includes the effects of energy transfer as temperature control is critical to PEM cells. The results of this model suggest that humidification of the cathode gas stream may be reduced at high operating currents, the temperature peak across a single cell increases as operating temperature decreases, and the gas backing has a significant effect on mass transport at typical operating potentials, especially with air operation.

Examiners:

Dr. X. Li, Supervisor (Dept. of Mechanical Engineering)

Dr. Z. Dong, Departmental Member (Dept. of Mechanical Engineering)

Dr. J. Haddow, Departmental Member (Dept. of Mechanical Engineering)

Dr. D. Harrington, External Examiner (Dept. of Chemistry)

Table of Contents

List of Tables

List of Figures

Nomenclature

A	reactive surface area per unit mass catalyst [cm^2/g]
a	active area per unit volume [cm^2/cm^3]
c	concentration [$mole/cm^3$]
c_{pi}	mass heat capacity at constant pressure [J/g]
D_3	diffusivity of water in membrane [cm^2/s]
D_{ij}	diffusivity for species i in species j [cm^2/s]
E_{cell}	cell potential difference [V]
F	Faraday's Constant 96487 [Coulombs/mole]
Δg	Gibb's free energy change [J/g]
$\Delta\bar{g}$	molar Gibb's free energy change [J/mole]
H	Henry's contstant [$atm\text{-}cm^3/mole$]
Δh	enthalpy change [J/g]
$\Delta\bar{h}$	molar enthalpy change [J/mole]
h^0_{fi}	enthalpy of formation at STP [J/g]
h_m	mass transfer coefficient $[s]^{-1}$
h_{vap}	mass enthalpy of vaporization [J/g]
$\bar{h}_{vap}$	molar enthalpy of vaporization [J/mole]
I	operating current density [A/cm^2]
i_0	exchange current density [A/cm^2]
i_m	catalyst layer membrane phase current density [A/cm^2]
i_s	catalyst layer solid phase current density [A/cm^2]
$j(x)$	reaction rate [A/cm^3]
K_p	equilibrium constant
k	thermal conductivity [W/cm-K]
k_p	hydraulic permeability [cm^2]
L	characteristic length scale [cm]
M_i	species i
m	catalyst loading [g/cm^2]

N_i	molar flux of species i [mole/cm^2-s]
n	moles of electrons transferred per mole reactant
p	pressure [atm]
q	heat flux [W/cm^2]
$\dot{q}_s$	heat source [W/cm^3]
R	universal gas constant 8.314 [J/mole-K]
S	all species
$\bar{S}$	Sutherland constant [K]
S_{nc}	non-charged species only
Δs	entropy change [J/g-K]
$\Delta \bar{s}$	molar entropy change [J/mole-K]
sh	Sherwood Number
T	temperature [K]
t_e	electrode thickness [cm]
t_m	membrane thickness [cm]
t_l	catalyst layer thickness [cm]
u	internal energy [J/g]
V_{oc}	reversible cell potential [V]
V_i	diffusion velocity of species i [cm/s]
v	mass-average velocity [cm/s]
v_i	absolute velocity of species i [cm/s]
W_i	molar mass of species i [g/mole]
W_m	membrane equivalent weight [g/mole]
w_i	mass source for species i [g/cm^3]
$\dot{w}$	work rate [W/cm^3]
x	position co-ordinate
x_i	mole fraction of species i
Y_i	mass fraction of species i

Greek Symbols

α_a	apparent transfer coefficient for anodic reaction
α_c	apparent transfer coefficient for cathodic reaction
β	symmetry factor
η	gas viscosity [μP]
η_{tot}	total cell polarization [V]
η_{a}	activation polarization [V]
η_{c}	concentration polarization [V]
η_{ohmic}	ohmic polarization [V]
η_d	electro-osmotic drag coefficient
Φ	potential [V]
ν_i	stoichiometric coefficient for species i
ρ	density [g/cm^3]
τ_{ij}	deviatoric stress tensor [N/cm^2]
ζ	stoichiometric flow rate
σ	electronic conductivity [Ω-cm]$^{-1}$
κ	ionic conductivity [Ω-cm]$^{-1}$
γ	order of reaction with respect to species i
ϵ_w	volume fraction of water
ϵ_e	volume fraction of void space in electrode
τ	tortuosity
μ	viscosity [g/cm-s]
δ	membrane expansion coefficient
λ	membrane hydration [moles water/moles charge sites]

Superscripts

*	non-dimensionalized parameter
^{g}	gas
$^\ell$	liquid
$^{\text{mem}}$	membrane
$^{\text{eff}}$	effective value of parameter
^{z_i}	charge of species i
$^{\text{ref}}$	reference value

Acknowledgements

I would like to thank my supervisor, Dr. Xianguo Li, who exemplifies leadership by example, and Mr. Jon Pharoah for freely distributing his computing knowledge.

This work has been made possible by a Collaborative Research and Development (CRD) grant between British Gas PLC, Ballard Power Systems and the Natural Sciences and Engineering Research Council of Canada.

Chapter 1

Introduction

> *The economic and technological triumphs of the past few years have not solved as many problems as we thought they would, and, in fact, have brought us new problems we did not forsee.*
>
> *–Henry Ford II*

1.1 Background

In 1839, Sir William Grove performed experiments that converted the chemical energy of oxygen and hydrogen directly into electricity, thus, beginning modern fuel cell research. A fuel cell is an electro-chemical device that converts the chemical energy of a fuel directly to electricity. Unlike a battery, the reactants powering a fuel cell are not an intrinsic part of the device. Moreover, a battery is primarily a means of storing energy while a fuel cell is a means to energy conversion. In its primary role, a fuel cell is comparable to an internal combustion engine, in that energy is converted to work; however, a fuel cell has some inherent advantages over traditional heat engines.

It is well known that the thermal efficiency of a heat engine is subject to the limitation described by Carnot - a limitation imposed by the second law of thermodynamics. So, too, is the maximum theoretical efficiency of a fuel cell limited by the second law; however, unlike a heat engine, the ideal efficiency is not determined by the temperature of two heat reservoirs. This leads to theoretical efficiencies for hydrogen-oxygen fuel cells at standard conditions that are as high as 83 percent. Other advantages of fuel cells are mechanical simplicity, modularity, low noise, and perhaps most importantly, reduced levels of pollution directly attributable to the energy conversion process (compared to internal combustion engines). This is a difficult statement philosophically and semantically, since how pollutant is defined seems to be changing. The legacy of hydrocarbon fuels is only now being realized. The effects of two centuries of converting stored carbon into what was once considered harmless carbon dioxide is forcing human-kind to explore more efficient ways of converting energy and, in doing so, reducing oxide emissions of nitrogen, sulphur, and carbon.

It is envisioned that one of the most promising energy carriers for a sustainable future is hydrogen [1]. The use of the most prolific element in the universe as a fuel, with oxygen as the oxidant, produces one of the most benign compounds found on earth - water. If science has aesthetics, then such a future is truly a vision. The growth of fuel cell technology is inexorably linked to this future since hydrogen is ultimately the reductant of choice. At the present time, if neat hydrogen is not used as the fuel in a cell then it is derived from some other hydrocarbon. In the case of the oxidant, for terrestrial applications, air typically provides oxygen. Unfortunately, at this time, it is not clear whether fuel cell technology will beget the hydrogen age, or if the availability of hydrogen will beget fuel cell proliferation. For the past 150 years the evolution of using hydrogen as a primary energy carrier has seemed to move along hand-in-hand with the growth of fuel cells as energy converters; both slowly advancing, but neither becoming a commercial reality.

1.2 Proton Exchange Membrane Fuel Cells

Energy conversion is ubiquitous. The most interesting applications of energy conversion from the perspective of man-kind, other than life itself, are the services that we derive from it. As our demand for services grows, so too does the need for power conversion. The automobile has become one of the most desired services in western society and consumes large quantities of fossil fuel. As a result, transportation was responsible for nearly 30% of urban CO_2 emssions in OECD countries in 1993;

moreover, harmful emssions are typically associated with fossil fuel consumption [2]. Replacing the IC engine with a more efficient and environmentally benign technology is one way of lessening these negative aspects of automobile use. In 1996, approximately 85% of U.S. energy demand was provided by fossil fuels; 26% of that was for transportation [3]. With these factors in mind, the use of fuel cells in transportation applications appears to be highly desireable.

Amongst the many types of fuel cells being developed, the Proton Exchange Membrane (PEM) fuel cell is currently the most likely to be the first powering a commercially viable vehicle [4]. The characteristic that differs PEM cells from other types of fuel cells is the use of an ionomeric membrane as the electrolyte. The membrane is sandwiched between two electrodes, usually incorporating a thin catalyst layer, and the resulting Membrane Electrode Assembly (MEA) is then mounted between plates incorporating channels for the delivery of gaseous reactants and also serving as current collectors. Such an assembly can be considered to be a unit cell. Joining these unit cells together in parallel or series results in a fuel cell stack. The power derived from a single cell largely determines the overall stack volume, mass, and cost. Normalizing the power by any of these parameters gives a characteristic power density of the cell (or stack). Obviously, increasing the power density of a cell is beneficial.

The power output of cell is determined by the overall cell potential at a given current density. In an ideal case, the potential between the two electrodes of a cell would remain constant at the reversible potential for all current densities. In reality, various losses in the cell cause the potential to decrease as the current demand increases. These losses are known as polarizations. In the past, three primary types of polarization have been identified: activation, ohmic, and concentration. Activation polarization is a result of energy being required to drive the electrode reaction at rates that exceed those at equilibrium. Ohmic losses are proportional to the current density and result from low membrane ionic conductivities and electronic resistance in the current carrying components of the stack. In a practical fuel cell, the delivery of fuel and oxidant to the reaction site, and product removal, occurs at a finite rate; concentration polarization results from these characteristic mass-transport limitations. The polarization associated with the operation of PEM fuel cells is one of the technological barriers limiting contemporary PEM cell commercialization.

A thorough understanding of how cell potential is affected by operating parameters such as temperature, pressure, stoichiometry, and gas stream composition is required in order to optimize cell and stack design. Cell structure and material is also of importance. Some design issues currently being researched are humidification and heat removal, catalyst layer composition, and ionomer optimization. Problems particular to PEM fuel cells result from the use of an ionomer as an electrolyte. With contemporary membranes the solubility of a reactant gas in the electrolyte is a function of membrane moisture content and temperature. These membranes also require humidification to minimize ionic resistivity; humidification is often performed via water vapour in the gas stream. While water is required to hydrate the membrane, water production can also be a problem due to the possibility of flooding of the electrode pores, thereby limiting gas transport to the reaction sites. It is well known that increasing the operating temperature of a PEM cell can decrease mass-transport limitations, increase conductivities, and increase the electrochemical reaction rates. However, increased temperature also has an adverse effect on the maximum cell potential due to thermodynamic considerations and the increase in water vapour partial pressure.

Cell morphology is of importance for many reasons, one of the most significant derives from the cathode reaction being extremely slow. At typical operating temperatures, an expensive platinum catalyst is required to decrease the activation polarization; furthermore, poor reaction kinetics are exacerbated by low gas solubilities in the membrane material. Novel catalyst layer structures to both increase the active surface area available for reaction and to provide a means for gas diffusion to the reaction sites are being studied. Clearly, optimizing cell design and physical operating conditions is not a simple task.

1.3 Fuel Cell Modelling

Mathematical modelling is a common tool for complex problems. A numerical model facilitates research and design by reducing the need for repetitive and costly experimentation. Often the more predictive a model is, the more insightful and valuable the results are. Incorportating as many of the relevant physical processes occuring in a numerical model is beneficial for ensuring the acccuracy of model predictions. Some of the more important factors affecting PEM cell performance have been mentioned; however, our understanding of some cell mechanisms is still lacking.

The power density of a fuel cell is the characteristic measure of performance. At the current stage of PEM cell development, the performance should be further increased for reasons of cost and compatability with transportation applications. To increase power density, PEM cell design needs to be optimized in areas such as electrode kinetics, water and thermal management, and membrane characteristics, to name a few. Optimizing is well adapted to numerical modelling. Two common modelling approaches are (1) theoretically based mechanistic models and, (2) emperically based analyses. Mechanistic models tend to be generalizable; however in the case of PEM cells detailed information regarding some of the processes in the cell is unavailable and simplifying approximations are required. In contrast, empirical models re-create observed data well, but lack predictability. Where knowledge is lacking a combination of these two approaches can be used. By creating a model that reproduces experimentally derived data, overall polarization can be studied and parameters altered to help predict the influences of operating conditions and cell design on performance.

If one sets current density as the independent variable, then cell voltage is the variable of interest for determining power density of a fuel cell. The overall cell potential can be defined by:

$$E_{\text{cell}} = V_{oc} - \eta_{\text{tot}} \tag{1.1}$$

where,

$$\eta_{\text{tot}} = \eta_a + \eta_c + \eta_{\text{ohmic}} \tag{1.2}$$

In Eqn (1.1), E_{cell} is the potential difference between the anode and cathode, V_{oc} is the reversible cell potential, and η_{tot} is the total cell polarization. In Eqn (1.2), η_a is the activation polarization, η_c is the concentration polarization, and η_{ohmic} represents the resistive losses in the cell. As can be seen, modelling the various mechanisms occuring in a fuel cell that lead to polarizations allows the cell voltage, hence power density, to be determined.

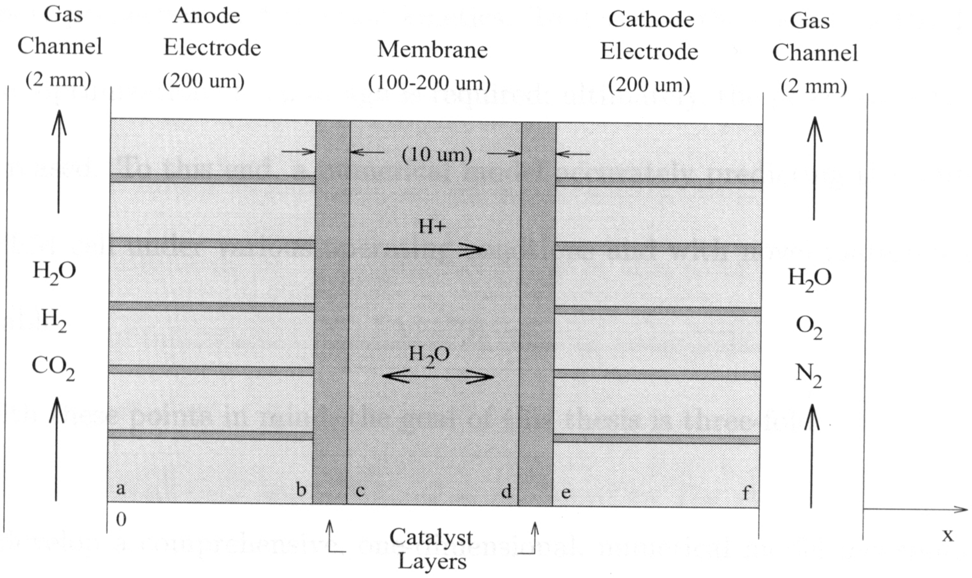

Figure 1.1: One-dimensional representation of a PEM fuel cell.

Figure 1.1 is a one-dimensional representation of a PEM fuel cell. If one ignores the effects of the gas distribution plates, then five distinct regions can be identified. A complete mathematical model for a cell can be created by amalgamating sub-models describing each layer.

1.4 Thesis Goal

The Membrane Electrode Assembly is the heart of the PEM fuel cell energy conversion process. The design of a fuel cell stack, thermal and water managment sub-system, and the means of delivering fuel and oxidant are dependent upon the operating conditions of the cells. The optimum design point for a cell is determined by cell materials, transport properties, and reaction kinetics. To decrease the costs of a PEM fuel cell system, optimization of cell design is required; ultimately, the power density needs to be increased. To this end, a numerical model accurately predicting the performance of a PEM cell under various operating condtions and with novel materials is highly desireable.

With these points in mind, the goal of this thesis is three-fold:

- develop a comprehensive, one-dimensional, numerical model incorporating energy conservation that predicts overall cell potential in PEM fuel cells;
- examine the effects operating conditions and physical parameters have on cell polarization;
- examine the effects of heat production on cell temperature profile and cell performance.

1.5 Literature Review

The past decade has seen a large amount of modelling work devoted to the study of PEM fuel cells. Often, the models are coupled with experimental work being performed by the authors. This can lead to models that are cell specific and sometimes highly empirical. Other researchers pursue a more analytical description of a PEM cell in hopes of creating a generalizeable and predictive model.

One of the earlier models addressing water management in PEM fuel cells was developed by Bernardi [5]. The primary focus of this work was the humidification requirements of inlet gases to mainatain a state of water balance in a PEM cell. This work assumes that the cell is isothermal, the gas diffusion electrodes are free of water droplets, and that only water vapour is produced by the electrochemical reaction. Further assumptions are that the electro-osmotic drag of water and pressure induced flow across the membrane are insignificant next to the flow caused by a concentration gradients. This is assumed to be valid for a thin membrane. The model is one-dimensional. Results of Bernardi's model suggest that the current density needed to maintain a water balance increases with increasing temperature due to larger water evaporation. Her work also suggests that oxygen transport in the cathode may limit fuel cell performance due to the current required to maintain water balance being higher than the diffusion-limiting current density. Another conclusion of significance is that humidifying the fuel stream may be preferable to the cathode stream, since it is not transport-limited.

Bernardi continued her modelling work with Verbrugge by investigating the performance of a gas-fed porous cathode bonded to an ion-exchange membrane [6]. In this model, the cell is assumed to be isothermal and the gas streams ideal. The membrane is once again assumed to be completely hydrated; however, unlike her previous model, the flux of water through the membrane due to pressure and potential gradients is addressed. The possibility of liquid water as well as vapour flux in the electrode is considered. The mathematical model is derived from analytic expressions describing the physical processes occuring in three layers: cathode electrode, catalyst layer, and membrane. The effects of the hydrogen electrode are neglected. The results of this model predict a performance for a complete PEM cell that agrees well with some experimental work. Results indicate that at higher operating currents, the resistance of the membrane is a significant contributor to overall polarization. The model also predicts that at typical operating currents, the cathode reaction is essentially a surface reaction at the front of the catalyst-layer; a result of low reactant permeability.

Bernardi and Verbrugge completed their model evolution with a one-dimensional, isothermal model of a complete PEM Membrane Electrode Assembly [7]. This model demonstrates a good agreement with experimental cell polarization curves and investigates the use of membranes with varying thickness. The results of using a Dow membrane as compared to Nafion are explored. Experimentally determined parameters are used wherever possible; however, the cathode exchange current density per unit volume is adjusted to fit performance data. The hydraulic permeability is also adjusted to fit experimental water-transport characteristics. Besides predicting the relative contributions of different processes to overall polarization, the model shows that membrane dehydration can pose limitations on operating current density. They suggest that electrodes with low hydraulic permeability are advantageous for maintaining membrane hydration.

In contrast to the model of Bernardi and Verbrugge that focussed on a cathode electrode bonded to an ionomeric membrane, the work of Wang and Savinell models the hydrogen electrode bonded to a membrane [8]. One novel aspect of this model is that it examines the effect of CO poisoning of the platinum catalyst. This model assumes that the catalyst layer is made up of two phases only, polymer and platinum covered carbon particles uniformly distributed throughout the layer. Humidified hydrogen is taken to make up the anode gas stream. Their results show that catalyst layer thickness has a significant impact on the electrode performance and that increasing the effective diffusion coefficient of hydrogen in the layer will enhance performance. Their results predict an optimum polymer volume fraction and catalyst layer thickness of 0.5 and 1.5-4.0 μm respectively. They also state that for the anode the optimal platinum coverage need not exceed 20 wt% Pt/C.

A significant amount of experimental and theoretical PEM fuel cell work is being performed at Los Alamos National Laboratories. The modelling being performed there is of special interest because, in most cases, it is being rigorously coupled with experimental work. One of the groups led by Springer has contributed significantly to the understanding of the processes occuring in complete fuel cell assemblies. An early model from this group is an isothermal, one-dimensional, steady-state model of a complete polymer electrolyte fuel cell [9]. The interesting aspect of this model is the ability to examine variable membrane hydration. The anode catalyst layer is neglected and the cathode catalyst layer is assumed to be a thin reactive plane. The presence of liquid water in the electrodes is ignored; instead, it is assumed that the water vapour activity can exceed unity and that the activity at the electrode-catalyst layer interface determines the hydration in the membrane at that point. Their model predicts a net water per proton flux of 0.2 for typical operating conditions which compares well to their experimental measurements. They also show that significant advantages concerning cell performance result from using thinner membranes.

A more ambitious model examining water and thermal managment in PEM fuel cells was developed by Fuller and Newman [10]. This model is a quasi-two-dimensional look at water and thermal management. The model assumes the oxidation of hydrogen and the evaporation of water are fast and can be neglected. To produce a performance curve that suitably mimics experimental results, the surface area of reactive sites per unit volume and the kinetic rate constants are adjusted. Their model examines the effect of various heat-transfer coefficients on energy transfer from the cell. The model is essentially one-dimensional; however, by breaking the cell into sections and integrating down the flow channels a two-dimensional approximation is produced. They conclude that thermal considerations must be included in an analysis of water management.

The importance of water and thermal management in PEM cells is reflected in the numerous models devoted its study. A model developed by Nguyen and White was used to explore the effects of various forms of gas humidification on cell performance and water management [11]. This model is two-dimensional, however, the MEA assembly is greatly simplified. The electrode is assumed to be ultra-thin and gas diffusion therein is neglected. Water is assumed to leave the gas channels as vapour only and water transport across the membrane is assumed to be the result of migration and diffusion. The results of their model examine the variation in gas stream composition and temperature down the gas channels. They conclude that the anode gas stream must be humidifed for high power densities, and, when air is used, the cathode stream must be humidifed as well.

Further work by Springer et al. fits a number of performance curves using experimentally determined parameters [12]. This model considers interfacial kinetics at the Pt/ionomer interface, gas-transport and ionic-conductivity limitations in the catalyst layer, and gas-transport limitations in the cathode backing. Combined with experimental results, this model suggests that gas transport limitations in the cathode backing determine the cell limiting current and affect the slope of the polarization curve in the medium current density region. As a result of fitting their model to numerous experimental data, they conclude that the permeability of reactant gas in their thin-film catalyst structures is approximately three orders of magnitude higher than in neat ionomer.

Experimental work is again coupled with modeling of PEM cells in the work of Rho et al. [13]. An experimental analysis of the oxygen reduction reaction using gas mixtures composed of oxygen with helium, argon, and nitrogen is used to interpret the gas transport mechanism. They found that above an oxygen mole fraction of 0.4 in dry gas, mass transport effects are considerably reduced. To explain the rapid fall-off in cell potential at high current densities, they assume very low diffusion coefficients of oxygen in the substrate layer. Like most other models, this one is isothermal, one-dimensional and steady-state. The reactant gases are assumed to be saturated with water vapour.

Amphlett et al. developed a parametric model of a single PEM cell [4, 14]. A theoretical description of a cell is derived using a mechanistic methodology. From this model, a number of grouped parameters are identified. A Ballard Mark IV single cell is then used to gather empirical data to which the theoretical parameters are fit. The mechanistic model is developed assuming isothermal, one-dimensional, steady-state conditions. The cathode side of the membrane is assumed to be fully hydrated while the anode hydration is set using a relative humidity of 50%. Oxygen diffusion through membrane in the catalyst layer is neglected. Using linear regression analysis, experimental data is applied to determine the parametric coefficients. The results of this model suggest cathode kinetics are highly dependent on oxidant feed composition and mass transport effects. The model accurately predicts the performance curve of the Ballard Mark IV cell.

In a spirit similar to Amphlett, Kim et al. use an empirical equation to describe the performance curve of a PEM fuel cell over the complete operating range [15]. The inclusion of an exponential term with an adjustable parametric coefficient is found to accurately model performance curves up to and including the mass transport limited region. The mechanistic insights of this equation are limited; however, the equation is of some use where a simple equation is needed to simulate cell performance. Such an application may be a complete fuel cell system.

One of the most recent PEM models is from a group at Los Alamos [16]. Weisbrod et al. developed an isothermal, steady-state, one-dimensional model of a complete cell incorportating the membrane water model of Springer et al. This model explores the possibility of the water flux in the electrode backing being a result of vapour flux only, or with liquid water present as well. If liquid water is present, they assume the gas stream is saturated. For the catalyst layer model, they assume that the catalyst particles are covered by a thin film of ionomer and that diffusion through this film can be neglected. The volume composition they use for the catalyst layer is dominated by void space. The results of the model indicate that moderate cell performance is predicted for catalyst loadings less than 0.1 mg/cm^2. The model also indicates a drop in performance when the cell temperature is raised to approximately 100 ^{0}C with a gas stream pressure of 2 atm.

None of the models discussed have explored the temperature profile across a cell or examined the effects of vaporization in electrodes with unsaturated gas streams.

Chapter 2

Reversible Cell Potential

2.1 Introduction

The potential of a fuel cell at open circuit with no internal losses is known as the reversible cell potential, which is the maximum theoretical electric potential for a given reaction. This potential can be determined by thermodynamic considerations and is related to the change in Gibbs' free energy. For a constant temperature and pressure reaction, the difference in chemical potential between reacting species and products is determined by the change in Gibb's free energy which acts as the driving force for the reaction. In the case of an electrochemical conversion of species, the driving potential is known as the electromotive force and is measured by the voltage. For the reaction of oxygen and hydrogen yielding liquid water, the net change in

Gibbs' free energy per mole of fuel, $\Delta\bar{g}$, can be equated to the cell potential, V_{oc}, as follows:

$$V_{oc} = \frac{-\Delta\bar{g}}{nF} \tag{2.1}$$

where n is the number of electrons transferred per mole of fuel consumed, and F is the Faraday constant. The above expression relates the change in Gibbs' free energy to the cell voltage under no load, ideal conditions. When the circuit is completed, the cell potential decreases due to irreversible losses resulting from slow reaction kinetics, ohmic effects, and concentration gradients. These losses are known as polarizations or overpotentials.

2.2 Thermodynamic Formulation

For an overall fuel cell reaction involving a total of N species written in the following form,

$$\sum_{i=1}^{N} \nu_i' M_i = \sum_{i=1}^{N} \nu_i'' M_i \tag{2.2}$$

where ν_i' and ν_i'' represent the number of moles of reactants and products respectively, the change in the Gibbs' free energy per unit mole can be written as,

$$\Delta\bar{g} = \Delta\bar{h} - T\Delta\bar{s} \tag{2.3}$$

where $\Delta\bar{h}$ is the enthalpy change per unit mole of fuel, and $\Delta\bar{s}$ is the entropy change per mole of fuel for the overall reaction. Assuming that $\Delta\bar{s}$, is a constant over the temperature range being considered, and that the gaseous reactants and products can be considered to be perfect gases, then the reversible cell potential as a function of temperature and partial pressures is expressed by the Nernst equation,

$$V_{oc}(T, p_i) = \frac{1}{nF}\left[-\Delta\bar{g}^o + \Delta\bar{s}^o(T - T_0) - RT\ln K_p\right] \tag{2.4}$$

where

$$K_p = \prod_{i=1}^{N}\left(\frac{p_i}{p_0}\right)^{\nu_i'' - \nu_i'}. \tag{2.5}$$

Here $\Delta\bar{g}^o$ and $\Delta\bar{s}^o$ are the change in Gibbs free energy and entropy, respectively, at T_0 and p_0. Usually, T_0 is taken as 298 K, and p_0 is one atmosphere. In reality, $\Delta\bar{s}$ is not an invariant; hence, to maintain the generality of Eqn (2.1), the entropy change is not considered to be constant for computational purposes. Instead, the reversible cell potential for the overall fuel cell reaction of interest in this thesis,

$$H_2 + \frac{1}{2}O_2 \rightleftharpoons H_2O(\ell) \tag{2.6}$$

is calculated from the following equation,

$$V_{oc}(T, p_i) = \frac{1}{nF}\left[-\Delta\bar{g}(T, p_0) - RT \ln K_p\right]. \tag{2.7}$$

Clearly, the effects of pressure and concentration are described by the second term in Eqn (2.7).

It can be seen from Eqn (2.3) that the change in free energy, $\Delta\bar{g}(T, p_0)$, as a function of temperature requires that the enthalpy and entropy changes be determined. Assuming perfect gas behaviour for the gaseous species and simple, incompressible for the liquid species, the enthalpy and entropy changes for the overall reaction are obtained by:

$$\Delta\bar{h}(T, p_0) = \sum_{i=1}^{N}(\nu_i'' - \nu_i')\left(\bar{h}_{fi}^o + \int_{T_0}^{T}\bar{c}_{pi}\,dT\right) \tag{2.8}$$

$$\Delta\bar{s}(T, p_0) = \sum_{i=1}^{N}(\nu_i'' - \nu_i')\left(\bar{s}_i^o + \int_{T_0}^{T}\frac{\bar{c}_{pi}}{T}\,dT\right) \tag{2.9}$$

where $\bar{h}_{fi}^o$ is the enthalpy of formation for species i, $\bar{s}_i^o$ is the absolute entropy of species i as given in Table 2.1, and $\bar{c}_{pi}$ is the specific heat at constant pressure and is approximated as follows:

$$\frac{\bar{c}_{pi}}{R} = \alpha_i + \beta_i T + \gamma_i T^2 + \delta_i T^3 \qquad (gas). \tag{2.10}$$

where R is the universal gas constant (8.314 J/mole-K), and the coefficients, α_i, β_i, γ_i, and δ_i are given in Table 2.2 [17]. The variation in heat capacity for liquid water over the temperature range of interest is small, therefore, it is taken to be a constant.

Species	$\bar{h}^o_{fi}$	$\bar{s}^o_i$
H_2	0	130.57 J/mole-K
O_2	0	205.03 J/mole-K
$H_2O_{(\ell)}$	-285830 J/mole	69.95 J/mole-K

Table 2.1: Thermodynamic Constants

Species	α	$\beta \times 10^3$	$\gamma \times 10^6$	$\delta \times 10^9$
H_2	3.057	2.677	-5.810	5.521
O_2	3.626	-1.878	7.055	-6.764
$H_2O_{(v)}$	4.070	-1.108	4.152	-2.964
$H_2O_{(\ell)}$	$\bar{c}_p = 75.4$ J/mole-K			

Table 2.2: Heat Capacity Parameters

The free energy change for the overall reaction at temperature T and pressure p_0 is calculated as $\Delta\bar{g}(T,p_0) = \Delta\bar{h}(T,p_0) - T\Delta\bar{s}(T,p_0)$ and finally, Eqn (2.7) is used to determine the reversible cell potential for a given set of operating temperature, pressure and reactant concentrations.

2.3 Reversible Potential

For a PEM fuel cell, the normal operating temperature range is approximately 330-350 Kelvin. In this regime, the minimum Gibb's potential for the product species is realized when liquid water is the product as compared to water vapour. Thus, the reversible potential for these temperatures is determined with liquid water being the product as this state will give a larger open circuit voltage (comparable to the Higher Heating Value).

Using the equations from the previous section, the reversible cell potential, V_{oc}, as a function of temperature and reactant partial pressures has been calculated, and some typical results are shown in Figures 2.1–2.3 for the overall reaction given by Eqn (2.6). As can be seen in Figure 2.1, the decrease in cell potential over the given temperature domain is approximately a linear function of operating temperature. This is consistent with the approximation in the Nernst equation that the entropy change, $\Delta\bar{s}(T,p_0)$, is constant. In Figures 2.2 and 2.3, the cell potential is shown to be a linear function of the logarithm of the partial pressures, and the slope of the potential versus the oxygen partial pressure is half of that for hydrogen. Figures 2.1

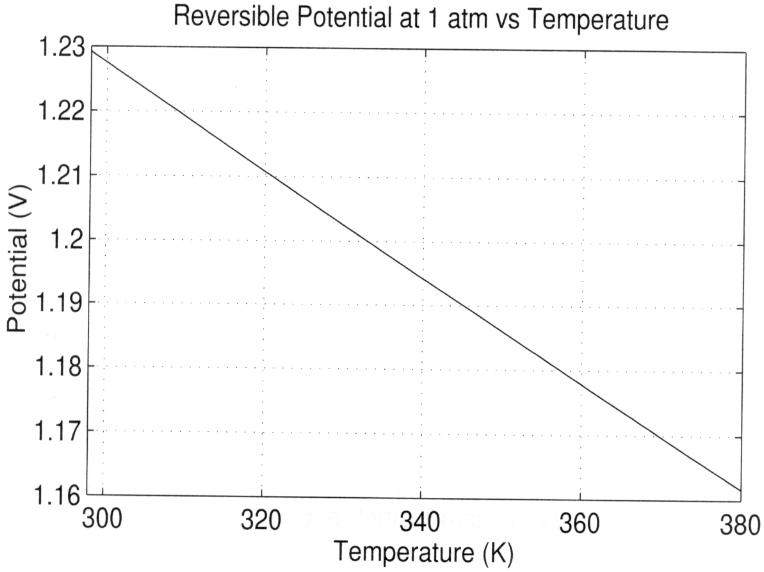

Figure 2.1: Effect of operating temperature on reversible cell potential for reaction $H_2 + \frac{1}{2}O_2 = H_2O(\ell)$ at an oxygen and hydrogen partial pressure of 1 atm.

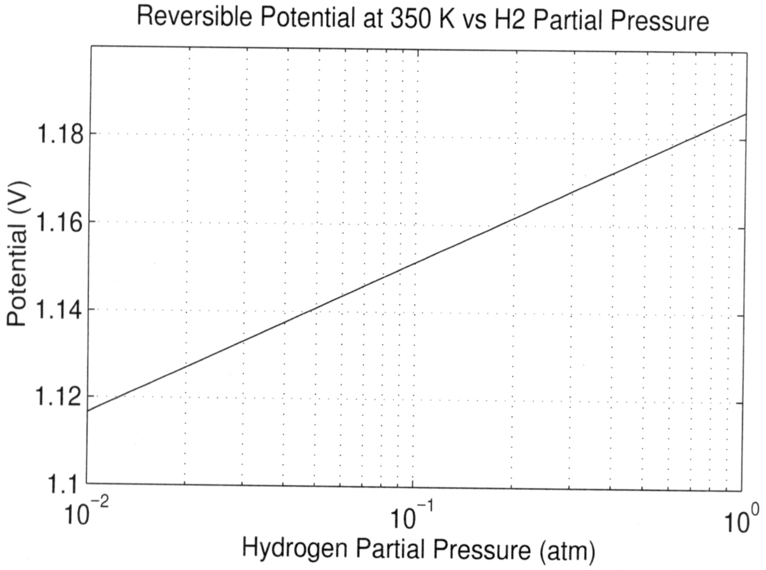

Figure 2.2: Effect of hydrogen partial pressure on reversible cell potential for cell reaction $H_2 + \frac{1}{2}O_2 = H_2O(\ell)$ at 350 K and oxygen partial pressure of 1 atm.

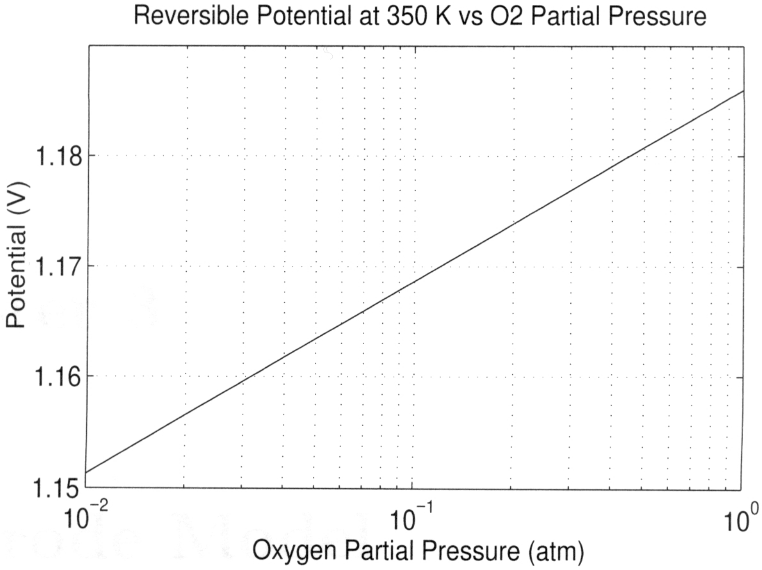

Figure 2.3: Effect of oxygen partial pressure on reversible cell potential for cell reaction $H_2 + \frac{1}{2}O_2 = H_2O(\ell)$ at 350 K and hydrogen partial pressure of 1 atm.

- 2.3 provide a benchmark to which a cell's actual performance can be compared.

Chapter 3

Electrode Model

3.1 Introduction

In this thesis the electrode region consists of the gas transport substrate only which serves the purposes of current collection and gas transport medium. Typical electrodes available commercially are made of a carbon-cloth or carbon-paper support that is impregnated with a mixture of wet-proofing agent, such as PTFE, and carbon particles. Further, the electrode structure often incorporates a layer of platinum black or platinum supported catalyst. It is in this region that the electrochemical reaction occurs; thus, the catalyst layer is modeled as a separate layer and is described in the next chapter.

The aim of the electrode model is to quantify the effects of specified operating conditions on heat and mass transfer of the gaseous species in the porous electrode. The influence of temperature distribution and species mass flux is of importance in determining the resulting cell polarization. In this region of the cell the effects of flooding can limit transport of gaseous components. Modeling the effects of energy flux is important in understanding the transport of water as vapour and liquid. As water management is an important aspect of PEM fuel cell design and operation, practical insights may be gained from a model incorporating the effects of water vaporization in the electrode backing.

3.2 Assumptions

The assumptions used in formulating the electrode model are:

1. steady-state operation,
2. one dimensional: the high aspect ratio of a cell makes this a reasonable simplification,
3. perfect gases: valid for the temperature and pressure range being considerd,
4. 100% Faradaic efficiency: cross-over and corrosion are assumed to be insignificant

5. viscous effects are negligible: the primary means of gas transport is diffusion,
6. negligible total pressure gradient: consistent with the previous assumption,
7. Soret, Dufour, and radiation effects are negligible: low temperature and concentration gradients make these phenomena insignificant,
8. no body forces: physically insignificant as compared to other driving forces,
9. no reaction of species: due to separation of the catalyst layer model from the electrode model,
10. kinetic energy is insignificant: velocities are low,
11. constant transport parameters: a suitable first assumption assuming that the temperature gradient across the cell is small.

3.3 Mathematical Formulation

The mathematical model of the various transport processes occuring in the electrode is formulated by applying the conservation equations for an ideal gas in a porous media. Specifically, the conservation of species and energy in differential form are applied, as is the Stefan-Maxwell equation for multi-component gas diffusion and

Fourier's law for heat conduction. The governing equations are:

$$\text{Species:} \qquad \nabla\cdot(\rho_i\vec{v} + \vec{j}_i) = w_i \tag{3.1}$$

$$\text{Energy:} \qquad \rho\vec{v}\cdot\nabla u = -\nabla\cdot\vec{q} + \tau_{ij} : \nabla\vec{v} - p\nabla\cdot\vec{v} + \dot{q}_s \tag{3.2}$$

$$\text{with,} \qquad \vec{j}_i = \rho_i\vec{V}_i, \tag{3.3}$$

$$\vec{q} = -k^{\text{eff}}\nabla T + \rho\sum_{i=1}^{N} h_i Y_i \vec{V}_i \tag{3.4}$$

where ρ_i is the partial density of species i, $\vec{v}$ is the mass-averaged velocity and $\vec{V}_i$ is the species diffusion velocity, u is the internal energy, $\vec{q}$ is the heat flux, τ_{ij} is the deviatoric stress tensor, p is absolute pressure, k^{eff} is the effective thermal conductivity, h_i is the specific enthalpy, and Y_i is the mass fraction of species i. The terms w_i and $\dot{q}_s$ are a mass source term and an energy source term, respectively. These terms account for species reaction or, in this case, the addition of mass and energy to the gas mixture due to the vaporization of liquid water and joule heating due to current flow.

The sum of the individual species equations gives the overall continuity equation for the gas mixture,

$$\text{Continuity:} \qquad \nabla\cdot(\rho\vec{v}) = \sum_{i=1}^{N} w_i, \tag{3.5}$$

and the diffusion velocity, $\vec{V}_i$, can be determined from the Stefan-Maxwell equation for multi-component gas diffusion,

$$\nabla x_i = \sum_{j=1}^{N} \left(\frac{x_i x_j}{D_{ij}^{\text{eff}}} \right) (\vec{V}_j - \vec{V}_i) \tag{3.6}$$

where D_{ij}^{eff} is the effective binary diffusion coefficient for species i in j. This equation can also describe the variation in gas composition.

3.3.1 Cathode Formulation

The oxidant used in terrestrial applications of PEM fuel cells is almost invariably humidified air. By applying the assumptions listed in Section 3.2, letting the index i represent the gas species in the cathodic electrode in the following manner: $1 = O_2$, $2 = N_2$, $3 = H_2O(g)$ (the subscript ℓ will represent liquid water), the conservation equations become:

Species:

$$\frac{d}{dx}[\rho_1(v + V_1)] = 0 \tag{3.7}$$

$$\frac{d}{dx}[\rho_2(v + V_2)] = 0 \tag{3.8}$$

$$\frac{d}{dx}[\rho_3(v + V_3)] = w_3 \tag{3.9}$$

$$\frac{d}{dx}[\rho_\ell v_\ell] = -w_3 \tag{3.10}$$

Continuity:

$$\frac{d}{dx}(\rho v) = 0 \tag{3.11}$$

$$\text{Energy:} \qquad \rho v\frac{du}{dx} + \frac{d}{dx}\left(\sum_{i=1}^{N}\rho_i h_i V_i\right) + p\frac{dv}{dx} = \frac{d}{dx}\left(k^{\text{eff}}\frac{dT}{dx}\right) + \dot{q}_s \tag{3.12}$$

where, $\rho_\ell v_\ell$, is the mass flux of liquid water. As nitrogen is an inert species in the gas mixture and assuming the dissolution of nitrogen in water and membrane is negligible, the absolute velocity of nitrogen at the electrode-catalyst layer interface will be zero. This boundary condition, $v + V_2 = 0$, combined with Eqn (3.8), sets the absolute velocity of species 2 equal to zero everywhere in the electrode.

Using the thermodynamic relation,

$$h = u + \frac{p}{\rho} \tag{3.13}$$

and converting the velocity terms for the gaseous species to absolute velocities by,

$$v_i = v + V_i, \tag{3.14}$$

where v_i is the absolute velocity of component i, allows the species and energy equations to be simplified as follows:

$$\text{Species:} \qquad \frac{d}{dx}(\rho_1 v_1) = 0 \tag{3.15}$$

$$v_2 = 0 \tag{3.16}$$

$$\frac{d}{dx}(\rho_3 v_3) = w_3 \tag{3.17}$$

$$\frac{d}{dx}(\rho_\ell v_\ell) = -w_3 \tag{3.18}$$

Continuity: $$\frac{d}{dx}(\rho v) = 0 \tag{3.19}$$

Energy: $$\rho_1 v_1 \frac{dh_1}{dx} + \frac{d}{dx}(\rho_3 v_3 h_3 + \rho_\ell v_\ell h_\ell) = \frac{d}{dx}\left(k^{\text{eff}} \frac{dT}{dx}\right) + \dot{q}_s \tag{3.20}$$

The Stefan-Maxwell equations can be simplified in the same manner by using the absolute velocities and noting that, $x_1 + x_2 + x_3 = 1$.

$$\frac{dx_1}{dx} = \frac{x_1 x_2}{D_{12}^{\text{eff}}}(-v_1) + \frac{x_1 x_3}{D_{13}^{\text{eff}}}(v_3 - v_1) \tag{3.21}$$

$$\frac{dx_3}{dx} = \frac{x_1 x_3}{D_{13}^{\text{eff}}}(v_1 - v_3) + \frac{x_2 x_3}{D_{23}^{\text{eff}}}(-v_3) \tag{3.22}$$

$$x_2 = 1 - x_1 - x_3. \tag{3.23}$$

Combined with Eqn (3.7), the oxygen flux can be determined at all locations in the electrode by applying the boundary condition for the oxygen flux at the catalyst layer,

$$\rho_1 v_1 = \frac{IW_1}{nF} = constant, \tag{3.24}$$

or, $$N_1 = \frac{I}{nF} \tag{3.25}$$

where I is the cell load current per geometric cell area, W_1 is the molar mass of species

1, and n is the moles of electrons consumed or produced per mole of species 1 (see Chapter 4). Thus, in terms of mole fluxes, the conservation equations reduce to:

$$\text{Species:} \qquad N_1 = \frac{I}{nF} \tag{3.26}$$

$$N_2 = 0 \tag{3.27}$$

$$\frac{d}{dx}(N_3) = \frac{w_3}{W_3} \tag{3.28}$$

$$\frac{d}{dx}(N_\ell) = -\frac{w_3}{W_3} \tag{3.29}$$

$$\text{Energy:} \qquad \left[\left(\frac{I}{nF}\right) W_1 c_{p1} + N_3 W_3 c_{p3g} + N_\ell W_3 c_{p3\ell}\right] \frac{dT}{dx} - k^{\text{eff}} \frac{d^2T}{dx^2} = -h_{\text{vap}} w_3 + \frac{I^2}{\sigma} \tag{3.30}$$

where the source term, $\dot{q}_s$, is replaced by an expression describing the Joule heating and the subscripts g and ℓ signify gas and liquid respectively. I is the cell current density, h_{vap} is the enthalpy of vaporization and σ is the electronic conductivity of the electrode. As can be seen, in the energy equation the effective thermal conductivity is assumed constant which is consistent with assumption 10. The equation describing liquid flux can be removed by noting that,

$$N_3 + N_\ell = N_3^{\text{ele}} = \text{constant}. \tag{3.31}$$

In the anode electrode, the total flux of water is determined by the conditions across the membrane as described in Chapter 5. For the cathode, the total flux is determined by the flux across the membrane and the rate of water generation.

By applying the perfect gas equation the diffusion equations become,

$$\begin{aligned}\frac{dx_1}{dx} &= \frac{RT}{p}\left[\frac{x_1N_3 - x_3N_1}{D_{13}^{\text{eff}}} - \frac{x_2N_1}{D_{12}^{\text{eff}}}\right] && (3.32)\\ \frac{dx_3}{dx} &= \frac{RT}{p}\left[\frac{x_3N_1 - x_1N_3}{D_{13}^{\text{eff}}} - \frac{x_2N_3}{D_{23}^{\text{eff}}}\right] && (3.33)\\ x_2 &= 1 - x_1 - x_3. && (3.34)\end{aligned}$$

Before formulating an expression for the mass source term, w_3, one more equation is required in order to describe the potential variation in the electronic current flow. This loss is described by an ohmic expression,

$$-\nabla\Phi_s = \frac{I}{\sigma^{\text{eff}}}. \qquad (3.35)$$

where Φ_s is the potential of the electrons in the electrode solid and σ^{eff} is the effective electronic conductivity.

3.3.2 Mass Source Term

To complete the mathematical description of the transport of heat and mass by the gas in the porous electrode, the source term, w_3 needs to be determined in terms of the temperature, mole fractions, and species velocities.

The mass (and energy) source is a result of liquid water vaporization or condensation. A driving potential for vaporization occurs due to a difference in chemical potential for water in the vapour form and water in the liquid form. Assuming this potential can be described by the difference between the partial density of saturated air and the partial density of the existing water vapour in the electrode, an expression for the mass source is then,

$$w_3 = h_m(\rho_{3,sat} - \rho_3), \tag{3.36}$$

where the term h_m is the mass transfer coefficient. The saturation partial density for water can be described as a function of temperature and pressure by the perfect gas equation of state.

$$\rho_{3,sat} = \frac{p_{sat} W_3}{RT} \tag{3.37}$$

The mass transfer coefficient, h_m, is calculated from a Sherwood number correlation as follows:

$$h_m = \mathrm{sh} \frac{D_{vg}^{\mathrm{eff}}}{L} f_e \tag{3.38}$$

$$\text{and,} \qquad f_e = \frac{\text{Surface Area of Water}}{\text{Volume of Electrode}}$$

where, L is the characteristic length scale, D_{vg}^{eff} is the effective diffusion coefficient of water vapour in the gas mixture, and sh is the Sherwood number. Rewriting Eqn (3.36) in terms of the Sherwood number and using the mole fraction gives,

$$\text{Mass Source:} \qquad w_3 = \text{sh}\frac{D_{v,g}^{\text{eff}}}{L} f_e \frac{pW_3}{RT}\left(\frac{p_{sat}}{p} - x_3\right) \tag{3.39}$$

Equation (3.39) defines the mass source in terms of the mole fraction, the temperature, and the absolute pressure.

3.3.3 Anode Formulation

The mathematical description of the anode is similar to the analysis performed for the cathode. The only difference is, that in the case of the anode the values of the index i are defined as $1 = H_2$, $2 = CO_2$, and $3 = H_2O(g)$. It should also be noted that for a reaction rate set by I, the mole flux of hydrogen is twice that of oxygen. This fact is taken into account in the governing equations by the parameter n. Using the same assumptions described in Section 3.2, the resulting anode model is mathematically similar to the cathode.

3.4 Summary of Governing Equations

At this point it is of some use to summarize the governing equations for the electrodes and to list the dependent variables.

$$\text{Fraction 1:}\quad \frac{dx_1}{dx} = \frac{RT}{p}\left[\frac{x_1N_3 - x_3N_1}{D_{13}^{\text{eff}}} - \frac{x_2N_1}{D_{12}^{\text{eff}}}\right] \tag{3.40}$$

$$\text{Fraction 3:}\quad \frac{dx_3}{dx} = \frac{RT}{p}\left[\frac{x_3N_1 - x_1N_3}{D_{13}^{\text{eff}}} - \frac{x_2N_3}{D_{23}^{\text{eff}}}\right] \tag{3.41}$$

$$\text{Fraction 2:}\quad x_2 = 1 - x_1 - x_3 \tag{3.42}$$

$$\text{Energy:}\quad \left[\left(\frac{I}{nF}\right)W_1c_{p1} + N_3W_3c_{p3g} + (N_3^{\text{ele}} - N_3)W_3c_{p3\ell}\right]\frac{dT}{dx} - k^{\text{eff}}\frac{d^2T}{dx^2} + h_{\text{vap}}w_3 - \frac{I^2}{\sigma^{\text{eff}}} = 0 \tag{3.43}$$

$$\text{Vapour Flux:}\quad \frac{d}{dx}(N_3) = \frac{w_3}{W_3} \tag{3.44}$$

$$\text{Mass Source:}\quad w_3 = \text{sh}\frac{D_{vg}^{\text{eff}}}{L}f_e\frac{pW_3}{RT}\left(\frac{p_{sat}}{p} - x_3\right) \tag{3.45}$$

$$\text{Potential:}\quad \frac{d\Phi_s}{dx} = -\frac{I}{\sigma^{\text{eff}}} \tag{3.46}$$

As can be seen, for the electrode layer there are seven equations for seven unknowns: x_1, x_2, x_3, T, N_3, w_3 and Φ_s. This set of equations can be reduced to four, coupled, non-linear differential equations by substituting in the expressions for x_2 and w_3; however, for clarity this is not done here. In this form, these seven equations describe the anode electrode as well as the cathode electrode; however, the cathode co-ordinate system is reversed and so the flux of oxygen is negative (See Figure 1.1).

3.5 Non-dimensionalization

The governing equations listed above and their associated variables, are normalized for ease of manipulation and interpretation. Since the equations are written using molar fractions, the only non-dimensional variables established are:

$$x^* = \frac{x-t_j}{t_e} \quad T^* = \frac{T-T_c}{\Delta T} \quad N_i^* = \frac{N_i}{\frac{I}{nF}} \quad \Phi^* = \frac{\Phi}{V_{oc}}$$

where x^* is the non-dimensional distance, t_e is the electrode thickness and t_j is the position of the beginning of the electrode backing layer, T^* is the non-dimensional temperature, T_c is the specified cell operating temperature (a boundary condition), ΔT is a characteristic temperature difference, N^* is the non-dimensional flux of gaseous species i, I/nF is recognized to be the mole flux of species 1, and V_{oc} is the open circuit (reversible) cell potential. Because the boundaries of the cell are assumed to be at a known temperature, T_c, a characteristic temperature difference is arbitrarily set.

Substituting the above variables into the governing equations allows the designation of the following non-dimensional parameters:

$$\bar{E}_1 = \frac{\Delta T}{T_c} \tag{3.47}$$

$$\bar{E}_2 = \frac{I}{nF}\frac{RT_c}{p}\frac{t_e}{D_{13}^{\mathrm{eff}}} \tag{3.48}$$

$$\begin{aligned}
\bar{E}_3 &= \frac{I}{nF}\frac{RT_c}{p}\frac{t_e}{D_{12}^{\text{eff}}} && (3.49)\\
\bar{E}_4 &= \frac{I}{nF}\frac{RT_c}{p}\frac{t_e}{D_{23}^{\text{eff}}} && (3.50)\\
\bar{E}_5 &= \frac{I}{nF}\frac{c_{p1}}{k^{\text{eff}}}W_1 t_e && (3.51)\\
\bar{E}_6 &= \frac{I}{nF}\frac{c_{p3g}}{k^{\text{eff}}}W_3 t_e && (3.52)\\
\bar{E}_7 &= \frac{I}{nF}\frac{c_{p3\ell}}{k^{\text{eff}}}W_3 t_e && (3.53)\\
\bar{E}_8 &= N_3^{\text{ele}}\frac{c_{p3\ell}}{k^{\text{eff}}}W_3 t_e && (3.54)\\
\bar{E}_9 &= \frac{I}{nF}\frac{h_{\text{vap}}}{k^{\text{eff}}\Delta T}W_3 t_e && (3.55)\\
\bar{E}_{10} &= \frac{I^2 t_e^2}{\sigma^{\text{eff}}\Delta T k^{\text{eff}}} && (3.56)\\
\bar{E}_{11} &= \frac{\text{sh}\, t_e f_e}{\frac{I}{nF}\frac{RT_c}{p}\frac{L}{D_{vg}}}. && (3.57)
\end{aligned}$$

The governing differential equations in non-dimensional form are:

Fraction 1:
$$\frac{dx_1}{dx^*} = (\bar{E}_1 T^* + 1) \quad (3.58)$$
$$\left[\bar{E}_2(x_1 N_3^* - x_3 N_1^*) + \bar{E}_3(x_1 N_1^* + x_3 N_1) - \bar{E}_3 N_1^*\right]$$

Fraction 3:
$$\frac{dx_3}{dx^*} = (\bar{E}_1 T^* + 1) \quad (3.59)$$
$$\left[\bar{E}_2(x_3 N_1^* - x_1 N_3^*) + \bar{E}_4(x_1 N_3^* + x_3 N_3) - \bar{E}_4 N_3^*\right]$$

Energy:
$$\frac{d^2 T^*}{dx^{*2}} - \left[\bar{E}_5 N_1^* + (\bar{E}_6 - \bar{E}_7)N_3^* + \bar{E}_8\right]\frac{dT^*}{dx^*} \quad (3.60)$$
$$-\bar{E}_9\frac{dN_3^*}{dx} + \bar{E}_{10} = 0$$

$$\text{Vapour Flux:} \qquad \frac{dN_3^*}{dx^*} - \frac{\bar{E}_{11}}{\bar{E}_1 T^* + 1}\left(\frac{p_{sat}}{p} - x_3\right) = 0 \tag{3.61}$$

The equations describing the mass source term and the mole fraction x_2 have been substituted in to reduce the number of equations; furthermore, the equation describing the potential variation is not included as this equation is not coupled with the others.

Chapter 4

Catalyst Layer Model

4.1 Introduction

Although the catalyst layer is a relatively small part of the cell, it is the heart of the fuel cell energy transformation mechanism. Here the fuel and oxidant react electrochemically to produce electrical work. In this portion of the cell, the transfer of mass and energy is coupled with reaction kinetics and results in a potential difference between electrodes. How this potential difference varies as a function of mass transfer, electrode kinetics, and energy flux determines the characteristic power curve of a cell.

In contemporary PEM fuel cells, the catalyst layer usually consists of small particles of platinum catalyst supported on larger carbon particles. This reactive zone can also include membrane material that has been impregnated into the layer to increase the three-dimensional reaction area, and PTFE to act as a wet-proofing agent. The composition, morphology, and layer thickness are critical in determining the performance of a cell and also the resulting cost of catalyst. Extensive research in catalyst layer morphology is being conducted in hopes of reducing the amount of precious metal catalyst required, decreasing polarizations in the layer and also finding materials that will resist poisoning by carbon monoxide in the fuel stream.

In this thesis the catalyst layer is assumed to be a mixture of membrane, catalyst and void space. The volume fractions of these components can be varied as can the effective surface area of catalyst that is characterized by different loadings and catalyst types.

The aim of the catalyst layer model is to mathematically describe the transport of dissolved reactants, ions, and water in the reaction zone and the resulting effect on cell potential. The production of heat due to reaction and irreversibilities is modeled to determine the effects of energy transfer on polarization and temperature.

4.2 Assumptions

The following assumptions are used in formulating the catalyst layer model:

1. the cathode catalyst layer is fully hydrated: this is where water is produced in

an acidic fuel cell,

2. the anode catalyst layer hydration is a function of water vapour activity: a similar assumption is used by Springer et al. [12],
3. membrane hydration is invariable across the layer: may not be valid, however this is a reasonable first assumption,
4. the layer thickness is uniform: a necessarry assumption for one-dimensional model,
5. the catalyst distribution is uniform: this is usually the design goal of electrode manufacturers,
6. the dissolution of reactant gases follows Henry's law: valid for an ideal solution,
7. the pressure gradient is negligible across the layer: true if diffusion is the primary means of gas transport, and
8. the dissolution of nitrogen or carbon dioxide is negligible: Henry's constant for nitrogen in aqueous solutions is approximately half of that for oxygen; carbon dioxide is more soluble than hydrogen in water. If these quantities are similar for dissolution in membrane, then the anode side may have to include the possibility of a flux of species 2 (of concern when operating with CO_2 in the gas stream).

The assumption that there is no pressure drop across the catalyst layer implies that the pressure difference between the two electrodes is maintained by the membrane portion only. Because the catalyst layer is much thinner than the membrane layer, and is porous, this approximation is qualitatively valid.

4.3 Mathematical Formulation

The mathematical description of the catalyst layer is formulated by the application of the conservation equations, the Butler-Volmer equation for chemical reaction, the Nernst-Planck equation for flux of aqueous species, Electroneutrality, and Fourier's law for heat conduction. The second law is used to quantify heat production due to reversible mechanisms. The development for this portion of the cell model is similar to that of Bernardi and Verbrugge [7]; however, in this case, the energy equation is also included. The conservation equations for the catalyst layer are:

$$\text{Species:} \qquad \nabla \cdot \vec{N}_i = -\frac{\nu_i j(x)}{nF} \tag{4.1}$$

$$\text{Energy:} \qquad \nabla \cdot \vec{q} + \nabla \cdot \sum_{i=1}^{S} \vec{N}_i h_i W_i + \dot{w} = \dot{q}_s. \tag{4.2}$$

The term N_i is the molar flux of species i, S is the number of species including ions, $\dot{w}$ is the electrical work rate per unit volume, $\dot{q}_s$ is an energy source term per unit volume, and $j(x)$ is the rate of reaction per unit volume. Furthermore, the values for ν_i and n correspond to the coefficients for the half-cell reactions written in the following form,

$$\sum_{i=1}^{S} \nu_i M_i^{z_i} \rightarrow ne^- \tag{4.3}$$

where $M_i^{z_i}$ is species i with charge z_i.

Additionally, the constitutive relations of importance are listed below:

$$\text{Current:} \quad \vec{i} = F \sum_{i=1}^{Sc} z_i \vec{N}_i \tag{4.4}$$

where $\vec{i}$ is the net current in the layer, and S_c is the number of ionic species. For a PEM cell the only mobile charged ion is $H+$, hence, $\vec{i}$ is the protonic current.

$$\text{Butler-Volmer:} \; j(x) = a i_0 \left[\exp\left(\frac{\alpha_a F \eta_a}{RT}\right) - \exp\left(-\frac{\alpha_c F \eta_a}{RT}\right)\right] \tag{4.5}$$

where,

$$i_0 = i_0^{\text{ref}} \left(\frac{c_1}{c_1^{\text{ref}}}\right)^{\gamma_1} \left(\frac{c_{H+}}{c_{H+}^{\text{ref}}}\right)^{\gamma_{H+}} . \tag{4.6}$$

The Butler-Volmer equation describes the electrochemical reaction rate in terms of,

a, the active surface area per unit volume, i_0 the exchange current density of a half cell in equilibrium, α_a and α_c the apparent transfer coefficients for the reaction in an anodic and cathodic direction respectively, and η_a the activation polarization. This term is of particular importance as its magnitude is a measure of how fast a reaction is. Typically, the reaction at the cathode is slow and therefore requires a higher polarization than the anode does to satisfy a given current density. In Eqn (4.6), 1 represents the reactant species which is hydrogen at the anode and oxygen at the cathode. The exchange current density is a function of the reactant concentrations, c, where c^{ref} is the concentration for the reference exchange current density i_0^{ref}. The superscripts γ_1 and γ_{H+} are functions of their respective reaction orders and apparent transfer coefficients as described in detail by Newman [18]. Essentially, for a rate-limiting reaction written in the form of Eqn (4.3), the exponent γ_1 is given by,

$$\gamma_1 = q_i + \beta \nu_i, \tag{4.7}$$

where

$$\begin{aligned} q_i &= |\nu_i| \qquad \text{for } \nu_i < 0, \\ q_i &= 0 \qquad \text{for } \nu_i > 0. \end{aligned} \tag{4.8}$$

The coefficient β is the symmetry factor and is often taken to be 0.5. Experimental evidence suggests that this value may be inappropriate for the cathodic reaction at an operating temperature of 350 K [19].

$$\text{Nernst-Planck:} \quad \vec{N_i} = -z_i F D_i \frac{c_i}{RT} \nabla \Phi_m - D_i \nabla c_i + c_i \vec{v} \tag{4.9}$$

The Nernst-Planck equation describes the absolute molar flux of dissolved species resulting from diffusion, migration due to charge, and convection, where Φ_m is the potential in the membrane and D_i is the diffusion coefficient for species i in the membrane.

For a macroscopic portion of the cell, there is no net charge,

$$\text{Electroneutrality:} \quad \sum_{i=1}^{S_c} z_i c_i = 0. \tag{4.10}$$

Finally, the potential gradient in the catalyzed solid is determined by Ohm's law,

$$\text{Ohm's law:} \quad i_s = -\sigma^{\text{eff}} \frac{d\Phi_s}{dx}, \tag{4.11}$$

where, σ^{eff} is the effective conductivity of the solid phase.

4.3.1 Energy Equation

The energy equation for the catalyst layer requires that the divergence in the enthalpy fluxes for all species be accounted for, including the protons and electrons. Newman [18] describes how the ionic species are included in the enthalpy divergence term where the divergence of ionic enthalpy flux results in Joule heating:

$$-\vec{N}_i \cdot \nabla \bar{h}_i = \frac{\vec{i} \cdot \vec{i}}{\kappa}. \tag{4.12}$$

The term on the right-hand side of Eqn (4.12) quantifies the effects of Joule heating in the familiar $i^2 \cdot r$ form where κ is the conductivity and $\bar{h}_i$ is the molar enthalpy of ionic species i.

The heat source term, $\dot{q}_s$, in Eqn (4.2) accounts for irreversible losses other than Joule heating. For an electrochemical cell at a temperature T, the reversible heat production is due to the reversible entropy change for the reaction, $T\Delta\bar{s}$. The electrical work term, $\dot{w}$, can be expressed by the equation;

$$\dot{w} = -\Delta\dot{g} = \left|\frac{j(x)}{2F}\right| (-\Delta\bar{h} + T\Delta\bar{s}) \tag{4.13}$$

where $-\Delta\dot{g}$ is the rate of change of free energy per mole of fuel, and $\left|\frac{j(x)}{2F}\right|$ is the rate of reaction per unit volume in terms of fuel consumption.

Combining Eqns (4.2), (4.12), and (4.13) results in the following one-dimensional energy equation:

$$\frac{dq}{dx} + \sum_{i=1}^{S_{nc}} N_i W_i \frac{dh_i}{dx} + \sum_{i=1}^{S} h_i W_i \frac{dN_i}{dx} + \left| \frac{j(x)}{2F} \right| (-\Delta\bar{h} + T\Delta\bar{s}) = \frac{i^2}{\kappa^{\text{eff}}} + \dot{q}_s \tag{4.14}$$

where, S_{nc}, indicates the summation is over the non-ionic species only. Although there is current flow in both the solid phase and the membrane phase, the resistivity of the solid can be assumed to be negligible compared to that of the membrane and so the Joule heating term will be described by the current in the membrane phase only, $i_m^2/\kappa^{\text{eff}}$. The term i_m is the current in the membrane, and κ^{eff} is the effective protonic conductivity of the ionomer in the catalyst layer.

The irreversible losses resulting from activation polarization are described by,

$$\text{Activation Polarization:} \qquad j(x)\eta_a. \tag{4.15}$$

Assuming that the activation polarization term accounts for any remaining losses in the layer, Eqn (4.15) can be substituted into Eqn (4.14) in place of the heat source term.

$$\frac{dq}{dx} + \sum_{i=1}^{S_{nc}} N_i W_i \frac{dh_i}{dx} = \frac{i_m^2}{\kappa^{\text{eff}}} + \left| \frac{j(x)}{nF} \right| (-T\Delta\bar{s}) + j(x)\eta_a. \tag{4.16}$$

Here, the term $\sum_{i=1}^{S} h_i W_i \frac{dN_i}{dx}$ has been canceled by the reaction enthalpy term, $-\Delta\bar{h}$.

Using the reference scale of electrochemistry, which sets the entropy of an aqueous proton at standard state conditions as being zero, allows the half-cell reversible entropy change to be calculated. This procedure is described by Lampinen and Fomino [20], and their results show that half-cell reactions can be exothermic or endothermic relative to each other. Assuming that this arbitrary scale describes the absolute entropy changes at each electrode and that for a PEM cell the anode entropy change is approximately zero relative to the cathode, the entropy change for the net reaction may be used to describe the reversible heat generation at the cathode. However, since this is a relative scale, this procedure is somewhat ambiguous. In any case, a source term for each catalyst layer is included in the model in the form ($T\Delta\bar{s}$). The magnitude of this term can be set as an arbitrary fraction of the heat released due to the reversible entropy change of the overall cell reaction.

4.3.2 Cathode Formulation

Applying the species equation to the cathode catalyst layer where there are oxygen and protons in solution, liquid water production, and electronic current in the solid matrix, yields the conservation equations for the cathode. In molar form, the sum of the individual species equations also yields conservation of charge for the half-reaction. To use the Butler-Volmer equation to describe the rate of the cathode reaction, the rate limiting elementary reaction must be used. Like Ticiannelli, et al. [21], the cathode reaction is assumed to have a first order dependence on oxygen concentration; however, a single electron transfer seems to be involved in the slow reaction step especially in a high overpotential region [19]. To ensure that a realistic Tafel slope is modeled by the cathode reaction, the number of electrons transferred in the rate-limiting step must correspond closely to the experimentally determined value. With this in mind, an overall cathodic reaction in the form of Eqn (4.17) is modelled (i.e., first order in oxygen concentration) but, the terms α_a and α_c in the Butler-Volmer equation are set to equal unity. This gives an approximate Tafel slope of 70 mV/decade which is similar to that used by Springer, et al. [22].

$$O_2(aq) + 4H^+(aq) + 4e^-(Pt) \rightarrow 2H_2O(\ell) \tag{4.17}$$

Written in the form of Eqn (4.3) gives,

$$-O_2 - 4H^+ + 2H_2O \rightarrow 4e^-. \tag{4.18}$$

Using the subscript notation of $1 = O_2$, $2 = H^+$, and $3 = H_2O$ the transfer of species in the catalyst layer is described by Eqn (4.1),

$$\frac{dN_1}{dx} = -\frac{\nu_1 j(x)}{nF} \tag{4.19}$$

$$F\frac{dN_2}{dx} = \frac{di_m}{dx} = j(x) \tag{4.20}$$

$$\frac{dN_3}{dx} = -\frac{\nu_3 j(x)}{nF} \tag{4.21}$$

$$\frac{di_s}{dx} = -j(x). \tag{4.22}$$

The movement of uncharged dissolved species is not affected by the presence of an electrostatic field, therefore the relevant term in the Nernst-Planck equation, Eqn (4.9), can be ignored. The resulting expression is then,

$$N_1 = -D_1^{\text{eff}}\frac{dc_1}{dx} + c_1 v_3. \tag{4.23}$$

where the first term on the right is the diffusive flux due to a concentration gradient and the second term assumes the convective flux of species 1 is due to liquid water flux only. The concentration variation is then described by,

$$D_1^{\text{eff}}\frac{d^2c_1}{dx^2} - \frac{N_3}{c_3}\frac{dc_1}{dx} - \frac{c_1}{c_3}\frac{dN_3}{dx} + \frac{dN_1}{dx} = 0. \tag{4.24}$$

Using the assumptions that the membrane in the cathode layer is completely hydrated and that the ionomer is uniformly distributed, and by imposing the condition of macroscopic charge neutrality, the concentration of protons in the ionomer is fixed by the concentration of negative charge sites in the polymer. This condition is assumed to be known. The gradient of the proton concentration in the catalyst layer is then zero. Thus, the corresponding Nernst-Planck equation for proton flux is,

$$N_2 = -\frac{F}{RT} D_2^{\text{eff}} c_2 \frac{d\Phi_m}{dx} + c_2 v_3 \tag{4.25}$$

where D_2^{eff} is the effective diffusion coefficient for protons in the catalyst layer and v_3, the liquid water velocity, is equivalent to $\frac{N_3}{c_3}$. Since the cell current density is one of the independent variables for the model, this equation is in a more useful form when the gradient in potential is determined explicitly. That is,

$$\frac{d\Phi_m}{dx} = -\frac{i_m}{\kappa^{\text{eff}}} + \frac{F}{\kappa^{\text{eff}}} c_2 v_3 \tag{4.26}$$

where

$$\begin{aligned} \kappa^{\text{eff}} &= \frac{F^2}{RT} D_2^{\text{eff}} c_2 && (4.27) \\ i_m &= F N_2 && (4.28) \end{aligned}$$

Converting v_3 to a flux, N_3, results in,

$$\frac{d\Phi_m}{dx} = -\frac{i_m}{\kappa^{\text{eff}}} + \frac{F}{\kappa^{\text{eff}}} \frac{c_2}{c_3} N_3 \tag{4.29}$$

To determine the energy flux in the catalyst layer, Eqn (4.16) is written as:

$$-k^{\text{eff}}\frac{d^2T}{dx^2}+N_1W_1\frac{dh_1}{dx}+N_3W_3\frac{dh_3}{dx}=\frac{i_m^2}{\kappa^{\text{eff}}}+\left|\frac{j(x)}{nF}\right|(-T\Delta\bar{s})+j(x)\eta_a \tag{4.30}$$

where the effective thermal conductivity in the catalyst layer, k^{eff}, is assumed to be constant. It should be noted here that because of the assumption that this is an ideal solution, the partial molar enthalpy of each component is equal to the molar enthalpy of the corresponding pure component at the same temperature and pressure [17]. After expanding Eqn (4.30) and substituting in the species equations, the energy equation now becomes:

$$-k^{\text{eff}}\frac{d^2T}{dx^2}+(N_1W_1c_{p1}+N_3W_3c_{p3})\frac{dT}{dx}=\frac{i_m^2}{\kappa^{\text{eff}}}+\left|\frac{j(x)}{nF}\right|(-T\Delta\bar{s})+j(x)\eta_a \tag{4.31}$$

where the thermodynamic relation $\frac{dh}{dT}=c_p$ has been invoked.

Since the concentration of protons in the layer is fixed by the number of charge sites in the membrane, the Butler-Volmer equation can be somewhat simplified. Because the number of charge sites in a membrane is fixed, the concentration of protons in the catalyst layers is constant. Thus, the associated ratio in Eqn (4.6) is invarient and can be absorbed into the reference exchange current, i_0^{ref}. Substituting the remaining terms into Eqn (4.5) in place of the exchange current density, i_0, gives:

$$\text{Butler-Volmer:} \qquad j(x) = a i_0^{\text{ref}} \left(\frac{c_1}{c_1^{\text{ref}}}\right)^{\gamma_1} \left[\exp\left(\frac{\alpha_a F \eta_a}{RT}\right) - \exp\left(-\frac{\alpha_c F \eta_a}{RT}\right)\right] \tag{4.32}$$

A potential difference exists between the protons in solution and the electrons on the solid and is equivalent to the activation polarization, η_a, for the electrochemical reaction,

$$\eta_a = \Phi_s - \Phi_m + \text{constant} \tag{4.33}$$

where Φ_s and Φ_m are the solid potential and membrane potential respectively. The constant accounts for the surface potential due to the double-layer at equilibrium. Using this relation, the activation polarization in the energy equation and Butler-Volmer equation can be expressed in terms of potential.

By the law of electroneutrality, the current in the solid and the proton flux in the membrane are linked by,

$$\vec{i}_s + \vec{i}_m = \vec{I}, \tag{4.34}$$

where I is the load current per unit geometric cell area.

4.3.3 Anode Formulation

The anode catalyst layer is distinct from the cathode layer in that there is no production of liquid water. In this layer the species of concern are dissolved molecular hydrogen, protons in solution and water. The overall reaction at the anode is thought to consist of the adsorption of hydrogen onto the reaction site and its dissociation, and a single electron transfer (Tafel-Volmer mechanism) [23]. The slow step is assumed to be the chemical dissociation and so an overall anodic reaction for one mole of hydrogen of the following form is modelled:

$$H_2(aq) \rightarrow 2H^+ + 2e^-, \tag{4.35}$$

and written in the form of Eqn (4.3) gives,

$$H_2 - 2H^+ \rightarrow 2e^- \tag{4.36}$$

Using the indices $1 = H_2$, $2 = H^+$, and $3 = H_2O$ results in equations of the same form as the cathode layer. It should be noted that since there is no water production at the anode, the species equation for water has the form,

$$\frac{dN_3}{dx} = 0. \tag{4.37}$$

However, from the coefficients, ν_i, as determined by the form of equation Eqn (4.36), one can see that s_3 for the anode is 0 and, thus, the equation describing the water flux in the anode catalyst layer, Eqn (4.37), is obtained from Eqn (4.21). Moreover, although the hydrogen flux is twice that of oxygen for a given load current, I, this is also taken into account by n, the moles of electrons transferred per mole of species 1. In effect, by replacing the indices i with the species described above, and using the stoichiometric coefficients for the reaction described by Eqn (4.36), the formulation developed for the cathode catalyst layer also describes the anode catalyst layer.

4.4 Summary of Governing Equations

The governing equations describing electrochemical kinetics, mass, and heat transport within the catalyst layer are summarized below:

$$\text{Flux 1:} \quad \frac{dN_1}{dx} = \frac{-\nu_1 j(x)}{nF} \tag{4.38}$$

$$\text{Flux 2:} \quad \frac{di_m}{dx} = j(x) \tag{4.39}$$

$$\text{Flux 3:} \quad \frac{dN_3}{dx} = \frac{-\nu_3 j(x)}{nF} \tag{4.40}$$

$$\begin{aligned} \text{Energy:} \quad & -k^{\text{eff}} \frac{d^2T}{dx^2} + (N_1 c_{p1} W_1 + N_3 c_{p3} W_3) \frac{dT}{dx} + \left| \frac{j(x)}{nF} \right| [T \Delta \bar{s}] \\ & = j(x)(\Phi_s - \Phi_m) + \frac{i_m^2}{\kappa^{\text{eff}}} \end{aligned} \tag{4.41}$$

$$\text{Butler-Volmer:} \quad j(x) = a i_0^{\text{ref}} \left(\frac{c_1}{c_1^{\text{ref}}} \right)^{\gamma_1} \left[\exp \left(\frac{\alpha_a F}{RT} (\Phi_s - \Phi_m) \right) \right.$$

$$- \exp\left(-\frac{\alpha_c F}{RT}(\Phi_s - \Phi_m)\right)\Big] \tag{4.42}$$

$$\text{Concentration:} \quad D_1^{\text{eff}}\frac{d^2c_1}{dx^2} - \frac{N_3}{c_3}\frac{dc_1}{dx} - \frac{c_3}{c_3}\frac{dN_3}{dx} + \frac{dN_1}{dx} = 0. \tag{4.43}$$

$$\text{Potential:} \quad \frac{d\Phi_m}{dx} = -\frac{i_m}{\kappa^{\text{eff}}} + \frac{F}{\kappa^{\text{eff}}}\frac{c_2}{c_3}N_3 \tag{4.44}$$

$$\text{Ohm's law:} \quad i_s = -\sigma^{\text{eff}}\frac{d\Phi_s}{dx}. \tag{4.45}$$

There are seven, non-linear, differential equations for seven unknowns: N_1, i_m, N_3, T, c_1, Φ_m and Φ_s.

4.5 Non-dimensionalization

The above equations are non-dimensionalized using the following definitions:

$$x^* = \tfrac{x-t_j}{t_l} \quad T^* = \tfrac{T-T_c}{\Delta T} \quad i^* = \tfrac{i_m}{I} \quad j(x)^* = \tfrac{j(x)}{ai_0^{\text{ref}}}$$

$$N_{1l}^* = \tfrac{N_{1l}}{\frac{I}{nF}} \quad N_{3l}^* = \tfrac{N_{3l}}{\frac{I}{2F}} \quad c_{1l}^* = \tfrac{c_1}{c_1^{\text{ref}}} \quad \Phi^* = \tfrac{\Phi}{V_{oc}}$$

where t_l is the catalyst layer thickness, t_j is the position of the catalyst layer-membrane interface, V_{oc} is the theoretical open-circuit potential for the specified operating conditions, I/nF is the molar consumption rate of species 1, and $I/2F$ is the molar rate of water generation per unit geometric area. Substituting these variables into the governing equations produces the following non-dimensional parameters:

$$\bar{L}_1 = \nu_1 t_l \frac{ai_0^{\text{ref}}}{I} \tag{4.46}$$

$$\bar{L}_2 = \frac{\nu_2}{n} t_l \frac{a i_0^{\mathrm{ref}}}{I} \tag{4.47}$$

$$\bar{L}_3 = \frac{2\nu_3}{n} t_l \frac{a i_0^{\mathrm{ref}}}{I} \tag{4.48}$$

$$\bar{L}_4 = \frac{I W_1}{nF} \frac{c_{p1}}{k^{\mathrm{eff}}} t_l \tag{4.49}$$

$$\bar{L}_5 = \frac{I W_3}{nF} \frac{c_{p3}}{k^{\mathrm{eff}}} t_l \tag{4.50}$$

$$\bar{L}_6 = \frac{I^2 t_l^2}{\kappa^{\mathrm{eff}} \Delta T k^{\mathrm{eff}}} \tag{4.51}$$

$$\bar{L}_7 = t_l^2 \frac{V_{oc} a i_0^{\mathrm{ref}}}{k^{\mathrm{eff}} \Delta T} \tag{4.52}$$

$$\bar{L}_8 = \frac{a i_0^{\mathrm{ref}}}{nF} \frac{t_l^2}{k^{\mathrm{eff}} T} [T \Delta \bar{s}] \tag{4.53}$$

$$\bar{L}_9 = \frac{I}{2F} \frac{t_l}{D_1^{\mathrm{eff}} c_3} \tag{4.54}$$

$$\bar{L}_{10} = \frac{I}{nF} \frac{t_l}{D_1^{\mathrm{eff}} c_1^{\mathrm{ref}}} \tag{4.55}$$

$$\bar{L}_{11} = \frac{I t_l}{V_{oc} \kappa^{\mathrm{eff}}} \tag{4.56}$$

$$\bar{L}_{12} = \frac{t_l}{\kappa^{\mathrm{eff}}} \frac{c_2}{c_3} \frac{I}{2V_{oc}} \tag{4.57}$$

$$\bar{L}_{13} = \frac{F}{RT} V_{oc} \tag{4.58}$$

$$\bar{L}_{14} = \frac{\Delta T}{T_c} \tag{4.59}$$

$$\bar{L}_{15} = \frac{I t_l}{V_{oc} \sigma^{\mathrm{eff}}}. \tag{4.60}$$

As will be shown in Chapter 5, the ratio c_2/c_3 is equal to $1/\lambda$, where λ is the membrane hydration.

Using the parameters above and the non-dimensional variables, the governing equations for the catalyst layer in non-dimensional form are:

$$\text{Flux 1:}\quad \frac{dN^*_{1l}}{dx^*} + \bar{L}_1 j(x)^* = 0 \tag{4.61}$$

$$\text{Flux 2:}\quad \frac{di^*_m}{dx^*} + \bar{L}_2 j(x)^* = 0 \tag{4.62}$$

$$\text{Flux 3:}\quad \frac{dN^*_{3l}}{dx^*} + \bar{L}_3 j(x)^* = 0 \tag{4.63}$$

$$\begin{aligned}\text{Energy:}\quad & \frac{d^2T^*}{dx^{*2}} - (\bar{L}_4 N^*_{1l} + \bar{L}_5 N^*_{3l})\frac{dT^*}{dx^*} - \bar{L}_8 |j(x)^*| \\ & + \bar{L}_7 j(x)^* (\Phi^*_s - \Phi^*_m) + \bar{L}_6 i^{*2} = 0\end{aligned} \tag{4.64}$$

$$\begin{aligned}\text{Butler-Volmer:}\quad j(x)^* = {c^*_{1l}}^{\gamma_1} \Bigg[& \exp\left(\frac{\alpha_a \bar{L}_{13}(\Phi^*_s - \Phi^*_m)}{\bar{L}_{14}T^* + 1}\right) \\ & - \exp\left(-\frac{\alpha_c \bar{L}_{13}(\Phi^*_s - \Phi^*_m)}{\bar{L}_{14}T^* + 1}\right)\Bigg]\end{aligned} \tag{4.65}$$

$$\text{Concentration:}\quad \frac{d^{*2}c^*_{1l}}{dx^{2*}} - \bar{L}_9 N^*_{3l}\frac{dc^*_{1l}}{dx^*} + (\bar{L}_9 \bar{L}_3 c^*_{1l} - \bar{L}_{10}\bar{L}_1) j(x)^* = 0 \tag{4.66}$$

$$\text{Mem Potential:}\quad \frac{d\Phi^*_m}{dx^*} + \bar{L}_{11} i^*_m - \bar{L}_{12} N^*_{3l} = 0 \tag{4.67}$$

$$\text{Solid Potential:}\quad \frac{d\Phi^*_s}{dx^*} + \bar{L}_{15}(1 - i^*_m) = 0. \tag{4.68}$$

Chapter 5

Membrane Model

5.1 Introduction

The categorization of fuel cells is usually based upon the type of electrolyte; for a PEM fuel cell, a perfluorosulfonate polymer membrane acts as the hydrogen ion conductor. Several different companies manufacture membranes for fuel cell applications; however, at the moment, the Nafion membrane of Dupont appears to be the polymer most widely used in published literature. While the various brands of membrane have differing characteristics, it is important to note that they all seem to exhibit minimum resistance when saturated with water.

The aim of the membrane model is to mathematically describe the flux of protons, water, and energy through the membrane layer. With knowledge of these fluxes, the effect on cell potential can be calculated. Of particular importance in this region is the transport of liquid water. It is well known that the transport properties of perfluorosulfonic membranes are intimately related to the degree of membrane hydration, λ. The hydration is a measure of the amount of liquid water held in the membrane pores and is calculated as the ratio of the number of water molecules to the number of charge sites. The degree of hydration a membrane exhibits is greatly affected by preparation, treatment procedures, temperature, and whether it is equilibriated with liquid water or water vapour. It has been found experimentally that the hydration can vary from a low value of 2 to a high value of approximately 26 for a Nafion 117 membrane hydrated in boiling water; however, when equilibrated in saturated water vapour, λ tends not to exceed approximately 14 [24]. The exact reasons for this behaviour are, as of yet, unknown and this phenomenon is refered to as Schroeder's paradox. This introduces some difficulties in accurately modeling cell behaviour.

The membrane is an electrolyte, and its primary function is to act as an ion conductor and electron insulator; hence, it is desirable to have a proton conductivity that is as high as possible. Since the conductivity of a membrane increases with the degree of hydration, keeping the membrane saturated is beneficial; however, membrane saturation needs to be balanced by water removal to prevent flooding, which leads to the idea of water management for PEM cells. One of the interesting modes of water transport in perfluorosulfonic membranes is via electro-osmotic drag. The flux of protons from the anode to the cathode effectively drags liquid water due to the interaction of electrostatic forces. This osmotic drag is quantified by, η_d, the electro-osmotic drag coefficient which is defined as the ratio of moles of water transported per mole of protons where there is no concentration or pressure gradient. Zawodzinski et al. have measured drag coefficients as high as 4.0 in fully hydrated samples of Membrane C, while Nafion 117 exhibited $\eta_d = 2.5$ for $\lambda = 22$, and $\eta_d = 0.9$ for $\lambda = 11$ [25].

As was stated in Section 4.2, in this thesis, it is assumed that the ionomer in cathode catalyst layer is completely hydrated. This is felt to be a valid assumption as this is where water is generated. Also, it is assumed that there is no variation in hydration across the layer; however, the degree of hydration in the anode catalyst layer is determined by the activity of water vapour adjacent to the electrode-catalyst layer interface. The activity of a species in an ideal gas mixture is determined by the ratio of the partial pressure of the species in the mixture to the pressure the pure species would have at the same temperature.

5.2 Assumptions

The following assumptions are made for the membrane model:

1. hydrogen and oxygen species are not present in the layer: conforms with the assumption that there is 100% Faradaic efficiency,
2. membrane hydration varies linearly from anode to cathode: a suitable first assumption although this may not be true for thicker membranes, and
3. the pressure difference between the anode and the cathode is a linear variation across the membrane: it is unknown what the actual pressure distribution in the membrane is, however, this is felt to be a suitable first assumption.

5.3 Mathematical Formulation

The mathematical formulation for the membrane is described by the conservation of species and energy. The net flux of water across the membrane is assumed to be the sum of osmotic-drag, diffusion, and convection due to a pressure gradient. The flux of protons is described by the Nernst-Planck equation. The index i is used to represent protons, $i = 2$, and liquid water, $i = 3$.

$$\text{Species:} \quad \nabla \cdot \vec{N_i} = 0 \tag{5.1}$$

$$\text{Energy:} \quad \nabla \cdot \vec{q} + \nabla \cdot \sum_{i=2}^{3} \vec{N_i} h_i W_i = 0. \tag{5.2}$$

For one dimensional transport only and applying these equations to the species in the membrane region gives,

$$\text{Current:} \quad \frac{dN_2}{dx} = 0 \tag{5.3}$$

$$\text{or,} \quad FN_2 = i_m = I \tag{5.4}$$

$$\text{Water Flux:} \quad \frac{dN_3}{dx} = 0 \tag{5.5}$$

$$\text{Energy:} \quad -k\frac{d^2T}{dx^2} + \frac{d}{dx}(N_3 h_3 W_3) = \frac{i_m^2}{\kappa} \tag{5.6}$$

where the relation $-\nabla \cdot (\vec{N}_2 h_2 W_2) = i_m^2/\kappa$ has been invoked in the energy equation.

The molar flux of water is given by

$$N_3 = -D_3\frac{dc_3}{dx} - \epsilon_w^{\text{mem}} c_3 \frac{k_p}{\mu}\frac{dp}{dx} + \frac{\eta_d I}{F} \tag{5.7}$$

where, the total molar water flux, N_3, is the result of a concentration gradient, a pressure gradient, and due to osmotic drag. The parameters k_p and μ are the hydraulic permeability of the membrane and fluid viscosity respectively, and ϵ_w^{mem} is the volume fraction of water in the membrane. Using assumption one, the gradient of membrane hydration is described by,

$$\frac{d\lambda}{dx} = \frac{\lambda_c - \lambda_a}{t_m} \tag{5.8}$$

where λ_c is the membrane hydration at the cathode catalyst layer and is set to correspond to full hydration, λ_a is the membrane hydration at the anode catalyst layer (determined by the vapour activity in the adjacent electrode), and t_m is the thickness of the membrane. In a similar fashion, from assumption three, the pressure gradient across the membrane is,

$$\frac{dp}{dx} = \frac{p_c - p_a}{t_m} \tag{5.9}$$

Substituting Equations (5.8) and (5.9) into (5.7) gives,

$$N_3 = -D_3 \left(\frac{c_{3c} - c_{3a}}{t_m} \right) - \epsilon_w^{mem} c_3 \frac{k_p}{\mu} \left(\frac{p_c - p_a}{t_m} \right) + \frac{\eta_d I}{F} \tag{5.10}$$

and hence N_3 is completely determined by boundary conditions for the layer where the electro-osmotic coefficient can be set by the mean membrane hydration as can the transport parameters.

The variation in membrane potential as a function of species flux is described by the Nernst-Planck equation written in terms of potential gradient:

$$\frac{d\Phi_m}{dx} = -\frac{i_m}{\kappa} - \frac{F}{\kappa} D_2 \frac{dc_2}{dx} + \frac{F}{\kappa} \frac{c_2}{c_3} N_3 \tag{5.11}$$

Unlike the formulation for the catalyst layers where the hydration is assumed to be uniform, the gradient of potential for the membrane region includes a term describing proton diffusion.

When a membrane absorbs water it expands. The concentration of charge sites, c_2, is therefore a function of hydration. Springer et al. measured the swelling exhibited by Nafion 117 membranes from a dry state to a fully hydrated condition [9]. They assume a linear dependence of swelling on hydration which modifies the concentration of charge sites from the dry state to a hydrated state in the form:

$$c_2 = \frac{\rho_m^{dry}}{W_m} \frac{1}{(1 + \delta\lambda)} \tag{5.12}$$

where c_2 is the concentration of charge sites in a hydrated state, ρ_m^{dry} is the density of the dry membrane, W_m is the equivalent weight of the membrane (grams per mole of charge sites), and δ is an experimentally determined coefficient. Springer et al. calculated δ to be 0.0126 for Nafion 117; it is assumed that this value applies to all membranes and is independent of temperature and pressure (this is not a particularly good assumption; however, no experimental data describing the expansion of other membranes was found in the literature). The concentration of water in the membrane, c_3, is then,

$$c_3 = \lambda \frac{\rho_m^{dry}}{W_m} \frac{1}{(1 + \delta\lambda)}. \tag{5.13}$$

Taking the derivative of Eqn (5.12) gives,

$$\frac{dc_2}{dx} = -\delta \frac{\rho_m^{dry}}{W_m} \frac{1}{(1+\delta\lambda)^2} \frac{d\lambda}{dx} \tag{5.14}$$

Substituting Eqns (5.12), (5.14), and (5.13) into Eqn (5.11) gives an equation describing the potential gradient in the membrane in terms of hydration, water flux, current, and temperature:

$$\begin{aligned} \frac{d\Phi_m}{dx} &= -\frac{i_m}{\kappa} + \delta \frac{RT}{F} \left(\frac{1}{1+\delta\lambda} \right) \frac{d\lambda}{dx} + \frac{F}{\kappa} \left(\frac{1}{\lambda} \right) N_3 & (5.15) \\ \text{where,} \qquad \lambda &= \lambda_a + \left(\frac{d\lambda}{dx} \right) (x - t_c). & (5.16) \end{aligned}$$

Eqn (4.26) was invoked to remove the coefficient of diffusion, and t_c is the position of the anode catalyst layer-membrane boundary (see Fig 1.1).

Finally, the energy equation can be written as

$$-k\frac{d^2T}{dx^2} + N_3 W_3 c_{p3} \frac{dT}{dx} = \frac{i_m^2}{\kappa}. \tag{5.17}$$

The correlations used to describe transport parameters for the membrane are discussed in Appendix A, Section 3.

5.4 Non-dimensionalization

The relevant equations describing the membrane are:

$$\text{Energy:} \quad -k\frac{d^2T}{dx^2} + \frac{d}{dx}(N_3 h_3 W_3) = \frac{i_m^2}{\kappa} \tag{5.18}$$

$$\text{Potential:} \quad \frac{d\Phi_m}{dx} = -\frac{i_m}{\kappa} + \delta\frac{RT}{F}\left(\frac{1}{1+\delta\lambda}\right)\frac{d\lambda}{dx} + \frac{F}{\kappa}\left(\frac{1}{\lambda}\right)N_3 \tag{5.19}$$

$$\text{Hydration:} \quad \lambda = \lambda_a + \left(\frac{d\lambda}{dx}\right)(x - t_c), \tag{5.20}$$

where the water flux, N_3, can be solved by Eqn (5.11) with the boundary conditions determined. This then leaves three equations with three unknowns. The equation for λ can be substituted into the energy and potential equations to reduce to two differential equations. Using the following non-dimensional variables:

$$x^* = \tfrac{x-t_c}{t_m}, \qquad T^* = \tfrac{T-T_c}{\Delta T}, \qquad \Phi_m^* = \tfrac{\Phi_m}{V_{oc}},$$

where t_m is the membrane thickness, results in non-dimensional parameters and equations describing the membrane region.

$$\bar{M}_1 = \frac{It_m}{V_{oc}\kappa} \tag{5.21}$$

$$\bar{M}_2 = \delta(\lambda_c - \lambda_a)\frac{RT_c}{FV_{oc}} \tag{5.22}$$

$$\bar{M}_3 = \frac{t_m N_3 F}{\kappa V_{oc}} \tag{5.23}$$

$$\bar{M}_4 = t_m N_3 W_3 \frac{c_{p3\ell}}{k} \tag{5.24}$$

$$\bar{M}_5 = \frac{I^2 t_m^2}{\kappa \Delta T k} \tag{5.25}$$

$$\bar{M}_6 = \lambda_a \tag{5.26}$$

$$\bar{M}_7 = \lambda_c - \lambda_a \tag{5.27}$$

$$\bar{M}_8 = \delta \tag{5.28}$$

$$\bar{M}_9 = \frac{\Delta T}{T_c} \tag{5.29}$$

The non-dimensional equations now become:

$$\text{Energy:} \quad \frac{d^2 T^*}{dx^{*2}} - \bar{M}_4 \frac{dT^*}{dx^*} + \bar{M}_5 = 0 \tag{5.30}$$

$$\text{Potential:} \quad \frac{d\Phi_m^*}{dx^*} - \bar{M}_2 \frac{(\bar{M}_9 T^* + 1)}{(\bar{M}_8 \lambda + 1)} - \frac{\bar{M}_3}{\lambda} + \bar{M}_1 = 0 \tag{5.31}$$

$$\text{Hydration:} \quad \lambda = \bar{M}_7 x^* + \bar{M}_6. \tag{5.32}$$

Chapter 6

Results and Discussion

6.1 Model Validation

6.1.1 Base Case Parameters

With a mathematical description of a PEM fuel cell developed, it is important to compare the model predictions to experimentally determined performance data. Some of the first researchers to use customized electrodes with supported catalysts were Ticianelli, Derouin and Srinivasan [21, 26]. They explored the effects of varying catalyst loading, and type, with a novel method of increasing interfacial contact at the reaction site; this work strongly influenced contemporary PEM fuel cell design. The experimental results of their work are well documented and, as such, are used to validate the present model.

Cell Temperature, T_c	353.0 K
Anode Pressure, p	3.0 atm
Cathode Pressure, p	5.0 atm
Anode Stoichiometry, ζ	1.5
Cathode Stoichiometry, ζ	3.0
Anode Relative Humidity	100%
Cathode Relative Humidity	100%
Electrode Thickness, t_e	180 μm
Catalyst Layer Thickness, t_{cl}	10 μm
Membrane Thickness, t_m	180 μm
Volume Fraction Membrane in Catalyst Layer, $\epsilon_{\mathrm{m}}^{\mathrm{cl}}$	0.17
Volume Fraction Solid in Catalyst Layer, $\epsilon_{\mathrm{s}}^{\mathrm{cl}}$	0.4
Anode Flooding	98%
Cathode Flooding	98%
Anode Dry Gas Mole Fraction $\frac{CO_2}{H_2}$, x_{12}	0.0 (pure H_2)
Cathode Dry Gas Mole Fraction $\frac{N_2}{O_2}$, x_{12}	3.76 (Air = 3.76)
Reversible Potential, V_{oc}	1.199 V
Reactive Area per Unit Volume, a	68×10^3 cm^2/cm^3
Anode Catalyst Layer H_2 Permeability, $D_1^{\mathrm{eff}} c_1^{\mathrm{ref}}$	2×10^{-8} mol/cm-s-atm
Cathode Catalyst Layer O_2 Permeability, $D_1^{\mathrm{eff}} c_1^{\mathrm{ref}}$	7×10^{-10} mol/cm-s-atm
Anode $a \times i_0^{\mathrm{ref}}$	4000 A/cm^3
Cathode $a \times i_0^{\mathrm{ref}}$	0.0013 A/cm^3
$\frac{Sh \times f_e}{L}$	20000 cm^{-2}
Vapour Flux at Interface B, (Boundary Condition B2)	0.1
Vapour Flux at Interface E, (Boundary Condition E2)	-0.1

Table 6.1: Validation Parameters

The primary goal of the model developed here is to accurately predict the overall cell polarization that results from a given set of operating conditions and physical parameters. Using the parameters listed in Table 6.1, the predicted polarization curve for 20 wt% Pt/C catalyst is compared to the experimental data of Ticianelli et al. in Figure 6.1.

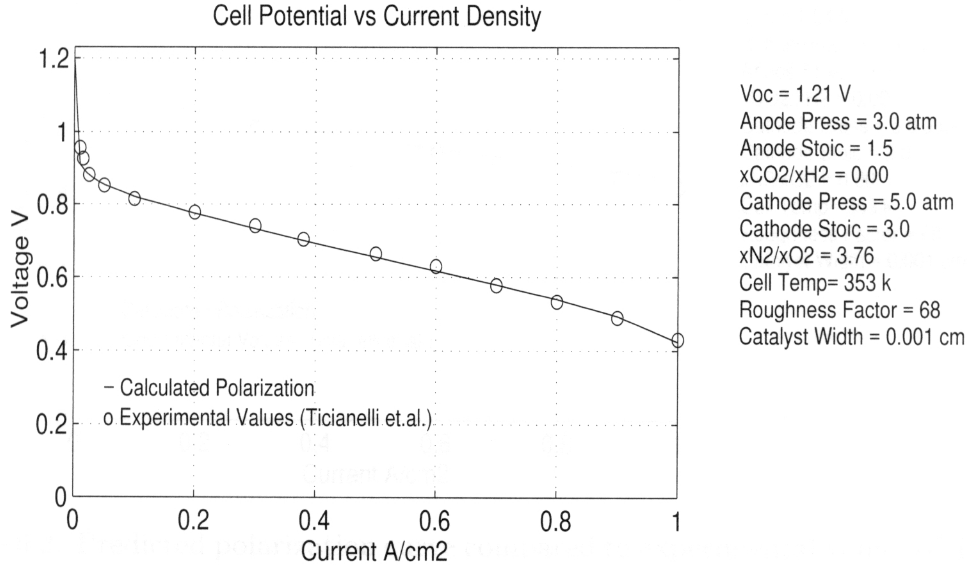

Figure 6.1: Predicted polarization curve compared to experimental values of Ticianelli et al. for 20 wt% Pt/C catalyst and 5 atm air [21].

As can be seen, the model results compare well with the experimental values. Figure 6.2 compares the predicted model results for pure oxygen with the same paramters. Again, good agreement is evident between the present model's predictions and experimental data.

It is important to note that no adjustment to the reactive surface area, a, or the exchange current density, i_0^{ref}, is required. The roughness factor employed (surface area of catalyst per unit area of cell) is the average of the two values reported by Ticianelli for 20 wt% Pt/C catalyst determined by cyclic voltammetry and transmission electron microscopy [26]. The electrode thickness is lower than many values used in

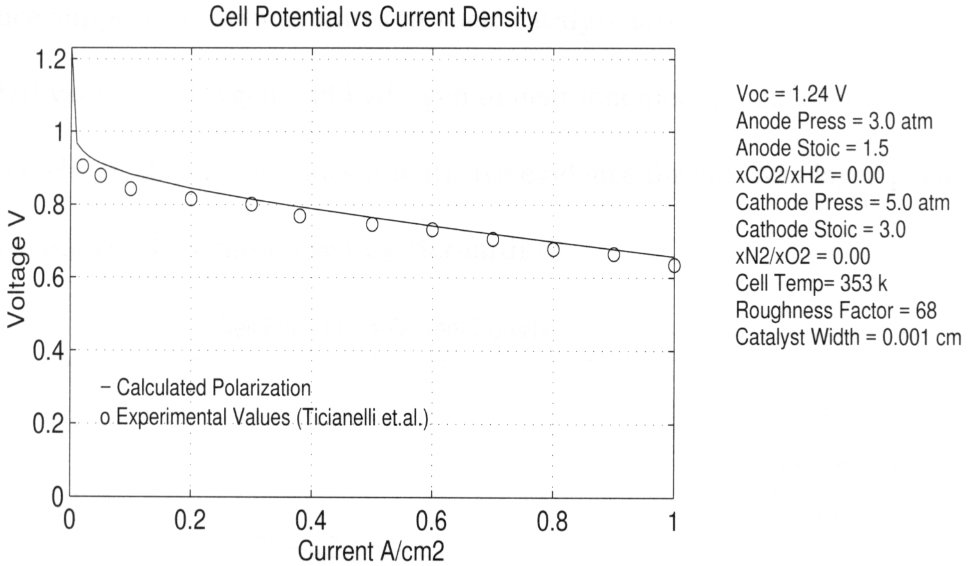

Figure 6.2: Predicted polarization curve compared to experimental values of Ticianelli et al. for 20 wt% Pt/C catalyst and 5 atm O_2 [21].

other models; a value of 260 to 300 μm is often used, which corresponds to the width of electrode material as received. Springer et al. report a compressed value for E-Tek electrodes of approximately 180 μm [22]; Ticianelli's group used Prototech electrodes. It is assumed here that there is negligible difference between the physical properties of the two types of electrodes.

The composition of the catalyst layer requires some justification. The values for volume fraction of membrane and solid are similar to those used by Weisbrod et al. [16] but are significantly different from those of Bernardi et al. [6, 7]. As is discussed later, the permeability of the catlayst layer has a significant impact on catalyst utilization and overall cell polarization. Work at Los Alamos National Laboratory provides evidence supporting permeabilites in their catalyst layer, that are much higher than reported values for oxygen and hydrogen in neat ionomer [12, 22]. Moreover, the work of Ticianelli et al. [21], provides qualitative evidence for catalyst layer permeabilities that are higher than those used by Bernardi [7].

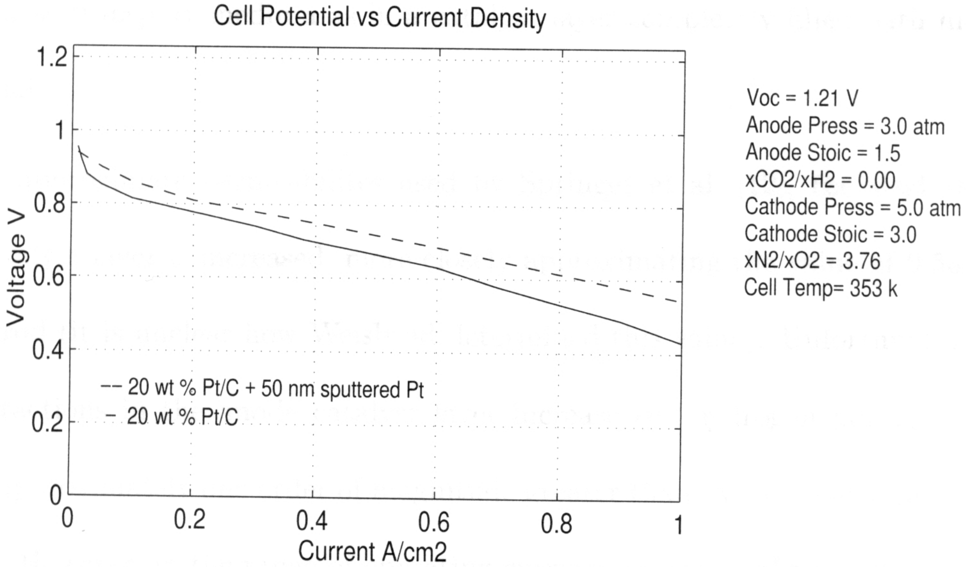

Figure 6.3: Experimental polarization curves of Ticianelli et al. for 20 wt% Pt/C catalyst and 20 wt% Pt/C catalyst with a 50 nm sputter-deposited Pt film [21].

Figure 6.3 highlights the benefit of depositing an additional 0.05 mg/cm^2 of platinum on an electrode loaded with 0.35 mg/cm^2 supported catalyst [21]. As shown by Bernardi and Verbrugge using catalyst layer permeabilties similar to those in neat ionomer [6, 7], at operating current densitites higher than 100 mA/cm^2 less than 2% of the cathode catalyst layer is utilized. In this case, the reaction is confined to the interface between the electrode and the catalyst layer. If this were the case, then the effect of adding a thin layer of catalyst at the opposite interface would only be evident at extremely low current densities. It is clear in Figure 6.3 that the benefits of an additional surface layer of catalyst are exhibited across the entire current range. This suggests higher permeabilites than those expected if diffusion through ionomer is the only mass transport medium as in a catalyst layer completely filled with membrane material.

To approximate permeabilites used by Springer et al. [12], the void volume of the catalyst layer is increased, more closely approximating the value of 0.53 used by Weisbrod (it is unclear how Weisbrod determined this value). Unfortunately, higher void fractions in the anode catalyst layer increase the hydrogen permeability to a value approximately one order of magnitude greater than oxygen which may be unrealistic. However, in the range of operating currents explored, the anode contribution to cell polarization is very small; thus, the effect of increased anode permeability has minimal effect on overall polarization. At this time, research is being performed by many people to determine catalyst layer morphology and transport properties more precisely.

6.1.2 Electrode Parameters

It was found by Springer et al. the effect of ribbed channels in the gas distribution plate causes an increase in the local gas flux and a resultant decrease in reactant concentration in the electrode [22]. To simulate the effects of the ribs on gas flux with a uniform, one-dimensional flow field (no ribs), they found that increasing the real electrode width by a factor of 1.6 produced the same concentration decrease at the catalyst layer [22]. Due to the nature of the model developed here, the actual electrode width is required to determine the temperature profile. Springer et al. also determine a tortuosity factor describing diffusion in the electrode which is used to calculate the effective diffusivity. They report a tortuosity factor of 7.0. Adjusting the tortuosity factor to 10.0 and setting the electrode thickness at 200 μm also gives a reasonable fit to Ticianelli's data and still provides a realistic dimension for the electrode thickness. With these values the model fit to experimental values is shown in Figures 6.4 and 6.5.

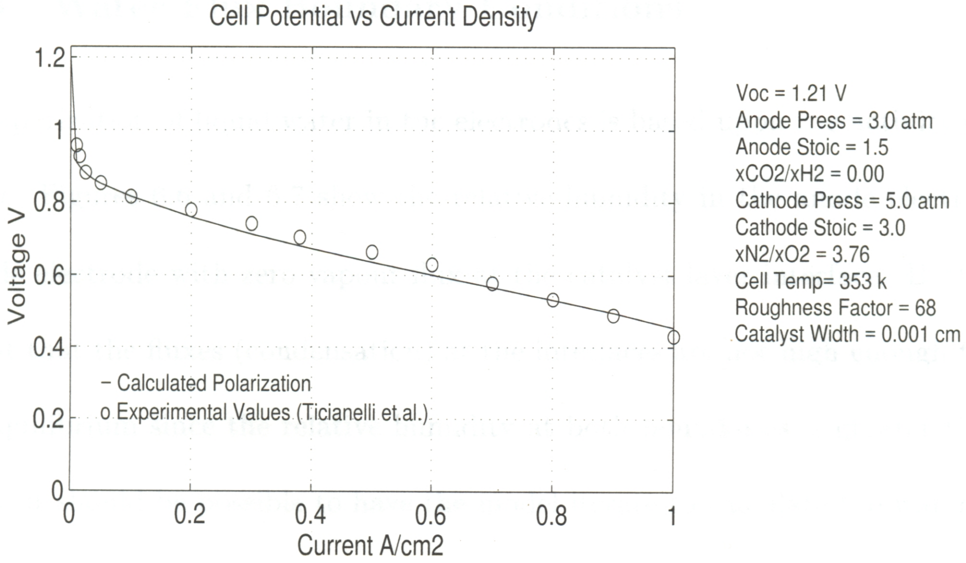

Figure 6.4: Predicted polarization curve compared to experimental values of Ticianelli et al. [12], for 20 wt% Pt/C catalyst and 5 atm air with modified tortuosity.

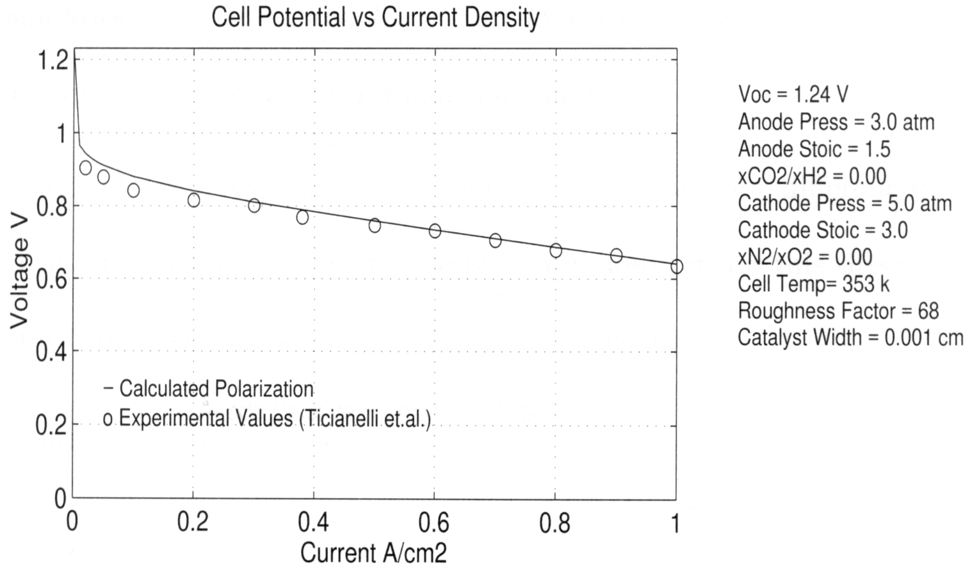

Figure 6.5: Predicted polarization curve compared to experimental values of Ticianelli et al. [12], for 20 wt% Pt/C catalyst and 5 atm O_2 with modified tortuosity.

6.1.3 Water Flux Boundary Conditions

The vaporization of liquid water in the electrodes is based upon the activity of water vapour. Figures 6.6 and 6.7 show the relative humidity in the anode electrode and cathode electrode with zero vapour flux at the catalyst layer interface. Both figures suggest that the fluxes (condensation) at the interfaces are not high enough to maintain equilibrium since the relative humidity at both boundaries is greater than 100. Ideally, it should be possible to have the model iterate to calculate the water vapour flux at the catalyst layer interfaces; however, at this time, these boundary conditions need to be set for a given simulation. Adjusting the non-dimensional water flux at the boundaries to $B2 = 0.1$ and $E2 = -0.1$ moves the mole fraction of water vapour closer to equilibrium as shown in Figures 6.8 and 6.9.

The flux of water vapour at the boundaries will vary for different levels of gas humidification, current density and temperature; however, for this thesis an absolute value of 0.1 for both fluxes is set as the base case condition.

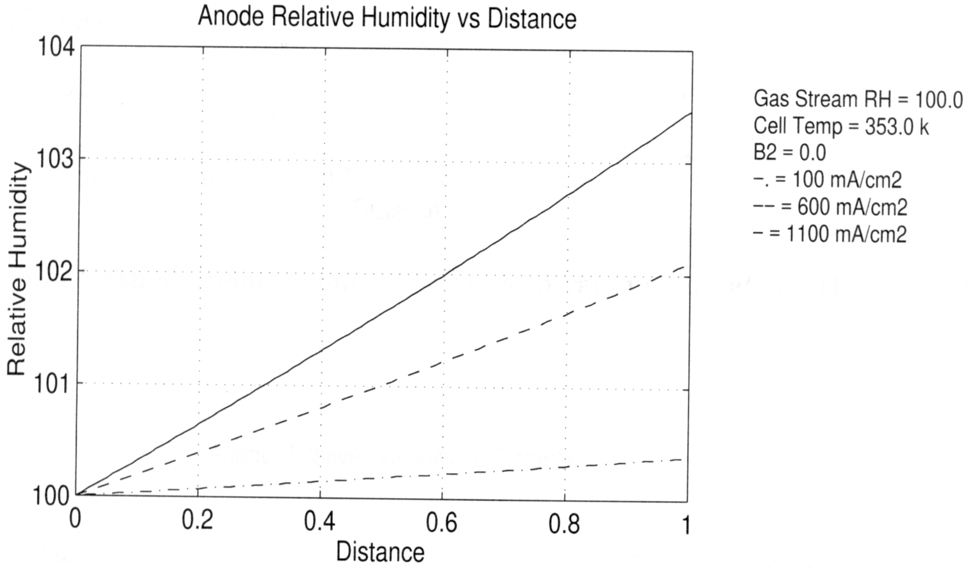

Figure 6.6: Anode relative humidity for zero vapour flux at interface b (B2 = 0.0).

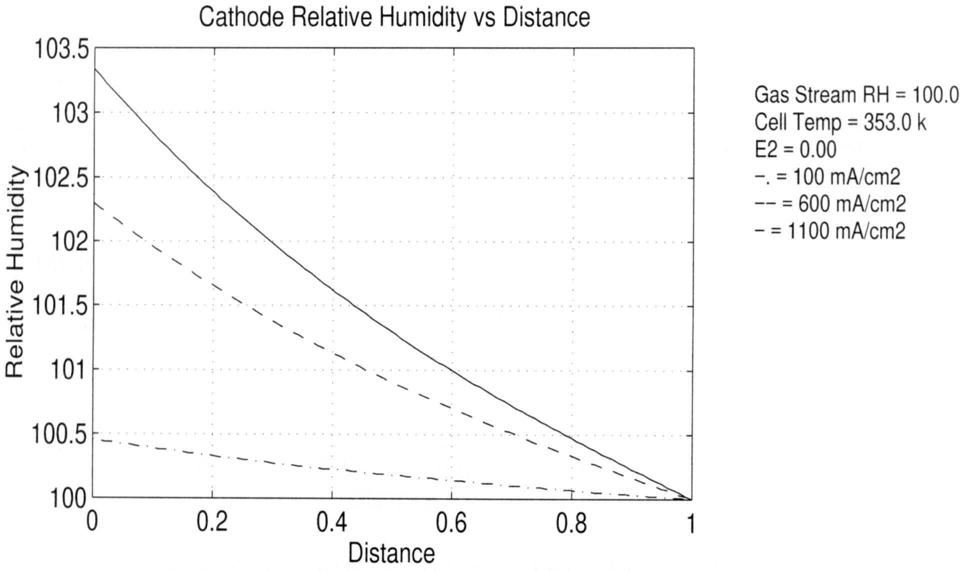

Figure 6.7: Cathode relative humidity for zero vapour flux at interface e (E2 = 0.0).

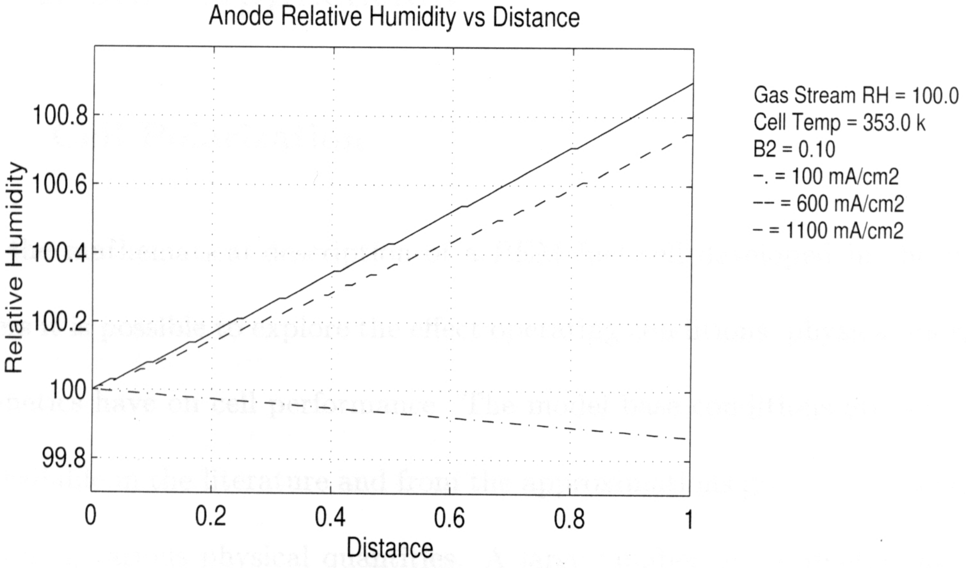

Figure 6.8: Anode relative humidity for B2 = 0.1.

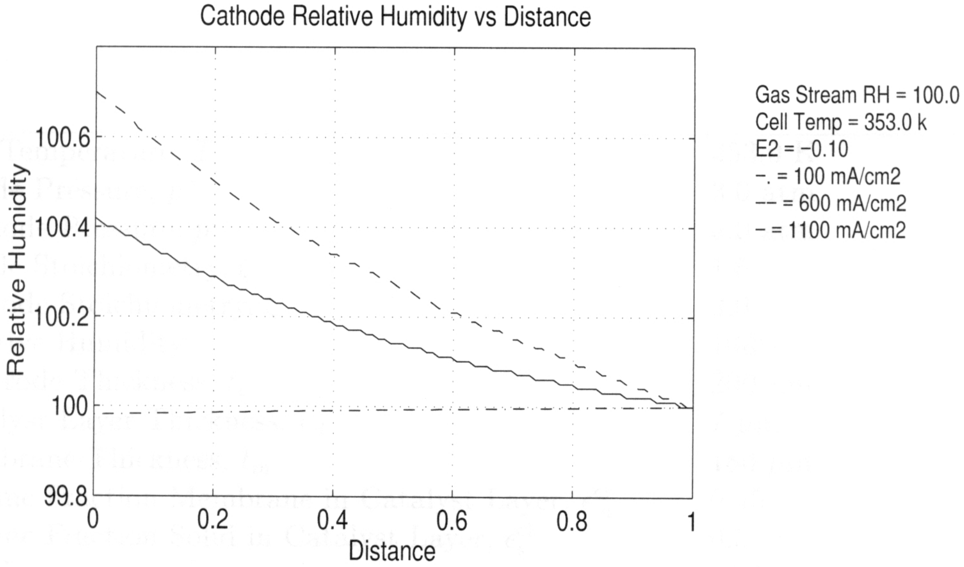

Figure 6.9: Cathode relative humidity for E2 = -0.1.

6.2 Model Application

6.2.1 Cell Polarization

Using the mathematical description of a PEM fuel cell developed in the preceding chapters it is possible to explore the effect operating conditions, physical morphology, and kinetics have on cell performance. The model base conditions are derived from data available in the literature and from the approximations given in Appendix A for determining various physical quantities. A large number of parameters are used in the model, consequently providing the opportunity to explore many areas.

Cell Temperature, T_c	353.0 K
Anode Pressure, p	3.0 atm
Cathode Pressure, p	3.0 atm
Anode Stoichiometry, ζ	1.5
Cathode Stoichiometry, ζ	3.0
Relative Humidity	100%
Electrode Thickness, t_e	200 μm
Catalyst Layer Thickness, t_{cl}	7 μm
Membrane Thickness, t_m	180 μm
Volume Fraction Membrane in Catalyst Layer, $\epsilon_{\mathrm{m}}^{\mathrm{cl}}$	0.45
Volume Fraction Solid in Catalyst Layer, $\epsilon_{\mathrm{s}}^{\mathrm{cl}}$	0.5
Flooding	98%
Anode Dry Gas Mole Fraction $\frac{CO_2}{H_2}$, x_{12}	0.0 (pure H_2)
Cathode Dry Gas Mole Fraction $\frac{N_2}{O_2}$, x_{12} (Air = 3.76)	3.76
Reversible Potential, V_{oc}	1.199 V
Reactive Area per Unit Volume, a	5×10^5 cm^2/cm^3
Anode Catalyst Layer H_2 Permeability, $D_1^{\mathrm{eff}} c_1^{\mathrm{ref}}$	2.6×10^{-10} mol/cm-s-atm
Cathode Catalyst Layer O_2 Permeability, $D_1^{\mathrm{eff}} c_1^{\mathrm{ref}}$	2.4×10^{-11} mol/cm-s-atm
Anode $a \times i_0^{\mathrm{ref}}$	30000A/cm^3
Cathode $a \times i_0^{\mathrm{ref}}$	0.0095A/cm^3
Anode Electrode Thermal Conductivity, k^{eff}	0.016 W/cm-k
Anode Catalyst Layer Thermal Conductivity, k^{eff}	0.015 W/cm-k
Membrane Thermal Conductivity, k^{eff}	0.0034 W/cm-k
Cathode Catalyst Layer Thermal Conductivity, k^{eff}	0.015 W/cm-k
Cathode Electrode Thermal Conductivity, k^{eff}	0.016 W/cm-k
$\frac{Sh \times f_e}{L}$	20000 cm^{-2}
Sherwood Number, Sh	2.0
Surface Area Water per unit Vol, f_e	200 cm^2/cm^3
Reference Length Scale, L	0.020 cm
Vapour Flux at Interface B, (Boundary Condition B2)	0.1
Vapour Flux at Interface E, (Boundary Condition E2)	-0.1

Table 6.2: Base Case Model Parameters

The base conditions for this section are given in Table 6.2. The most significant difference between the parameters set here and those in Section 6.1 is for the volume composition of the catalyst layers. Here, the void fraction was set at 5% as the values used by Weisbrod have not been substantiated in the literature for hot-pressed MEA assemblies. It was decided to use values similar to Bernardi to provide what is expected to be a more realistic value for the thermal conductivity of the layer. Furthermore, because thermal effects are more pronounced at higher currents an electrode tortuosity of 7.0 is used, thereby allowing current densities greater than 1.0 A/cm^2 to be explored.

The cell polarization curve resulting from the base case parameters is shown in Figure 6.10. As expected, the most significant contributor to potential loss for the

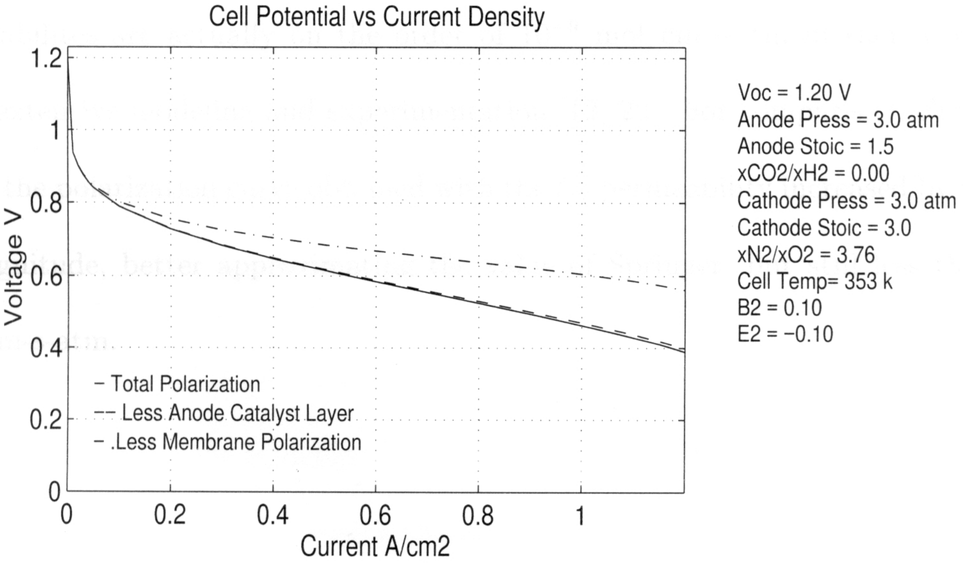

Figure 6.10: Base case polarization curve.

cell is the cathode layer. A low permeability and exchange current density combine to demand a significant portion of the reaction free energy. The membrane layer also shows a large potential loss due to low ion conductivity. The anode catalyst layer loss is insignificant due to the relatively high permeability of H_2 in the layer as compared to that for O_2 and, more importantly, because the anode reaction is orders of magnitude faster than the cathode for a given activation overpotential.

6.2.2 Catalyst Layer Permeability

The permeabilites used for the base case are calculated as described in Appendix A and are higher than the experimental values given by Broka and Ekdunge [27] for reactant gases in neat Nafion 1100; however, Springer et al. argue that oxygen permeabilites are actually on the order of 10^{-9} mol/cm-s-atm in their cells based upon extensive modeling and experimentation [12, 22]. For comparison, Figure 6.11 shows the polarization curve obtained with the O_2 permeability increased by an order of magnitude, better approximating the value of Springer, but still less than 10^{-9} mol/cm-s-atm.

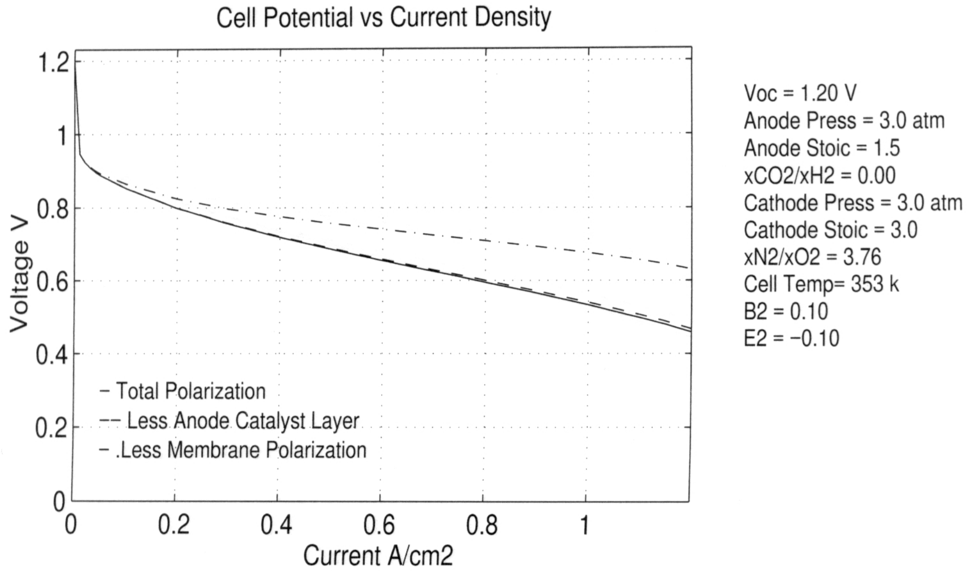

Figure 6.11: Polarization curve for high O_2 permeability (2×10^{-10} mol/cm-s-atm.)

The polarization curve resulting from a decrease in the permeability of H_2 by an order of magnitude is shown in Figure 6.12. The anode potential loss is clearly greater with a lower permeability.

6.2.3 Catalyst Surface Area

The morphology and physical composition of the catalyst layer has a significant impact on cell polarization and a substantial amount of research is being conducted in hopes of optimizing the structure [21, 26, 28, 29, 30]. Essentially, the two main areas being addressed are (1) decreasing the amount of precious metal catalyst while ensuring a large reactive surface area, and (2) increasing gas permeability in the layer.

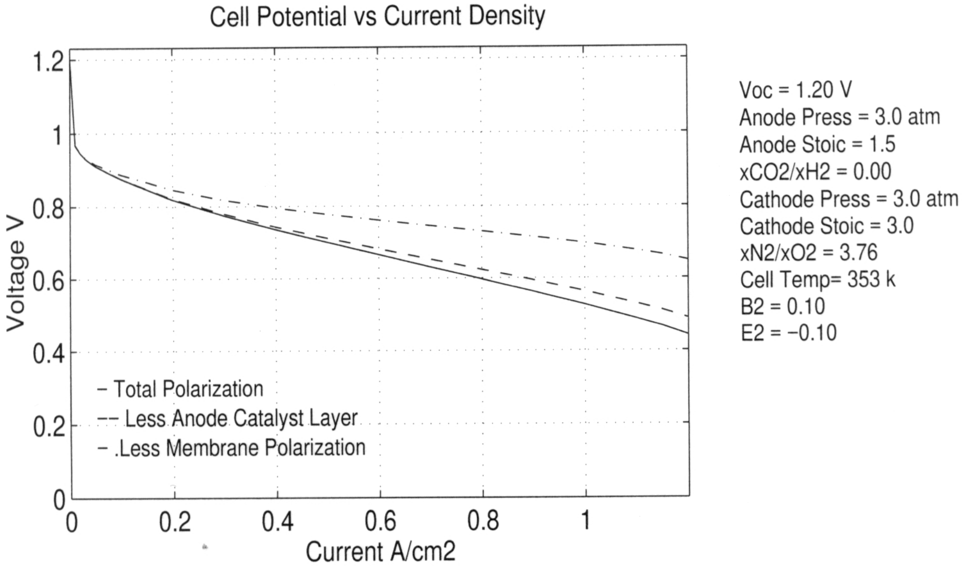

Figure 6.12: Polarization curve for low H_2 permeability (3×10^{-11} mol/cm-s-atm).

The second point is being approached in a number of different ways, such as, wet-proofing, void space inclusion, catalyst composition, and using ionomers with higher gas solubility. One way of decreasing the activation polarization for a given current density is by increasing the reactive surace area. Values for the active area per unit volume depend on catalyst loading, layer thickness, and catalyst morphology. Values used in the literature can vary from 10^4 cm^{-1} to 10^8 cm^{-1} [26, 13] depending on catalyst type and layer morphology. The effect of increasing the active surface area per unit volume in the cathode catalyst layer from 5×10^5 to 1×10^6 cm^{-1} is shown in Figure 6.13. A decrease in polarization across the entire current range is evident.

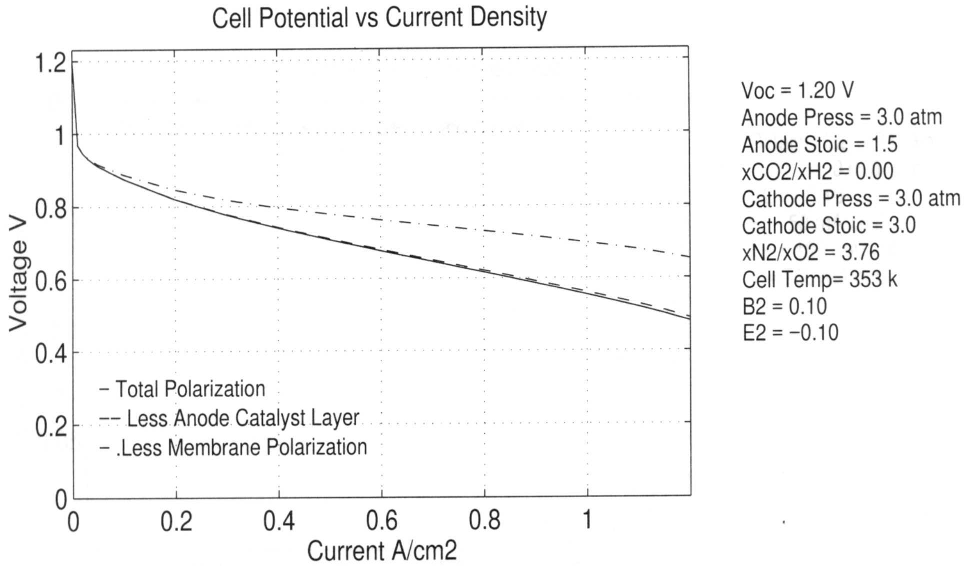

Figure 6.13: Cell Polarization with cathode active surface area at 1×10^6 $\mathrm{cm}^2/\mathrm{cm}^3$.

6.2.4 Catalyst Utilization

The effect of increased permeability in the cathode catalyst layer on catalyst utilization is clearly shown in Figures 6.14 and 6.15. The low permeability results support the conclusions of Bernardi and Verbrugge [7] that the cathode reaction is essentially a surface reaction at normal fuel cell operating conditions. The high permeability conditions in Figure 6.15 show better catalyst utilization; however, as the current density increases, the effective reaction thickness once again becomes a very thin layer near the electrode-catalyst layer surface.

In view of Ticianelli's experimental data that shows the positive effect of a sputtered layer of catalyst on the electrode surface, and the model predictions for the

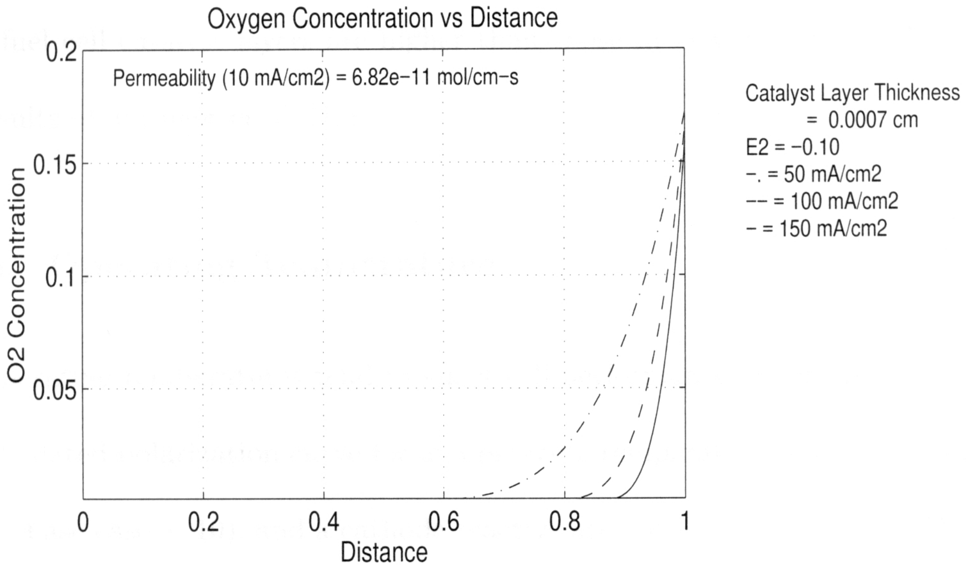

Figure 6.14: Cathode catalyst layer utilization for low O_2 permeabilities.

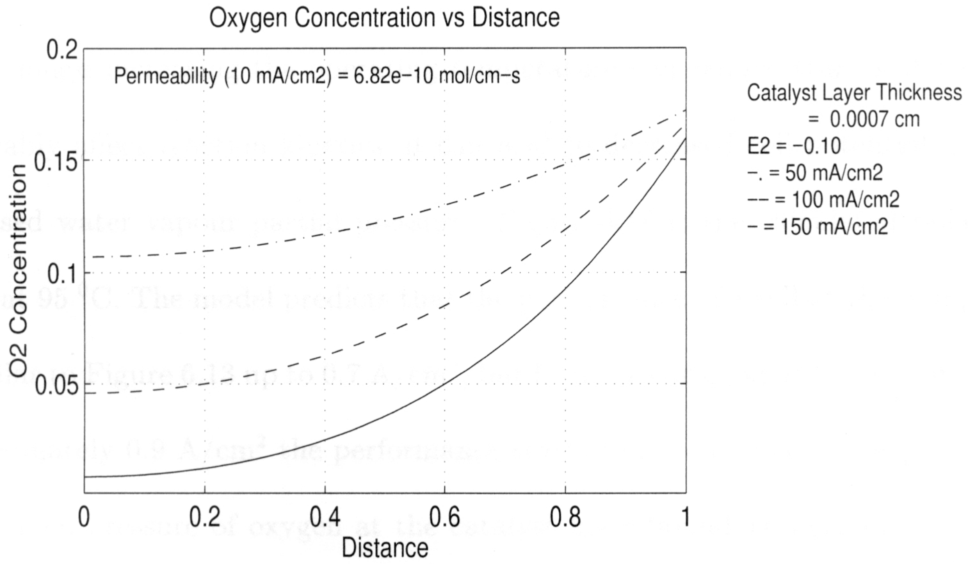

Figure 6.15: Cathode catalyst layer utilization for high O_2 permeabilities.

utilization of catalyst, this model suggests that the permeabilities of contemporary PEM fuel cell catalyst layers are higher than those in neat ionomer. This confirms the results of Springer et al. [12].

6.2.5 Operating Temperature

Low operating temperatures tend to affect cell performance adversely. Figure 6.16 is the calculated polarization curve for an operating temperature of 60 ^{0}C, high permeability (base case $\times$ 10), and a cathode reactive area of 1×10^6 cm^2/cm^3. Comparing this curve with Figure 6.13 which is calculated for similar conditions except for a cell temperature of 80 ^{0}C, a noticeable decrease in potential is evident primarily due to increased resistive losses in the membrane.

Although increasing the operating temperature can reduce transport losses and favourably affect reaction kinetics, it can lead to decreased cell potential due to an increased water vapour partial pressure. Figure 6.17 is the calculated polarization curve at 95 ^{0}C. The model predicts that the performance of a cell at this temperature is similar to Figure 6.13 up to 0.7 A/cm^2, but begins to drop off at higher currents. At approximately 0.9 A/cm^2 the performance starts to become mass-transport limited. The partial pressure of oxygen at the catalyst layer boundary becomes so low that a limiting current density will be reached at about 1.0 A/cm^2. When the reactant concentration in the catalyst layer approaches zero, the numerical algorithm becomes

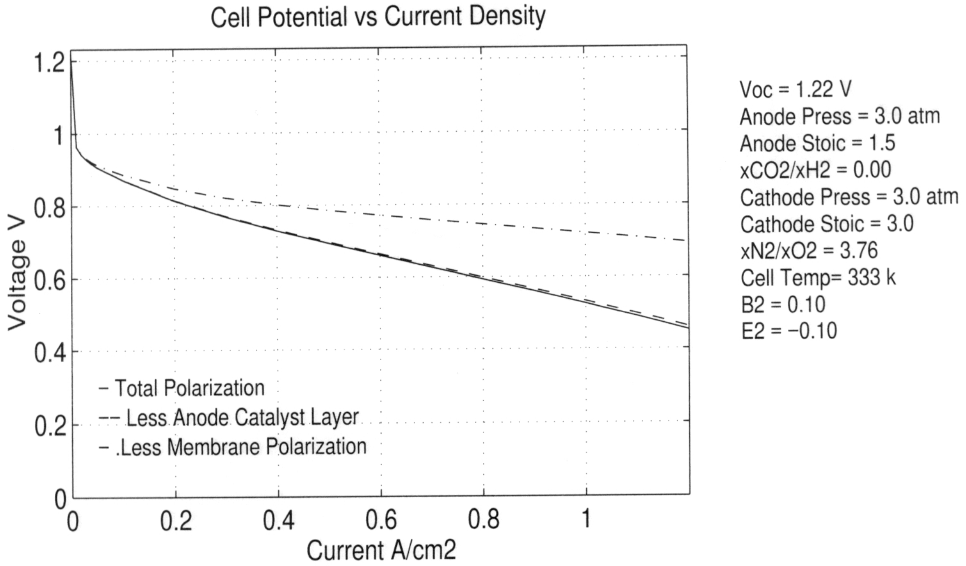

Figure 6.16: Cell polarization curve with high permeability, $a = 1 \times 10^6$ cm^{-1} and $T_c = 333$ K.

very unstable; hence, the lack of data after 0.89 A/cm^2. However, one can predict the limiting current is approximately 1.0 A/cm^2 by observing the plot of oxygen mole fraction versus position in the cathode electrode as shown in Figure in O_2 mole fraction. At 0.8 A/cm^2 the oxygen mole fraction at the catalyst layer is approximately 0.03. As can be seen, the oxygen partial pressure at the catalyst layer is approximately a linear function of current density. Extrapolating the mole fraction at the interface for an operating current of 1.0 A/cm^2 predicts a mole fraction of nearly zero; thus, the reaction will be mass-transport limited.

The results described above imply that given sufficient information concerning the physical characteristics of a cell and water vaporization in the electrodes, an optimum

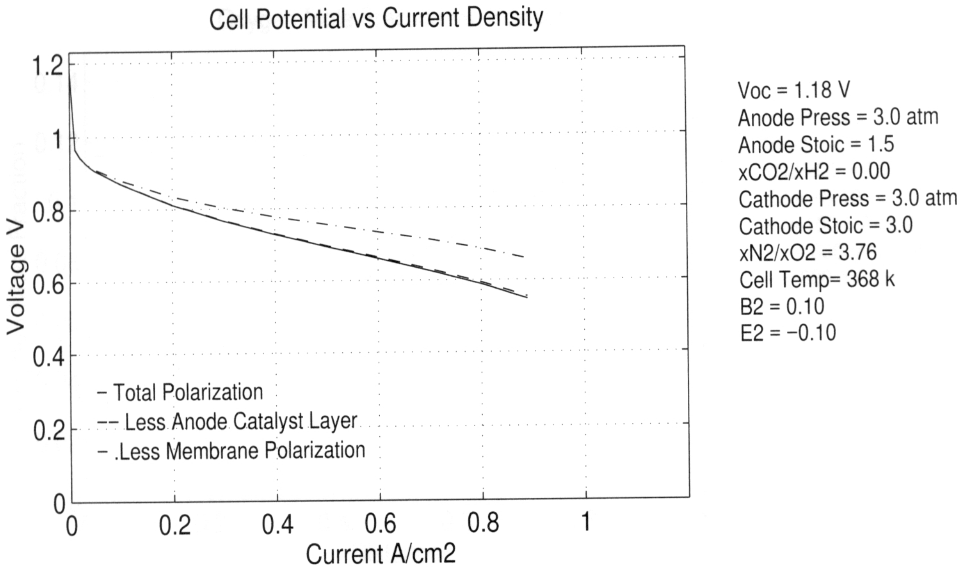

Figure 6.17: Cell polarization curve with high permeability, $a = 1 \times 10^6$ cm^{-1} and $T_c = 368$ K.

operating temperature can be found.

6.2.6 Thermal Effects

The calculated temperature profile across the complete width of a PEM cell with $B2 = 0.0$ and $E2 = 0.0$ is shown in Figure 6.19. The temperature is non-dimensionalized by an arbitrary value which is listed as ΔT in the legend by the plot. For all temperature plots in this thesis ΔT has been set as 4 K; thus, a non-dimensional temperature of 0.25 is equivalent to 1 K.

Figure 6.19 shows that at low current densities the temperature across the cell is nearly uniform. As the operating current increases, the temperature profile rises in

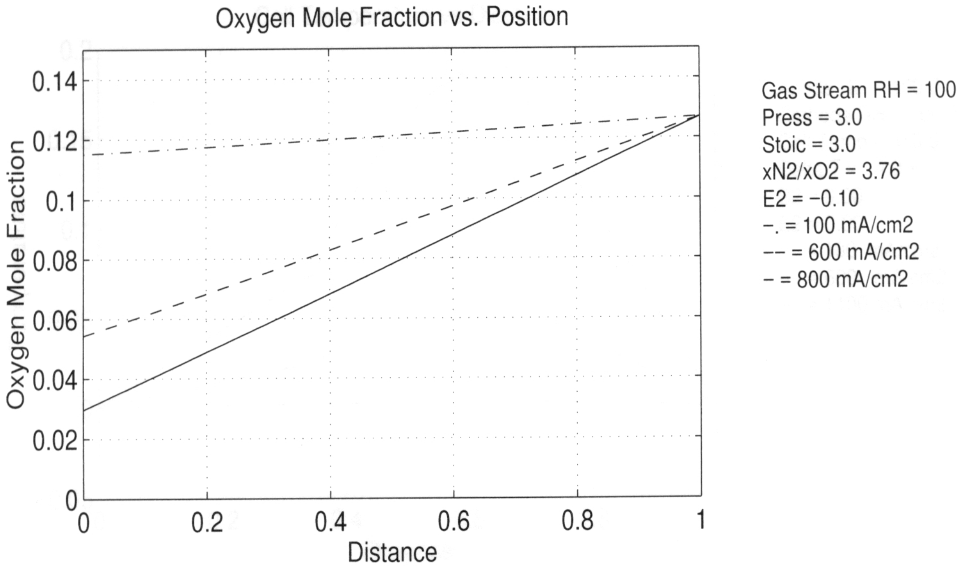

Figure 6.18: Cathode electrode mole fraction O_2 at $T_c = 368$ K.

a non-linear fashion suggesting that as designers try to increase the performance of PEM cells the more critical heat management issues will become. Besides the design issues associated with heat removal in fuel cell stacks, the temperature profile is of interest for other reasons. Vaporization in the electrodes is affected by heat transfer and is of special interest since membrane hydration is a critical parameter governing performance [31]. Currently, the most common means of maintaining membrane hydration is by gas stream humidification [11, 10, 5, 31]. Further, the temperature of the cell affects the transport properties and the reaction rate constants according to the Arrehnius definition. While a low operating temperature gives a higher theoretical open circuit potential, it also leads to lower reaction rates, higher resistivities, lower diffusivities and lower solubilities - seemingly due to decreased water absorption in

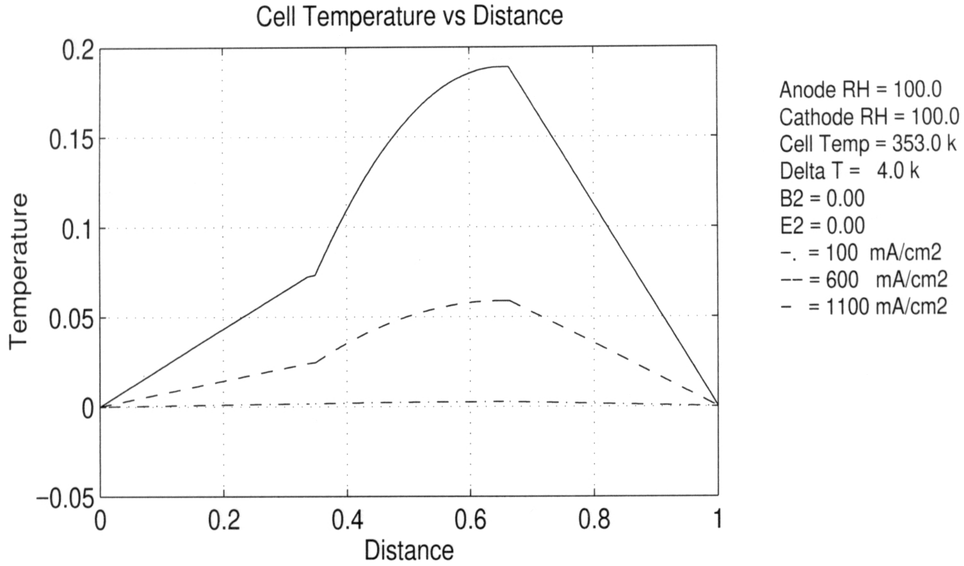

Figure 6.19: Cell temperature profile with zero vapour flux at interfaces a and b.

the membrane at lower temperatures [19]. These conditions adversely affect cell performance. On the other hand, a lower cell temperature results in a lower water vapour pressure. As will be seen, the mole fraction of reactant in the cathode gas stream is one of the important factors limiting maximum cell operating currents; thus, decreasing the vapour pressure of water in the gas streams while maintaining membrane hydration can be beneficial.

6.2.7 Water Phase Change

Figure 6.20 is a plot of the temperature profile across a cell with base case flux conditions. The peak temperature difference at 1100 mA/cm^2 is slightly less than 0.8 Kelvin. The heat produced in the cell is due to the exothermic nature of the overall

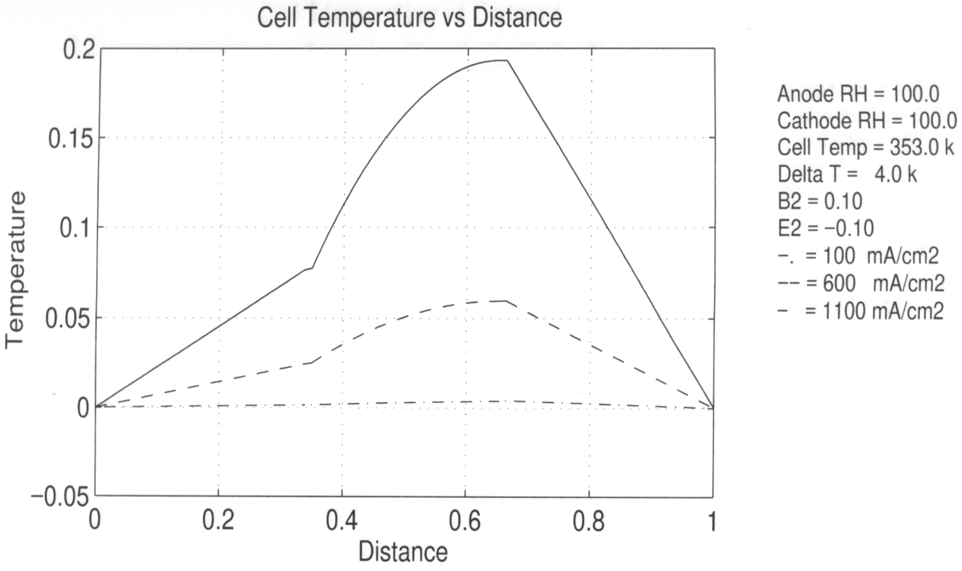

Figure 6.20: Cell temperature profile for base case vapour flux.

reaction, Joule heating and the phase change of water. In this case, the heat contribution from the condensation of water vapour is small because the relative humidity of the gas streams is set at 100%. In some working cells the gas streams are introduced into the cell at temperatures higher than the operating point so as to provide a larger quantitity of water vapour. Such a situation leads to water condensation and would release heat in the electrodes, driving the temperature up. Figure 6.21 shows the temperature profile where the base case vapour fluxes at the catalyst layer interfaces are used and the gas channel humidity is set at 110% (simulating saturated, higher temperature feed streams). The effect of higher condensation at the interfaces and in the electrodes is most prominent at the lower operating current where the peak temperature across the cell is seen to be approximately twice as high as in Figure

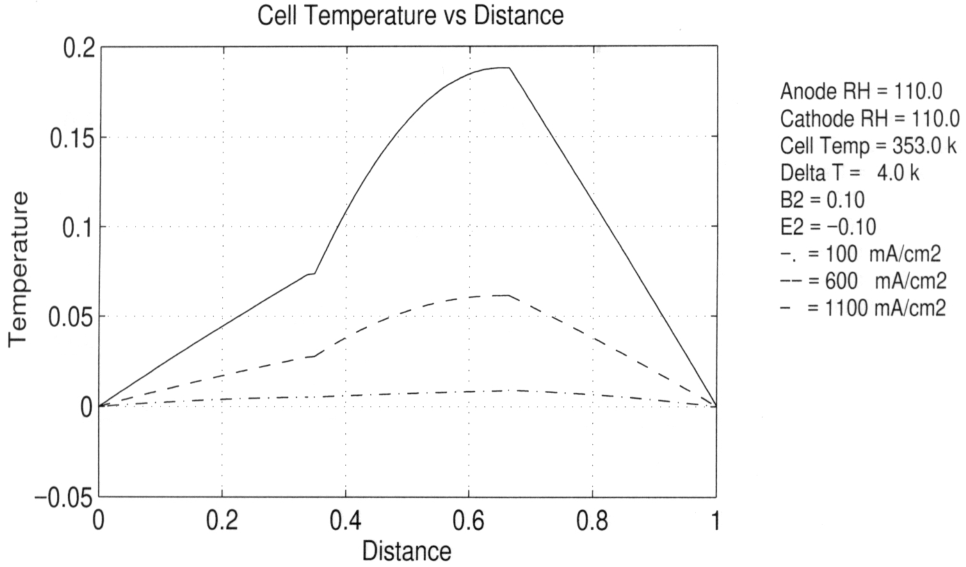

Figure 6.21: Cell temperature profile for base case boundary fluxes and gas feed stream humidities of 110%.

6.20 (in fact, a slight decrease in peak temperature is seen at 1.1 A/cm^2 which can be explained by reduced membrane resistivity due to better hydration). This can be explained by the fact that at lower currents the Joule heating and heat of reaction will be small and thus the heat of vaporization will be a larger portion of the total heat released. If Joule heating were linearly dependent on current one might expect the resistive heat contribution to be similar at all operating currents (since the boundary fluxes are non-dimensionalized by the reactant gas flux); however, as we know, resistive heat dissipation is proportional to the square of the current density. Thus, as current increases Joule heating becomes a larger portion of the total heat production.

The effect of water vaporization can be simulated by setting the relative humidity

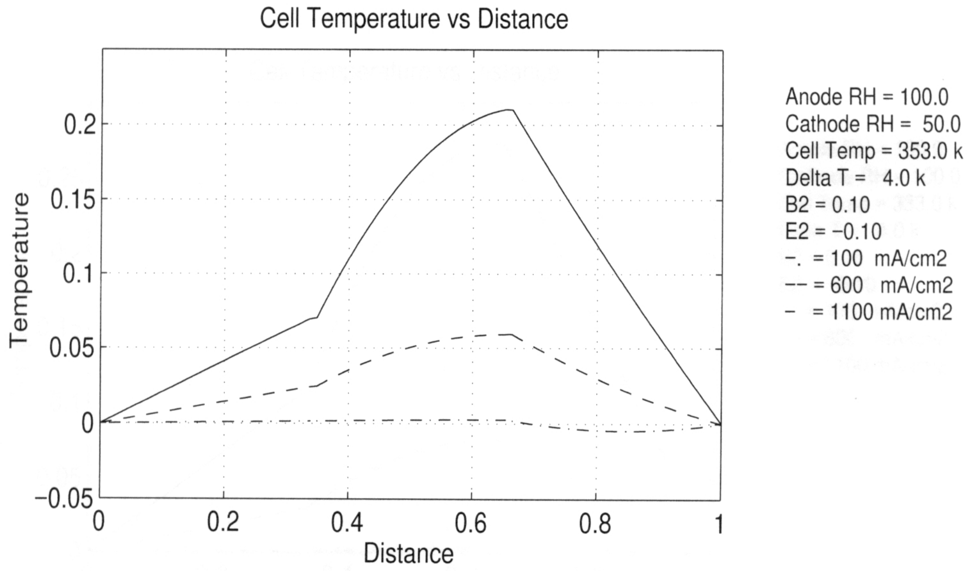

Figure 6.22: Cell temperature profile for base case boundary fluxes and cathode gas stream humidity of 50%.

in the cathode gas stream to 50%. In Figure 6.22, the effect of liquid evaporization is clearly evident at 100 mA/cm^2 driving the temperature down. This can be seen at the higher operating currents, as well, by the slight depression in the temperature profile across the cathode section.

6.2.8 Cell Operating Temperature

The temperature profiles through a cell for an operating temperature of 60 ^{0}C and 95 ^{0}C are shown in Figures 6.23 and 6.24. The peak temperatures at 60 ^{0}C are higher than those shown in Figure 6.20, and, at 600 mA/cm^2, it appears that the peak temperature at 95 ^{0}C is less than the peak at a cell temperature of 80 ^{0}C. Although

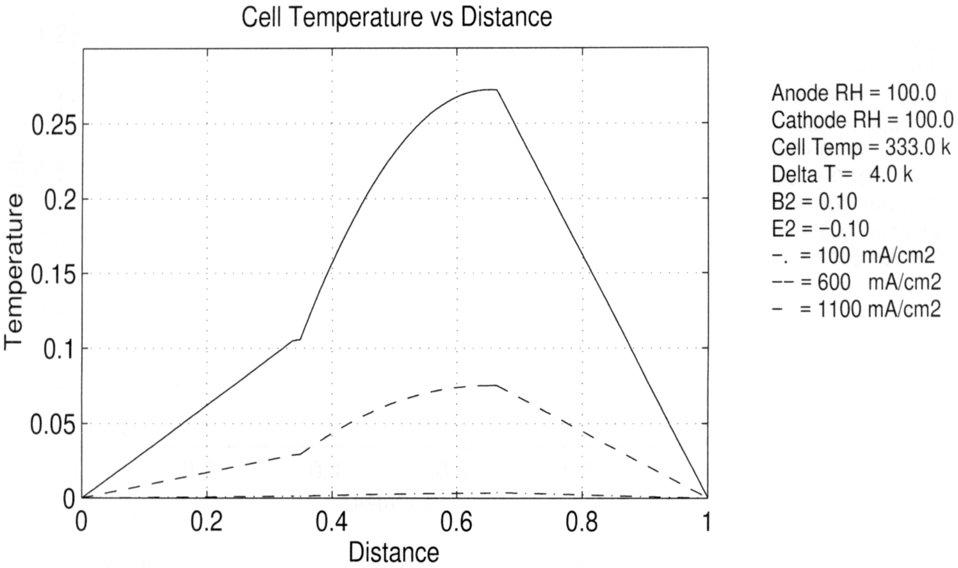

Figure 6.23: Cell temperature profile at $T_c = 333$ K.

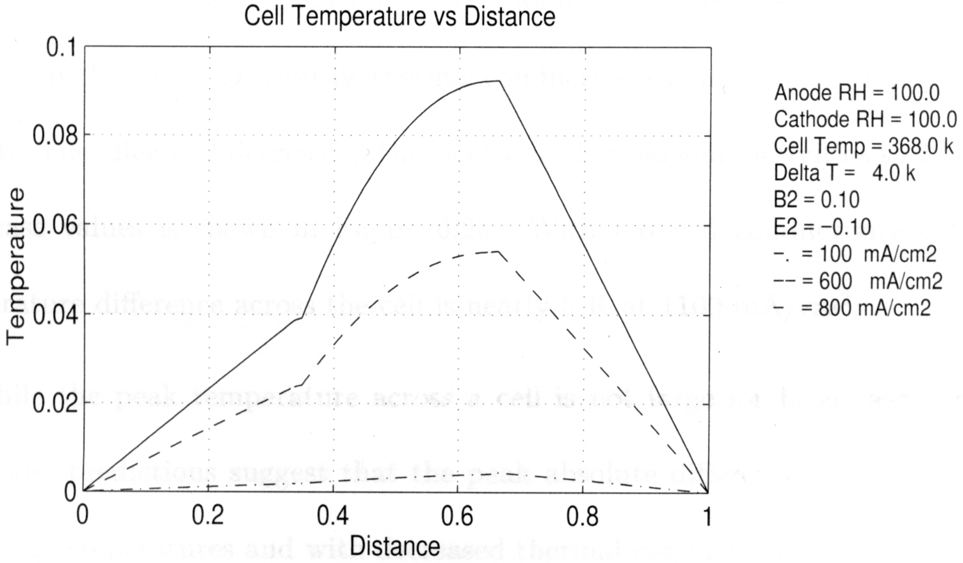

Figure 6.24: Cell temperature profile at $T_c = 368$ K.

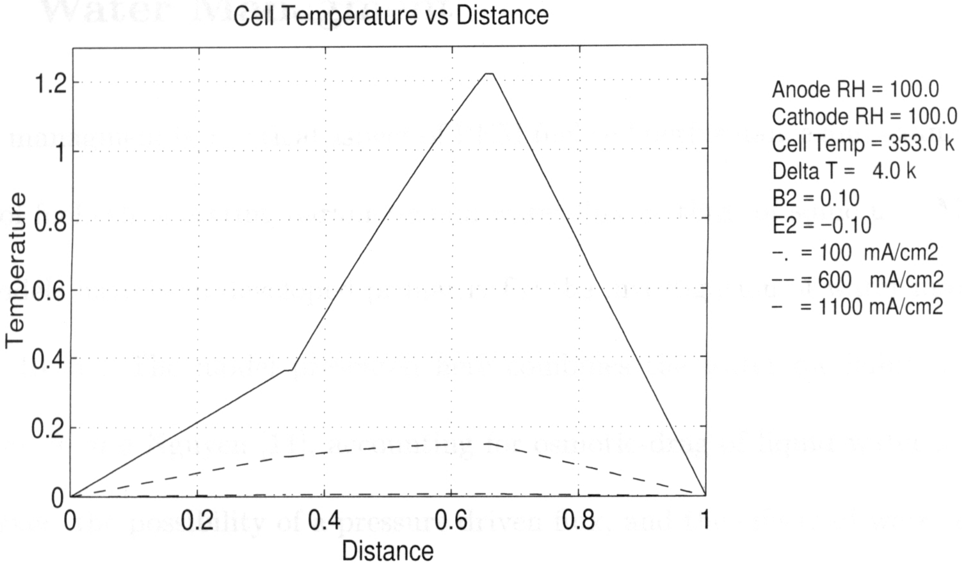

Figure 6.25: Cell temperature profile for an effective anode and cathode thermal conductivity of 0.004 W/cm-K.

the predicted temperature difference through the cell is small, the effects in a complete fuel cell stack could be significant where cooling plates are distributed periodically throughout the stack. Obviously, thermal conductivities impact heat transfer through the cell. The effects of decreasing the electrode thermal conductivities to 1/4 of their base case values is shown in Figure 6.25. With reduced conductivities, the peak temperature difference across the cell is nearly 5 K at 1100 mA/cm^2.

While the peak temperature across a cell is not large for base case conditions, the model predictions suggest that the peak absolute difference increases for lower operating temperatures and with decreased thermal conductivities.

6.3 Water Managment

Water managment is a critical aspect of PEM fuel cell performance and examining the effect of fuel cell operating parameters on water flux is, thus, of some use. Many fuel cell models have been developed primarily for the investigation of water managment [9, 11, 10, 5]. The model presented here combines the water modeling aspects of Springer [9] and Nguyen [11], accounting for osmotic-drag of liquid water across the membrane, the possibility of a pressure driven flux, and the effects of water diffusion due to variable membrane hydration. Although this thesis concentrates on overall cell performance, the inclusion of the basic equations describing water flux provides an area for further work in the future. With that in mind, the basic water flux and vaporization predictions of the model do give some insight into cell operation.

The net water flux across the membrane normalized by the current density is a common way of identifying the overall water-flux in a PEM cell. The work of Springer et al. predicts the net water flux per proton for a cell at 80 ^{0}C is 0.2 [9]. Figure 6.26 shows the net water flux predicted by this model for base case conditions. Unlike Springer's model, this model assumes the cathode catalyst is fully hydrated for all operating conditions. Because of this assumption, the net water flux at low current densities is from cathode to anode due to a concentration gradient in the membrane. This is evident in Figure 6.26 where the flux has values less than 0. As the current

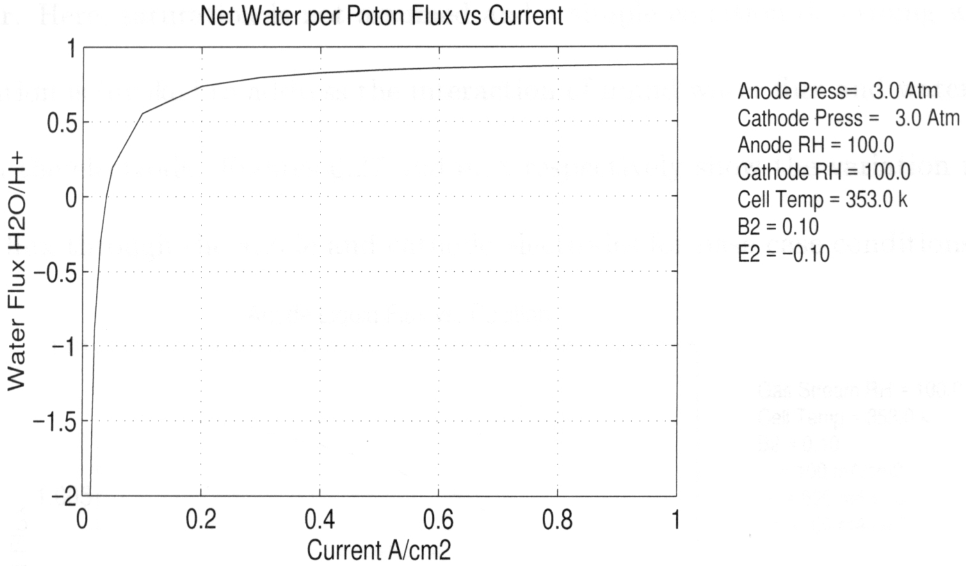

Figure 6.26: Net water flux across membrane for base case conditions.

density is increased, the net water flux reverses direction, becoming nearly asymptotic at a flux of 0.8 moles of water per mole of protons. Another assumption used here that differs from Springer's work is that the osmotic flux coefficient is constant at 1.0. Qualitatively, the model predictions for net water flux across the cell are consistant with Springer and Bernardi's models. Further refinement of this aspect of the model can be useful where detailed experimental data is available to validate predictions.

6.3.1 Electrode Water Transport

An interesting prediction of this model is the water flux through the electrodes. Bernardi and Verbrugge describe the water velocity profiles through the cell for various operating conditions assuming that the electrodes are saturated with water vapour. Here, saturation is not assumed and a simple equation describing water vaporization is invoked to address the interaction of liquid water flux and water vapour flux in the electrode. Figures 6.27 and 6.28 respectively show the variation in liquid water flux through the anode and cathode electrodes for base case conditions. As is expected, the vaporization or condensation of water is very low for fully humidified stream conditions.

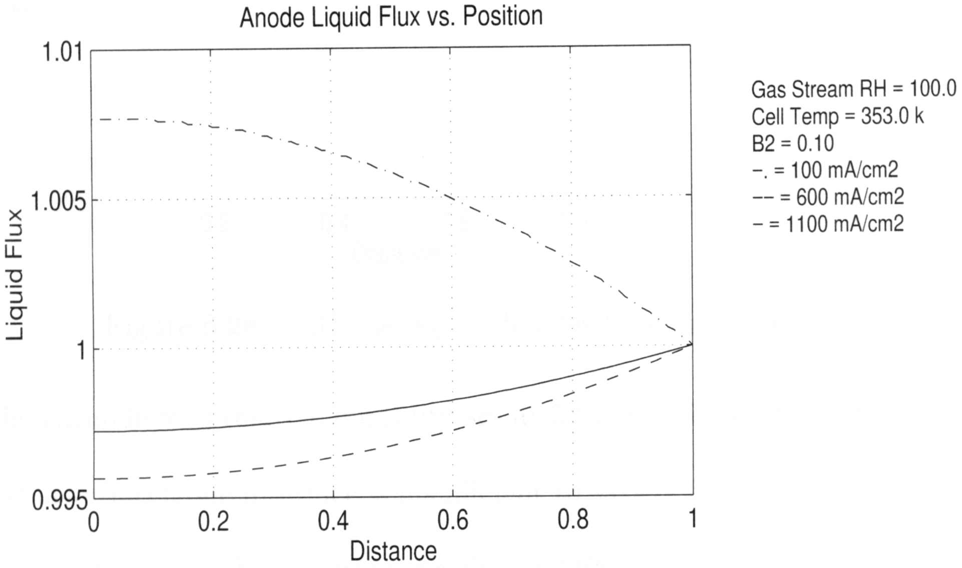

Figure 6.27: Anode liquid flux for base case conditions.

6.3.2 Cathode Humidification

The effect of low cathode gas stream humidification is shown in Figure 6.29 and Figure 6.30. The liquid flux values in these figures has been normalized by the liquid flux entering or leaving their respective electrode-catalyst layer interfaces. In Figure 6.29,

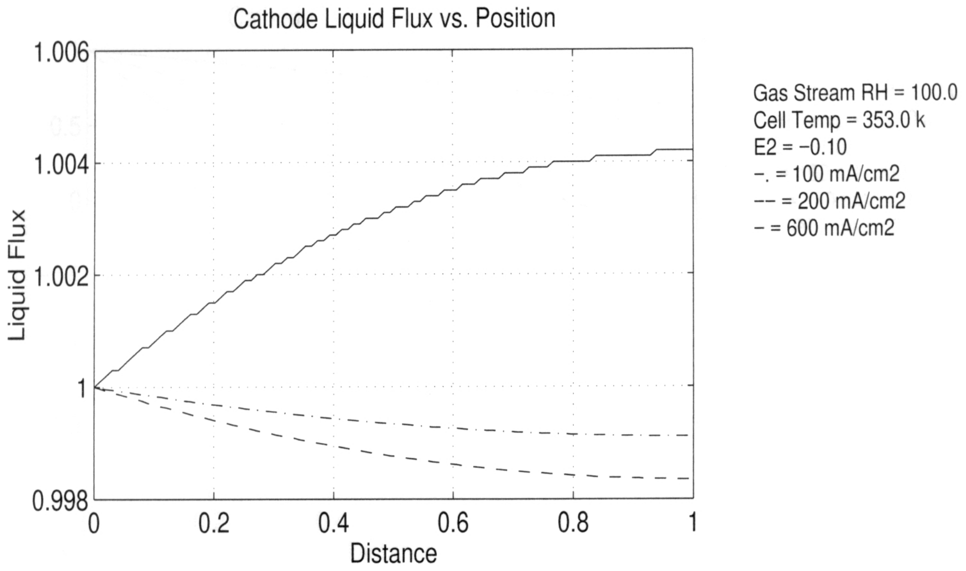

Figure 6.28: Cathode liquid flux for base case conditions.

with the cathode feed relative humidity set at 50%, the liquid water flux through the catalyst layer-electrode interface is insufficient to satisfy the effects of vaporization at low current densities. At a current density of 1100 mA/cm^2 the flux of liquid water satisfies vaporization demands without requiring an influx of liquid water from the gas channel.

These results suggest that given sufficient humidification in the anode (to satisfy the water flux demands across the membrane), it may be possible to reduce the humidification of the cathode gas stream at high operating currents. Removing the need for humidification can have several benefits. Lower humidification levels would allow the cathode gas stream pressure to be reduced because the effective mole fraction of oxygen in the stream would be higher. Moreover, operating at a lower cathode

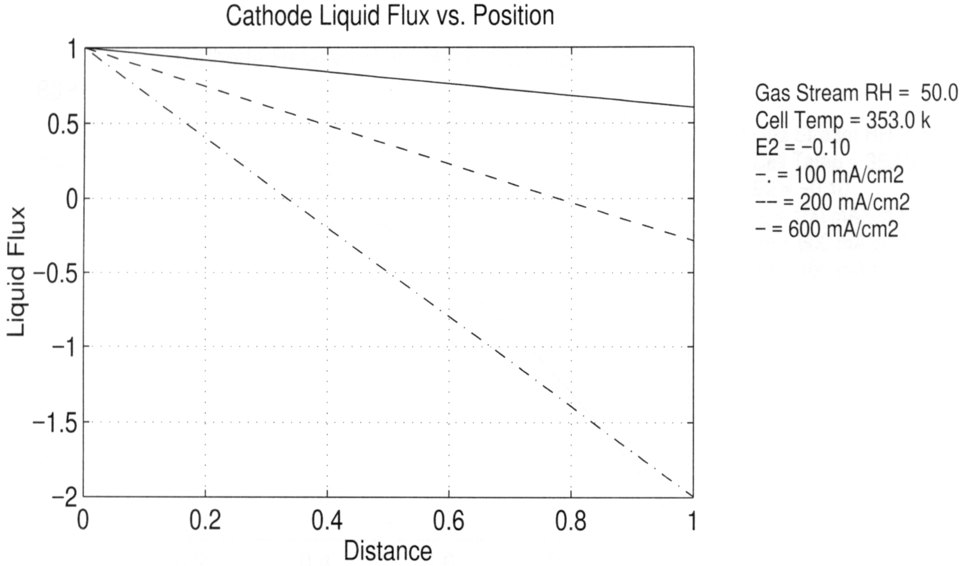

Figure 6.29: Cathode liquid flux for cathode gas stream relative humidity of 50%.

pressure would decrease the parasitic energy requirements of a compressor and would therefore increase net system efficiency.

6.3.3 Anode Humidification

Theoretical and experimental work concerning humidification of PEM cells indicates that fuel stream humidification is required for optimum cell performance under typical operating conditions [11, 9]. It is therefore useful to investigate low anode gas stream humidities.

Figure 6.31 depicts the variation in fuel stream relative humidity across the anode electrode with a humidification of 75%. Given the low humidity at the catalyst layer,

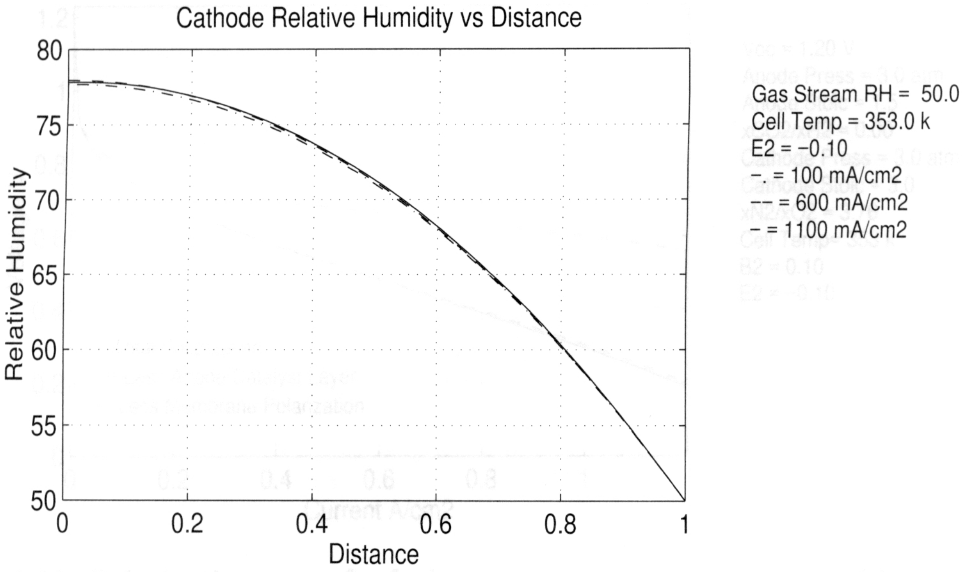

Figure 6.30: Cathode electrode relative humidity for cathode gas stream relative humidity of 50%.

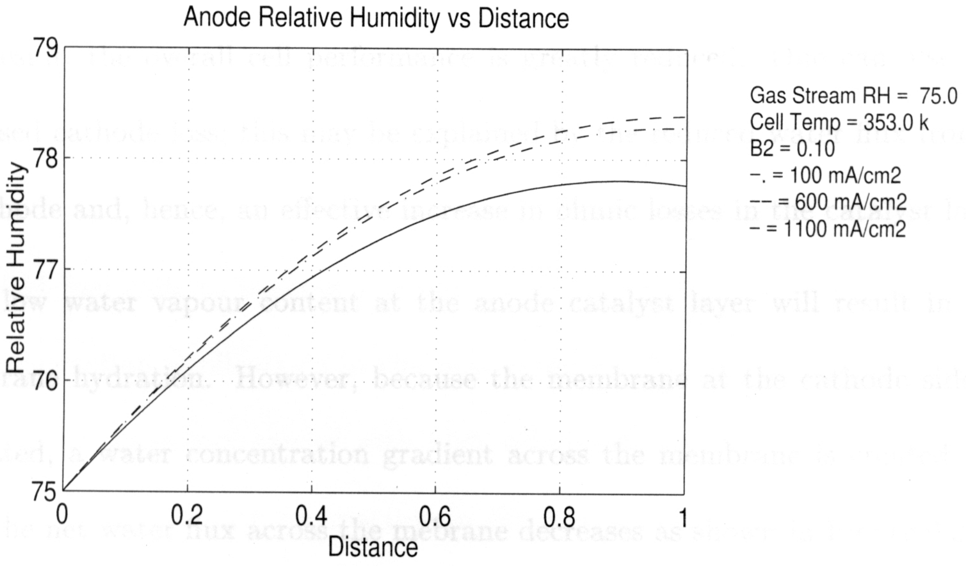

Figure 6.31: Fuel stream water vapour content for 75% inlet stream relative humidity.

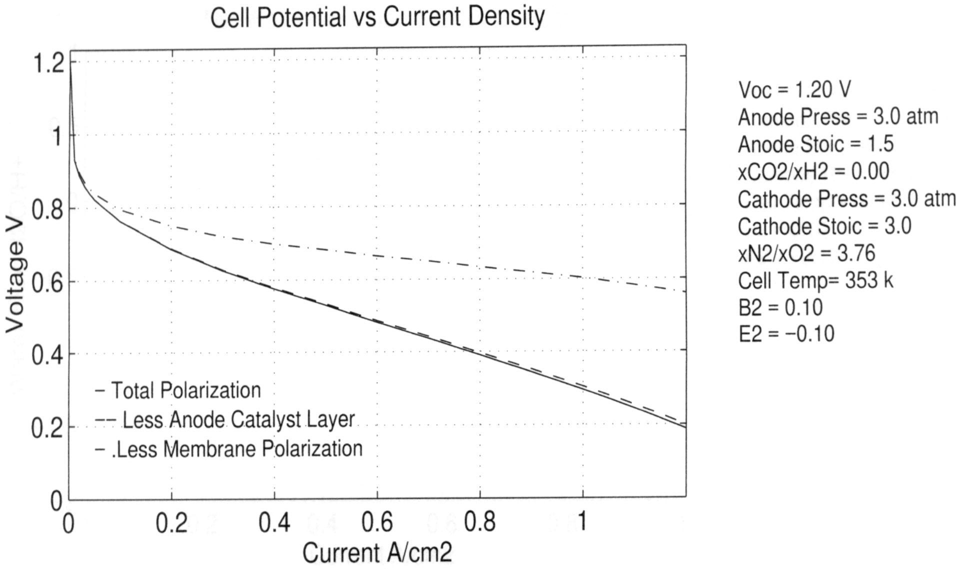

Figure 6.32: Polarization curve for fuel stream water vapour content of 75% with base case conditions.

one expects there to be an increase in membrane resistance. As can be seen in Figure 6.32, the membrane loss is much larger than with a fully humidified fuel stream and, as a result, the overall cell performance is greatly reduced. One can also note an increased cathode loss; this may be explained by the reduced water flux from anode to cathode and, hence, an effective increase in ohmic losses in the catalyst layer.

A low water vapour content at the anode catalyst layer will result in reduced membrane hydration. However, because the membrane at the cathode side is still saturated, a water concentration gradient across the membrane is created. In this case, the net water flux across the mebrane decreases as shown in Figure 6.33.

The model predictions for low anode gas stream humidities indicate that cell per-

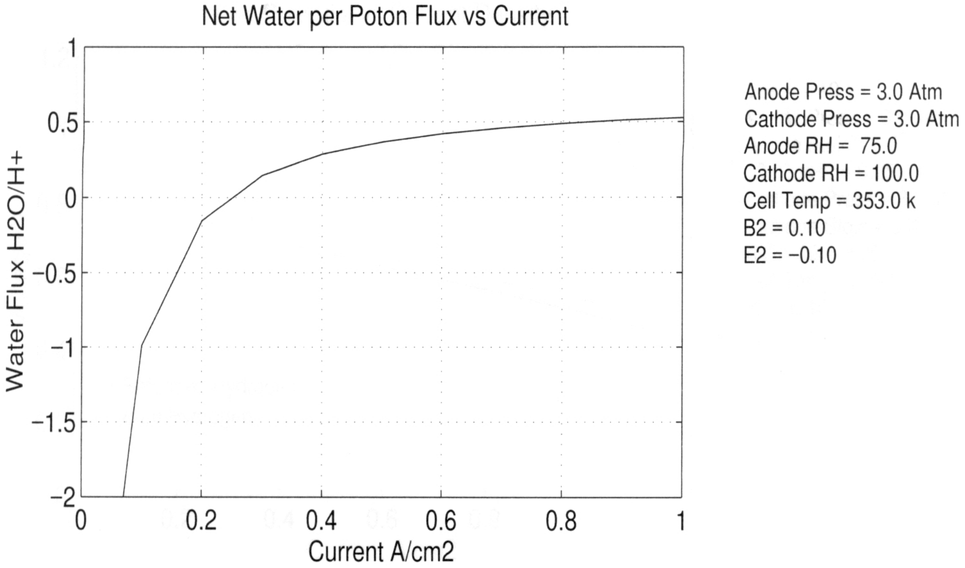

Figure 6.33: Net water flux across the membrane for base case conditions with 75% inlet anode fuel stream humidity.

formance decreases if suitable hydration of the anode catalyst layer is not maintained. This is consistant with experimental results for actual PEM cells.

6.4 Reformed Fuel

For PEM fuel cells to become a viable alternative to internal combusiton engines in transportation applications in the near term, the hydrogen used will have to be derived from an energy carrier with high volumetric energy density. This fuel will be converted to hydrogen for reaction in the fuel cell stack. Steam reforming of an hydrocarbon fuel is widely recognized as one of the most likely means of providing hydrogen to a PEM fuel cell system [4]. During the fuel reforming and conditioning

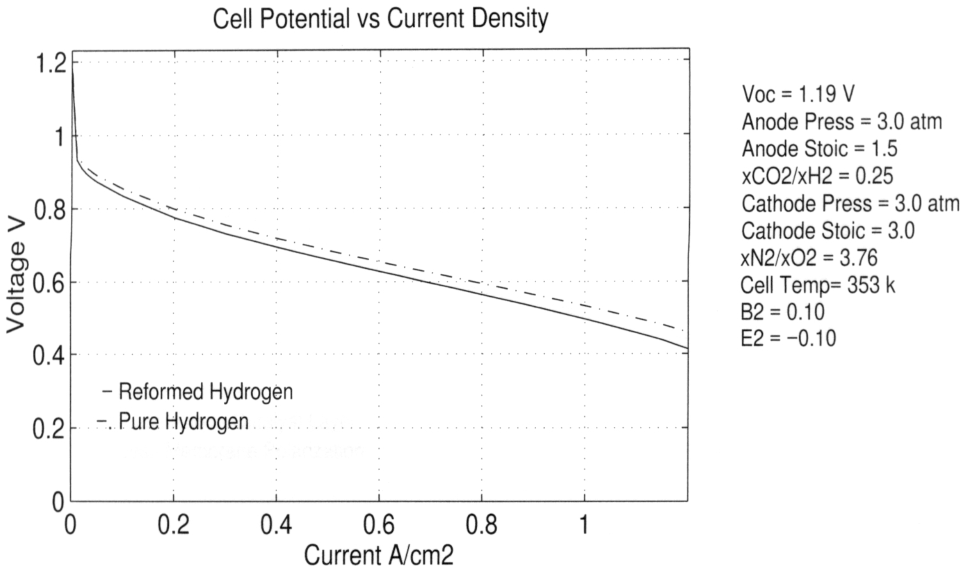

Figure 6.34: Polarization curve for operation with reformed fuel.

process, water is a necessary constituent. Since the anode reaction is extremely fast and has a low impact on overall cell polarization, diluting the anode feed stream has less impact than cathode stream dilution at typical operating stoichiometries. Thus, the anode appears to be a better place for humdification to occur whether it is by liquid water injection, wicking, or gas stream humidification. The benefits of not having to fully humidify the cathode stream have already been discussed.

One of the products of the reformation process is carbon dioxide. In the case of steam reforming of methanol, the resulting mole fraction of CO_2 relative to H_2 is approximately 0.25 in dry gas. Such an anode gas stream composition is modeled in Figure 6.34. At first glance, one may think that a decreased partial pressure of hydrogen in a reformed fuel stream is causing a significant decrease in cell performance

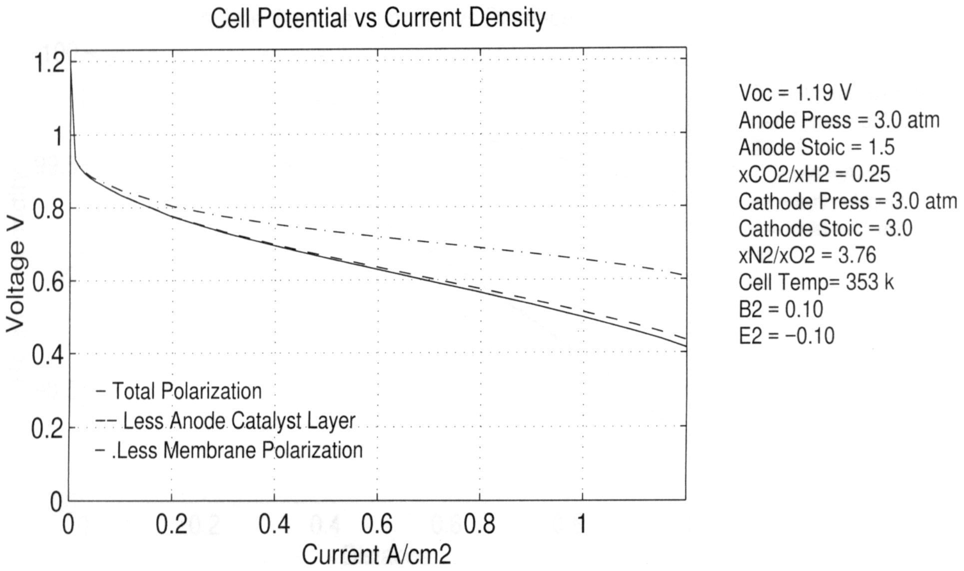

Figure 6.35: Polarization curve with high oxygen permeability for operation with reformed fuel showing anode and membrane losses.

over the entire operating range. However, by examining Figure 6.35 and comparing it to Figure 6.11 (which is the predicted curve for similar operating parameters other than fuel stream composition), it can be seen that the decrease in polarization is largely due to membrane losses. Figure 6.36 cleary shows a decrease in anode relative humidity at the catalyst layer interface under these operating conditions. This leads to a lower membrane hydration and decreased ionic conductivity which is responsible for the increase in membrane polarization. A small increase in anode polarization is also observable in Figure 6.35 when compared to Figure 6.11. The decreased mole fraction of hydrogen leads to a small increase in anode concentration and activation losses.

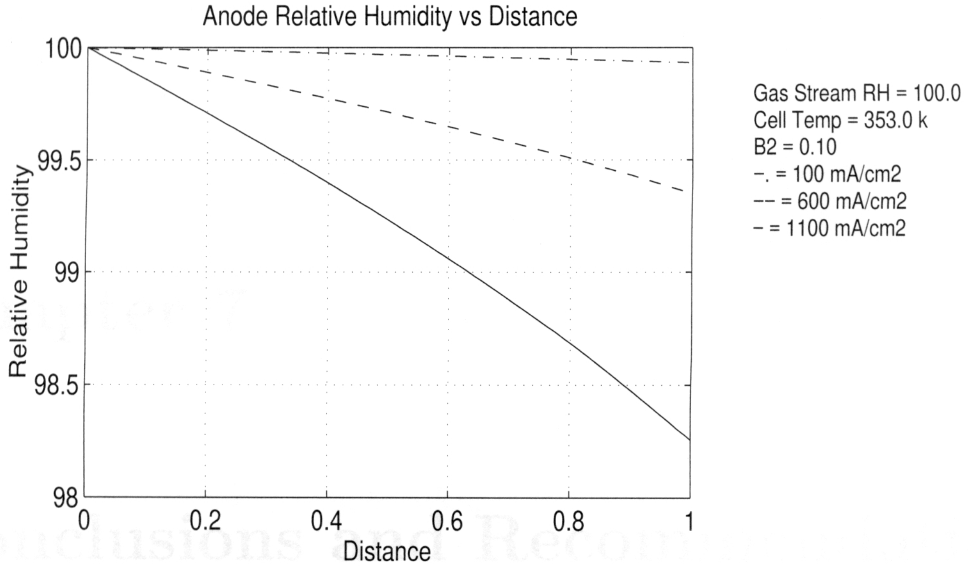

Figure 6.36: Anode relative humidity with reformed fuel stream.

The model results for operation on a reformed fuel stream predict that there is an increase in concentration and polarization losses at the anode. The vaporization model suggests that humidification may be more difficult with a fuel stream that includes a significant amount of carbon dioxide thereby leading to decreased performance because of reduced membrane hydration.

Chapter 7

Conclusions and Recommendations

7.1 Conclusions

This thesis describes the development of a comprehensive one-dimensional mathematical model of a Proton Exchange Membrane fuel cell. The model incorporates the possibility of ternary gas mixtures in each gas stream, operation with variable humidity gas streams, the effects of vaporization in the electrodes, variable membrane hydration, and energy conservation. A complete PEM cell is modeled, including the anode, allowing one to investigate many aspects of design and operation.

Performance predictions of the model compare well to experimentally verified data. Some model predictions of particular interest are:

- for fully humidified gas streams, the temperature profile across a cell operating at 80 ^{0}C and 1.1 A/cm^2 has a peak temperature difference of approximately 0.8 Kelvin. As cell operating temperature is increased the peak temperature difference appears to decrease. Lowering the operating temperature has the opposite effect. The effects of the predicted temperature profile may be more pronounced in a complete stack;

- it may be possible to reduce cathode humidification substantially at high operating currents. This could positively affect net system efficiencies by allowing the cathode pressure to be decreased;

- catalyst layer gas permeabilities appear to be higher than values determined in neat ionomer. If this is the case, catalyst utilization may be higher than suggested in some other models;

- gas diffusion in the electrode limits the maximum operating current density. Reducing the tortuosity or thickness of the electrode substrate may increase the maximum cell operating current and mitigate concentration polarizations in the electrode; and

- operating with a ternary gas mixture typical of reformed methanol as the anode feed stream increases anode polarization. Maintaining a well hydrated membrane may also be more difficult with reformed fuel use which could have a significant impact on overall cell polarization.

7.2 Recommendations

Although the model developed here attempts to address most of the important issues affecting PEM fuel cell performance, some further work is required to clarify operating processes:

- the electrode backing has a significant impact upon the maxmimum realizable operating current when using air as the reactant gas. To address the mass transport limitations in the electrode backing in more detail, the actual compressed porosity and tortuosity of the backing is required. The true compressed backing thickness needs to be confirmed as well. Measurements on actual cell assemblies are needed to quantify these figures;
- the vaporization of liquid in the electrodes and the rate at which water vapour condenses is important for accurately modeling mass and energy transport. The condensation of water in the electrode will affect the cell temperature profile, and the rate at which water vapour is absorbed into the membrane material will determine the water vapour flux at the catalyst layer boundaries. Depending on the operating conditions, this boundary flux could significantly affect the

overall transport of reactant to the catalyst layer. Measurements to determine the mass transfer coefficient for water vaporization in the electrode backing and for vapour absorption in the membrane would be beneficial;

- breaking the catalyst layer model into two layers could be useful depending on the MEA manufacturing method being explored. For a Nafion impregnated, hot-pressed assembly, the catalyst layer thickness is probably not of a uniform width. It would be interesting to model two distinct regions: one where the void space is completely filled with ionomer, and another where the void space is free to provide gas transport. Currently, an effective diffusion coefficient for one morphology is calculated; and
- incorporate the necessary equations to account for gas cross-over in the membrane layer.

Appendix A

Properties

A.1 Introduction

The physical properties affecting mass and heat transport are based upon experimental or empirical correlations wherever possible. Temperature correlations are employed to correct for different operating conditions and to describe the effects of temperature gradients within the cell. Assuming the temperature variation across the cell is relatively small, it is possible to neglect the variation in transport properties in the mathematical derivation for a given mean operating temperature. However, to approximate the effects of a temperature gradient on the transport properties, the average temperature across the layer is used to update relevant properties such as diffusion coefficients, thermal conductivities, and reaction rates. Furthermore, the average hydration across the membrane is used to determine membrane properties.

A.2 Gas Properties

The enthalpy, entropy and Gibb's free energy of a gaseous species at a given temperature are determined in Chapter 2 and will not be discussed further.

The latent heat of vaporization for water in J/mole is calculated using the expression:

$$\begin{aligned} \bar{h}_{vap} = 45070.0 - 41.9 \times T &+ 3.44 \times 10^{-3} T^2 \\ &+ 2.54 \times 10^{-6} T^3 - 8.98 \times 10^{-10} T^4, \end{aligned} \tag{A.1}$$

where T is in Celsius [11].

The binary diffusion coefficients, D_{ij}, are calculated with the empirical correlation of Fuller, Schettler, and Giddings [32]

$$D_{ij} = \frac{10^{-3} T^{1.75} [(W_i + W_j)/W_i W_j]^{0.5}}{p[(\Sigma v)_i^{\frac{1}{3}} + (\Sigma v)_j^{\frac{1}{3}}]^{2.0}}, \tag{A.2}$$

and are corrected for electrode porosity, ϵ_e, and tortuosity, τ, by the relation:

$$D_{ij}^{\text{eff}} = \frac{\epsilon_e}{\tau} D_{ij}, \tag{A.3}$$

where the values of ϵ_e and τ are those used by Springer et al. (to describe E-Tek electrodes ($\epsilon_e = 0.4$, $\tau = 7.0$) [22]) unless otherwise stated. The diffusion coefficient in Eqn (A.2) is in cm^2/s when the total pressure, p, is in atmospheres, and the temperature, T, is in Kelvin. The symbol, W, represents the molar mass of a species in g/mole, and the molecular diffusion volumes (an emprical dimensionless correction factor), (Σv), are given in Table A.1 [32].

Anode	Cathode
$(\Sigma v)_{H_2} = 7.07$	$(\Sigma v)_{O_2} = 16.6$
$(\Sigma v)_{CO_2} = 26.9$	$(\Sigma v)_{N_2} = 17.9$
$(\Sigma v)_{H_2O} = 12.7.$	

Table A.1: Diffusion Volumes

The thermal conductivity of a gaseous mixture is calculated using the Wassiljewa equation [32]:

$$k_{\text{mix}} = \Sigma_{i=1}^{n} \left(\frac{x_i k_i}{\Sigma_{j=1}^{n} x_j A_{ij}} \right). \tag{A.4}$$

Here, k_{mix} is the thermal conductivity of the gas mixture, k_i is the thermal conductivity of a pure component, x_i is the mole fraction of component i and n is the number of species in the mixture. The coefficient A_{ij} is determined using the Lindsay and

Bromley modification of the Sutherland model [32],

$$A_{ij} = 0.25 \left\{ 1 + \left[\frac{\mu_i}{\mu_j} \left(\frac{W_j}{W_i} \right)^{0.75} \frac{T + \bar{S}_i}{T + \bar{S}_j} \right]^{0.5} \right\}^2 \frac{T + \bar{S}_{ij}}{T + \bar{S}_i}. \tag{A.5}$$

where μ is the pure gas viscosity, and $\bar{S}$ is the Sutherland constant. The modification used to determine the Sutherland constant is,

$$\bar{S}_i = 1.5 T_{bi}, \tag{A.6}$$

where T_{bi} is the normal boiling point of species i in Kelvin. The interaction Sutherland constant $\bar{S}_{ij}$ is determined by

$$\bar{S}_{ij} = \bar{S}_{ji} = (\bar{S}_i \bar{S}_j)^{0.5}. \tag{A.7}$$

The values for the boiling points are given in Table A.2 [32]. It should be noted that the value for hydrogen is not the normal boiling point, but is instead a recommended empirical value to use in the correlation [32]. The viscosity of a pure gas at a specified

Anode	Cathode
$T_b(H_2) = 79.0$ K	$T_b(O_2) = 90.2$ K
$T_b(CO_2) = 194.7$ K	$T_b(N_2) = 77.4$ K
$T_b(H_2O) = 373.15$ K	

Table A.2: Normal Boiling Points

temperature is calculated based on the Chapman-Enskog theory for low pressure gases where the viscosity in micropoise is given by [32]

$$\eta = 26.69\frac{(WT)^{0.5}}{\sigma^2\Omega_v}. \tag{A.8}$$

where σ is the hard-sphere diameter in Angstroms, and Ω_v is the collision integral determined from the relation,

$$\Omega_v = \frac{A}{T^{*B}} + \frac{C}{\exp(DT^*)} + \frac{D}{\exp(FT^*)} \tag{A.9}$$

where

$$T^* = \left(\frac{k}{\epsilon}\right)T$$

and

$$A = 1.16145 \quad D = 0.77320$$

$$B = 0.14874 \quad E = 2.16178$$

$$C = 0.52487 \quad F = 2.43787.$$

The values for $\left(\frac{k}{\epsilon}\right)$ and σ are as given in Table A.3 [32].

The saturation pressure of water vapour in atmospheres at a given temperature

Anode	Cathode
$\left(\frac{k}{\epsilon}\right)_{H_2} = 59.7$ $\sigma_{H_2} = 2.827$	$\left(\frac{k}{\epsilon}\right)_{O_2} = 106.7$ $\sigma_{O_2} = 3.467$
$\left(\frac{k}{\epsilon}\right)_{CO_2} = 195.2$ $\sigma_{CO_2} = 3.941$	$\left(\frac{k}{\epsilon}\right)_{O_2} = 71.4$ $\sigma_{N_2} = 3.798$
$\left(\frac{k}{\epsilon}\right)_{H_2O} = 809.1$ $\sigma_{H_2O} = 2.641$	

Table A.3: Gas Viscosity Coefficients

in degrees celsius is determined by the relation [11]

$$\log p_{sat} = -2.1794 + 0.02953T - 9.1837 \times 10^{-5}T^2 + 1.4454 \times 10^{-7}T^3. \quad \text{(A.10)}$$

A.3 Membrane Properties

The hydration of the membrane in the anode catalyst layer is determined by the activity of the water vapour at the electrode-catalyst layer interface. An empirical correlation based on the adsorption isotherm of Nafion 117 is used with an allowance for the activity to exceed unity. A maximum hydration of 16.8 is assumed in the presence of liquid water as measured by Zawodzinski for Nafion 117 immersed in water at 80 ^{0}C [9]. The hydration is assumed to vary linearly from 14 to 16.8 when the mole fraction of water vapour exceeds saturation up to $3x_{sat}$ in a manner similar to that used by Springer [9]:

$$\begin{aligned}
\lambda &= 0.043 + 17.81a - 39.85a^2 + 36.0a^3, \qquad 0 < \frac{x_3 p}{p_{sat}} \leq 1 && \text{(A.11)} \\
\lambda &= 14 + 1.4\left(\frac{x_3 p}{p_{sat}} - 1\right), \qquad 1 < \frac{x_3 p}{p_{sat}} \leq 3. && \text{(A.12)}
\end{aligned}$$

The diffusion coefficient for liquid water in the membrane is determined as a function of membrane hydration and temperature [9],

$$D_3 = 10^{-6} \exp\left[2416\left(\frac{1}{303} - \frac{1}{T}\right)\right] \times (2.563 - 0.33\lambda + 0.0264\lambda^2 - 0.000671\lambda^3). \tag{A.13}$$

The diffusion coefficient for oxygen is determined by a similar function [19],

$$D_{O_2} = 2.88 \times 10^{-6} \exp\left[2933\left(\frac{1}{313} - \frac{1}{T}\right)\right]. \tag{A.14}$$

And, the diffusion coefficient for hydrogen is determined by [7],

$$D_{H_2} = 4.1 \times 10^{-3} \exp\left[-2602\left(\frac{1}{T}\right)\right]. \tag{A.15}$$

The above diffusion coefficients are all in units of cm^2/s.

The hydraulic permeability of the membrane is assumed to be a constant value of

1.8×10^{-14} cm^2 [7], and the volume fraction of water in membrane, $\epsilon_w^{\mathrm{mem}}$, is assumed to vary linearly with hydration up to a maximum value of 0.35 for fully hydrated Nafion 117 [33] (this parameter varies considerably amongst different membranes):

$$\epsilon_w^{\mathrm{mem}} = 0.35\left(\frac{\lambda}{16.8}\right). \tag{A.16}$$

The ionic conductivity of Nafion 117, κ, in $[\Omega\text{-cm}]^{-1}$ is calculated as a function of hydration and temperature [9],

$$\kappa = \exp\left[1268\left(\frac{1}{303} - \frac{1}{T}\right)\right](0.005139\lambda - 0.00326). \tag{A.17}$$

The viscosity of liquid water, μ, in centipoise is calculated from [32],

$$\log\mu = 658.25\left(\frac{1}{T} - \frac{1}{283.16}\right). \tag{A.18}$$

The thermal conductivity of the bulk membrane is approximated based on the volume fraction of water in the membrane (a function of hydration). As the backbone of the polymer structure is PTFE, it is assumed that the thermal conductivity of dry membrane is equal to that of PTFE. A constant value of 0.00673 W/cm-K is used for water and a value of 0.0024 W/cm-K is used for PTFE [34]. The bulk conductivity is then,

$$k_m = \epsilon_w^{\text{mem}} k_{H_2O} + (1 - \epsilon_w^{\text{mem}}) k_{PTFE} \tag{A.19}$$

The Wilke-Chang correlation is used to calculate the diffusion coefficient for hydrogen and oxygen in water as a function of temperature [32],

$$D_{i\ell} = 7.4 \times 10^{-8} \left[\frac{(\phi W_w)^{0.5} T}{\mu V_{mi}^{0.6}} \right]. \tag{A.20}$$

The difffusion coefficient is in units of cm^2/s. The association factor of water, ϕ, and the molar volumes of solute at their normal boiling points, V_{mi}, are given in Table A.4.

Hydrogen	Oxygen
$V_m = 14.3 \frac{cm^3}{g-mol}$	$V_m = 25.6 \frac{cm^3}{g-mol}$
$\phi_{H_2O} = 2.26$	

Table A.4: Wilke-Chang Coefficients

The solubility of hydrogen and oxygen in Nafion 117 is determined by Henry's number:

$$c_i = \frac{p_i}{H_i} \tag{A.21}$$

The expression used by Bernardi and Verbrugge describes Henry's constant for oxygen as a function of temperature is,

$$H_{O_2} = \exp\left(\frac{-666.0}{T} + 14.1\right) \tag{A.22}$$

while a constant value of $H_{H_2} = 4.5 \times 10^4$ atm-cm^3/mole is used for hydrogen [7]. For the solubility of each of these species in water, constant values of Henry's number at 350 K are used; for hydrogen, $H_{H_2} = 143 \times 10^4$ atm-cm^3/mole and for oxygen, $H_{O_2} = 124 \times 10^4$ atm-cm^3/mole [34].

A.4 Kinetic Parameters

The most important parameter describing reaction kinetics at each electrode is the exchange current density, i_0. The exchange current density for the anode is much higher than that of the cathode and is reflected in the fact that the anode activation polarization is often neglected in many models. In this paper the anode exchange current density is assumed to be temperature independent and is set as, $i_0^{\text{anode}} = 0.055$ A/cm^2 [8]. The exchange current density in A/cm^2 for the cathode is a function of temperature and is determined by [19],

$$i_0^{\text{cathode}} = 7.33 \times 10^{-10} \exp\left[8999\left(\frac{1}{313} - \frac{1}{T}\right)\right]. \tag{A.23}$$

A.5 Bulk Parameters

The effective transport parameters for thermal conductivity, electrical conductivity and mass diffusion in each of the layers are approximated by using the sum of the volume weighted parameters for each component that makes up the layer (except for the mass diffusion coefficients in the electrodes. These are discussed in Section A.2.) In the case of the effective thermal conductivity for the catalyst layer a parallel resistance analogy is used,

$$k^{\text{eff}} = \epsilon_m k_m + \epsilon_s k_s + \epsilon_w k_w, \tag{A.24}$$

where the conductivity is determined by the volume fractions, ϵ, of the components making up the layer: membrane, solid (catalyst) and water. The thermal conductivity of the solid electrodes is assumed to be approximately 0.026 W/cm-K.

The bulk diffusion coefficient for oxygen in the cathode catalyst layer is determined by the volume fractions of membrane, water and void space and by using a parallel resistance analogy. Typically, a series resistance approximation is used; however, a parallel analogy seems to better approximate the empirical permeabilities reported for Nafion impregnated, hot-pressed, catlayst layer structures [27]:

$$D_1 = \epsilon_m D_1^{\text{mem}} + \epsilon_w D_1^w + \epsilon_{void} D_{ij} \tag{A.25}$$

where, D_{ij} is the taken as the diffusion coefficient of oxygen in nitrogen for air operation and oxygen in water vapour for neat-O_2 operation. In the case of the anode, a similar approximation is made; however, for reformed fuel, D_{ij} is the diffusion coefficient of hydrogen in carbon dioxide. The effective diffusion coefficient for the catalyst layer is then determined by modifying for the porosity of the layer,

$$D_1^{\text{eff}} = (1 - \epsilon_s)D_1. \tag{A.26}$$

A tortuosity correction is not employed here as there is no information available regarding the value of this parameter in a typical catalyst layer structure. The effective electrical conductivity of the membrane phase in the catalyst layers is modified for porosity in a similar manner.

The active surface area in the catlayst layers, a, can be set arbitrarily or is approximated by the following relation:

$$a = \frac{mA}{t_l} \tag{A.27}$$

where m is mass of catalyst per geometric area, A is the reactive surface area per unit mass of catalyst and t_l is the catalyst layer thickness.

To determine the vaporization rate in the electrodes the Sherwood number, surface area of liquid water per unit volume, f_e, and the length scale L, are set as a grouped parameter. Thus, the value of $\frac{sh\, f_e}{L}$ is adjusted to maintain the relative humidity in the electrodes at approximately 100% when saturated gas streams are used. This value is then used for other simulations.

Appendix B

Solution Method

B.1 Numerical Method

The mathematical model described is essentially a boundary value problem. To solve the coupled differential equations a banded matrix solver known as MBAND is used. MBAND is based on a pentadiagonal solver developed by Newman [35] that provides fourth order accuracy for systems of second-order differential equations [36, 35]. Subsequently, Fan et al. modified this solution method to be able to solve systems with interior boundary conditions, like those in battery and fuel cell models [37, 38]. Previously, this type of problem could be solved using Newman's pentadiagonal solver; however, this proved to be numerically intensive. MBAND has been shown to be much more computationally efficient [38].

To solve a system of non-linear, coupled, second-order equations using MBAND, one must first discretize the differential equations using forward, backward, or central differences (depending on the order of the equation and the given boundary conditions). With the equations in finite difference form and written as being equal to zero, the recurrence relations describing the elements of a Jacobian matrix are determined. For a non-linear set of equations, a first guess must be given and then iteration is used in a Newton-Raphson procedure to converge to the system solution. This procedure is used for each layer in sequence. After all five layers have been solved, the non-dimensional parameters and boundary conditions are up-dated and the layers are solved again. This is repeated until the relative errors of the unknowns are specified to within a set tolerance.

B.2 Boundary Conditions

The mathematical representation of the fuel cell consists of five regions made up of a number of coupled, non-linear, ordinary differential equations. Physically, these equations describe the variation of species and energy flux between the two boundaries defined as the interfaces between the electrodes and the gas channels. The operating conditions are specified at either boundary as are interface conditions at the interior boundaries. There are four differential equations describing the electrode layers, three of which are first-order equations. Thus, five boundary conditions are required. Table B.1 and Table B.2 list the boundary conditions for the anode and cathode electrodes.

The mole fractions of gas species at the boundaries a and f are determined based upon the set stoichiometric flow rate of gas and the humidification of the streams. The average composition between inlet and outlet is determined using an integral material balance on the gas chambers in a similar manner to Bernardi [6]. The effective mole fraction of species 1 is determined by taking the average of the inlet and outlet conditions,

$$x_1^{\text{eff}} = \frac{1 - x_3}{1 + \frac{x_{21}}{2}\left(1 + \frac{\zeta}{\zeta - 1}\right)} \tag{B.1}$$

where x_{21} is the molar ratio of species 2 to 1 as dry gas, and ζ is the stoichiometric flow rate.

	Anode Electrode	
Equation	a	b
x_1	$x_{H_2} = A1$	
x_2	$x_{CO_2} = A2$	
T	$T = A3$	$-k_e^{\text{eff}}\frac{dT}{dx} = -k_{al}^{\text{eff}}\frac{dT}{dx} - N_3\bar{h}_{vap}$
N_3		$N_3 = A4$

Table B.1: Anode Electrode Boundary Conditions

N_3 is the water vapour flux at the electrode-catalyst layer interface. If it is assumed that liquid water and water vapour are in local equilibrium throughout the electrode,

	Cathode Electrode	
Equation	e	f
x_1		$x_{O_2} = F1$
x_2		$x_{N_2} = F2$
T	$-k_{cl}^{\text{eff}}\frac{dT}{dx} - N_3\bar{h}_{vap} = -k_e^{\text{eff}}\frac{dT}{dx}$	$T = F3$
N_3	$N_3 = E4$	

Table B.2: Cathode Electrode Boundary Conditions

then N_3 can be set by solving the Stefan-Maxwell equation for vapour flux with saturated gas. One may also set the boundary condition for N_3 based upon the rate of vaporization at the interface. In this thesis the non-dimensional vapour flux is set arbitrarily.

For the catalyst layers, there are five, coupled, differential equations, two of which are second order. The boundary conditions for the catalyst layers are given in Table B.3 and Table B.4. The membrane potential at interface b is set to 0.

	Anode Catalyst Layer	
Equation	b	c
i_m		$i_m = I$
T	$T = T_e$	$-k_{al}^{\text{eff}}\frac{dT}{dx} = -k_{mem}\frac{dT}{dx}$
c_1	$c_{H_2} = \frac{x_{H_2}p_A}{H_{H_2}^{\text{eff}}}$	$-D_{H_2}^{\text{eff}}\frac{dC_{H_2}}{dx} + c_{H_2}N_w = 0$
Φ_m	$\Phi_m = 0$	
Φ_s	$\frac{d\Phi_s}{dx} = -\frac{I}{\sigma^{\text{eff}}}$	

Table B.3: Anode Catalyst Layer Boundary Conditions

The membrane layer is described by two, independent, differential equations. The

	Cathode Catalyst Layer	
Equation	d	e
i_m	$i_m = I$	
T	$T = T_{mem}$	$-k_{mem}\frac{dT}{dx} = -k_{cl}^{\text{eff}}\frac{dT}{dx} + N_3\bar{h}_{vap}$
c_1	$-D_{O_2}^{\text{eff}}\frac{dC_{O_2}}{dx} + c_{O_2}N_w = 0$	$c_{O_2} = \frac{x_{O_2}pC}{H_{O_2}^{\text{eff}}}$
Φ_m	$\Phi_m = \Phi_{m,mem}$	
Φ_s		$\frac{d\Phi_s}{dx} = -\frac{I}{\sigma^{\text{eff}}}$

Table B.4: Cathode Catalyst Layer Boundary Conditions

boundary conditions for temperature and membrane potential are given in Table B.5 The boundaries, a-f, are defined in Table B.6. The subscripts e, al, and cl stand for electrode, anode catalyst layer and cathode catalyst layer respectively.

	Membrane	
Equation	c	d
T	$T = T_{cl}$	$-k_{mem}\frac{dT}{dx} = -k_{cl}^{\text{eff}}\frac{dT}{dx}$
Φ_m	$\Phi_m = \Phi_{mcl}$	

Table B.5: Membrane Boundary Conditions

Boundary	Interface
a	Anode Gas Channel
b	Anode Electrode-Catalyst Layer
c	Anode Catalyst Layer-Membrane
d	Cathode Membrane-Catalyst Layer
e	Cathode Catalyst Layer-Electrode
f	Cathode Gas Channel

Table B.6: Boundaries

References

[1] D. S. Scott and W. Hafele. The coming hydrogen age: Preventing world climatic disruption. *International Journal of Hydrogen Energy*, 15(10):727–737, 1990.

[2] Choosing an alternative transportation fuel - air pollution and greenhouse gas impacts. Organization for Economic Co-operation and Development, 1993.

[3] U.S. DOE Energy Information Administration. 1996 u.s. energy flow. Web Site.

[4] R. F. Mann J. C. Amphlett and B.A. Peppley. On-board hydrogen purification for steam reformation/pem fuel cell vehicle power plants. *International Journal of Hydrogen Energy*, 21(8):673–678, 1996.

[5] Dawn M. Bernardi. Water balance calculations for solid-polymer-electrolyte fuel cells. *J. Electrochem. Soc.*, 137(11):3344–3345, November 1990.

[6] Dawn M. Bernardi and Mark W. Verbrugge. Mathematical model of a gas dif-

fusion elelctrode bonded to a polymer electrolyte. *AIChE Journal*, 37(8):1151–1163, August 1991.

[7] Dawn M. Bernardi and Mark W. Verbrugge. A mathematical model of the solid-polymer-electrolyte fuel cell. *J. Electrochem. Soc.*, 139(9):2477–2491, September 1992.

[8] Jiang-Tao Wang and Robert F. Savinell. Simulation studies on the fuel electrode of a h2-o2 polymer electrolyte fuel cell. *Electrochimica Acta*, 37(15):2737–2745, 1992.

[9] T. A. Zawodzinski T. E. Springer and S. Gottesfeld. Polymer electrolyte fuel cell model. *J. Electrochem. Soc.*, 138(8):2334–2342, August 1991.

[10] Thomas F. Fuller and John Newman. Water and thermal management in solid-polymer-electrolyte fuel cells. *J. Electrochem. Soc.*, 140(5):1218–1225, May 1993.

[11] Trung V. Nguyen and Ralph E. White. A water and heat management model for proton-exchange-membrane fuel cells. *J. Electrochem. Soc.*, 140(8):2178–2186, August 1993.

[12] M. S. Wilson T. E. Springer and S. Gottesfeld. Modeling and experimental diagnostics in polymer electrolyte fuel cells. *J. Electrochem. Soc.*, 140(12):3513–3526, December 1993.

[13] Yong Woo Rho et al. Mass transport phenomena in proton exchange membrane fuel cells using o2/he, o2/ar, and o2/2 mixturesnn2 m. *J. Electrochem. Soc.*, 141(8):2084–2096, August 1994.

[14] J. C. Amphlett et al. Performance modeling of the ballard mark iv solid polymer electrolyte fuel cell. *J. Electrochem. Soc.*, 142(1):1–15, January 1995.

[15] Junbom Kim et al. Modeling of proton exchange membrane fuel cell performance with an empirical equation. *J. Electrochem. Soc.*, 142(8):2670–2674, August 1995.

[16] S. A. Grot K. R. Weisbrod and N.E. Vanderborgh. Through-the-electrode model of a proton exchange membrane fuel cell. *Electrochemical Society Proceedings*, 95-23:152–166, 1995.

[17] M. J. Moran and H. N. Shapiro. *Fundamentals of Engineering Thermodynamics.* John Wiley & Sons, inc., 1995.

[18] John S. Newman. *Electrochemical Systems.* Prentice Hall, 2 edition, 1991.

[19] Supramaniam Srinivasan Arvind Parthasarathy and A. John Appleby. Temperature dependence of the electrode kinetics of oxygen reduction at the platinum/nafion interface- a microelectrode investigation. *J. Electrochem. Soc.*, 139(9):2530–2537, September 1992.

[20] Markku J. Lampinen and Marina Fomino. Analysis of free energy and entropy

changes for half-cell reactions. *J. Electrochem. Soc.*, 140(12):3537–3546, December 1993.

[21] Charles R. Derouin Edson A. Ticianelli and Supramaniam Srinivasan. Localization of platinum in low catalyst loading electrodes to attain high power densities in spe fuel cells. *J. Electroanal. Chem.*, 251:275–295, 1988.

[22] T. E. Springer et al. Characterization of polymer electrolyte fuel cells using ac impedance spectroscopy. *J. Electrochem. Soc.*, 143(2):587–599, February 1996.

[23] W. Vogel et al. The rate controlling step for electrochemical oxidation of hydrogen on pt in acid and poisoning of the reaction by co. *Electrochimica Acta*, 20:79–93, 1975.

[24] Thomas A. Zawodzinski et al. Water uptake by and transport through nafion 117 membranes. *J. Electrochem. Soc.*, 140(4):1041–1047, April 1992.

[25] T. A. Zawodzinski et al. A comparitive study of water uptake and transport through ionomeric fuel cell membranes. *J. Electrochem. Soc.*, 140(7):1981–1985, July 1993.

[26] J. G. Beery E. A. Ticianelli and Supramaniam Srinivasan. Dependence of performance of solid polymer electrolyte fuel cells with low platinum loading on

morphologic characteristics of the electrodes. *Journal of Applied Electrochemistry*, 21:597–605, 1991.

[27] K. Broka and P. Ekdunge. Oxygen and hydrogen permeation properties and water uptake of nafion 117 membrane and recast film for pem fuel cell. *Journal of Applied Electrochemistry*, 27:117–123, 1997.

[28] J. Fournier et al. High-performance, low pt content catalysts for the electroreduction of oxygen in polymer-electrolyte fuel cells. *J. Electrochem. Soc.*, 144(1):145–154, January 1997.

[29] Makoto Uchida et al. Investigation of microstructure in the catalyst layer and effects of both perfluorosulfonate ionomer and ptfe-loaded carbon on the catalyst layer of polymer electrolyte fuel cells. *J. Electrochem. Soc.*, 142(12):4143–4149, 1995.

[30] Ashok K. Vijh Siyu Ye and Le H. Dao. A new fuel cell electrocatalyst based on highly porous carbonized polyacrylonitrile foam with very low platinum loading. *J. Electrochem. Soc.*, 143(1):L7–L9, January 1996.

[31] H.H. Voss D. P. Wilkinson and K. Prater. Water management and stack design for polymer fuel cells. *Journal of Power Sources*, 49:117–127, 1994.

[32] J. M. Prausnitz R. C. Reid and T. K. Sherwood. *The Properties of Gases and Liquids.* McGraw-Hill book Company, 3 edition, 1977.

[33] Masonobu Wakizoe Felix N Buchi and Suprmaniam Srinivasan. Microelectrode investigation of oxygen permeation in perfluorinated proton exchange membranes with different equivalent weights. *J. Electrochem. Soc.*, 143(3):927–932, March 1996.

[34] V. E.Denny D. K. Edwards and A. P. Mills. *Transfer Processes.* Holt, Rinehart & Winston, Inc., 1973.

[35] John S. Newman. Numerical solution of coupled, ordinary differential equations. *Ind. Eng. Chem. Fundamentals*, 7(3):514–517, August 1968.

[36] John Van Zee et al. Extension of newman's numerical technique to pentadiagonal systems of equations. In Ralph E White, editor, *Electrochemical Cell Design*, pages 377–389. Plenum Press, 1984.

[37] Ralph E. White. On newman's numerical technique for solving boundary value problems. *Ind. Eng. Chem. Fundamentals*, 17(4):367–369, 1978.

[38] D. Fan and R. E. White. Modification of newman's band(j) subroutine to multi-region systems containing interior boundary conditions: Mband. *J. Electrochem. Soc.*, 138(6):1688–1691, June 1991.